

January 2013

Towards RANS Parameterization of Vertical Mixing by Langmuir Turbulence in Shallow Coastal Shelves

Nityanand Sinha

University of South Florida, nsinha@mail.usf.edu

Follow this and additional works at: <http://scholarcommons.usf.edu/etd>

 Part of the [Civil Engineering Commons](#), [Environmental Engineering Commons](#), and the [Ocean Engineering Commons](#)

Scholar Commons Citation

Sinha, Nityanand, "Towards RANS Parameterization of Vertical Mixing by Langmuir Turbulence in Shallow Coastal Shelves" (2013).
Graduate Theses and Dissertations.
<http://scholarcommons.usf.edu/etd/4945>

This Dissertation is brought to you for free and open access by the Graduate School at Scholar Commons. It has been accepted for inclusion in Graduate Theses and Dissertations by an authorized administrator of Scholar Commons. For more information, please contact scholarcommons@usf.edu.

Towards RANS Parameterization of Vertical Mixing by Langmuir Turbulence
in Shallow Coastal Shelves

by

Nityanand Sinha

A dissertation submitted in partial fulfillment
of the requirements for the degree of
Doctor of Philosophy
Department of Civil and Environmental Engineering
College of Engineering
University of South Florida

Major Professor: Andrés E. Tejada-Martínez, Ph.D.
Mark Ross, Ph.D.
Ping Wang, Ph.D.
Stanley Kranc, Ph.D.
Rasim Guldiken, Ph.D.

Date of Approval:
November 13, 2013

Keywords: Turbulent channel, KPP, Stokes drift velocity, Tidal channel, Numerical simulation

Copyright © 2013, Nityanand Sinha

Dedication

To my mother and father, whose positive, unflinching attitude towards life and whose belief on education have become my precious assets.

Acknowledgments

I wish to express my deepest gratitude to Dr. Andrés E. Tejada-Martínez, my major advisor, who provided me this wonderful opportunity to develop my capability to work independently and to challenge myself intellectually. His guidance, insight and encouragement were critical for the successful completion of this study. I would like to thank my committee members Rasim Guldiken, Ph.D., Mark Ross, Ph.D., Stanley Kranc, Ph.D., and Kathy Ping Wang, Ph.D. and my committee chairperson Boris Galperin, Ph.D. for their continual support and guidance throughout this dissertation.

I would also like to sincerely thank to Dr. Samir Kumar Das for his assistance and guidance in getting my graduate career started on the right foot.

I must thank all the members of the excellent Environmental Computational Fluid Dynamics group like, Roozbeh Golshan, Rachel Walker and Jie Zhang. I would like to give very special thank to Dr. Cigdem Akan for her friendship, guidance, help and teachings.

I would lastly and most importantly like to thank Rupa Nath for her endless support, encouragement, and patience throughout the last three years.

Table of Contents

List of Tables	iii
List of Figures	iv
List of Symbols	viii
Abstract	xii
1 Introduction	1
1.1 A Brief Introduction to Turbulence	1
1.1.1 The Physical Nature of Turbulence	1
1.1.2 Turbulent Boundary Layer	2
1.1.3 Basic Equation of Turbulent Flows	5
1.2 Numerical Approach to Turbulence Simulation	6
1.2.1 Direct Numerical Simulation	8
1.2.2 Large Eddy Simulation	8
1.2.3 Reynolds Averaged Navier-Stokes Simulation (RANSS)	11
1.3 Chapter Summary	15
2 Turbulence in the Upper Ocean	16
2.1 Context and Motivation	16
2.2 Langmuir Circulation	16
2.3 LES of Langmuir Turbulence	21
2.4 Objectives	22
2.5 Organization of the Dissertation	24
3 LES of Full-Depth Langmuir Circulation: Computational Methodology and Setup	26
3.1 Governing LES Equations	26
3.2 Spatially Filtered Navier-Stokes Equation (Craig-Leibovich Equation)	26
3.3 Flow Configuration	29
3.4 Turbulence Statistics	33
3.5 Chapter Summary	39
4 Surface Dynamics in LES of Langmuir Turbulence with Full-Depth LC	40
4.1 Introduction	40
4.2 Turbulence Structure	41
4.3 Disruption of the Near-Surface Log-Law	53
4.4 Budgets of Turbulent Kinetic Energy (TKE)	55
4.5 Budgets of TKE Components	58

4.6	Budgets of Reynolds Shear Stress	60
4.7	Summary and Conclusions	65
5	Bottom Boundary Layer Dynamics in LES of Langmuir Turbulence with Full-Depth LC	68
5.1	Introduction	68
5.2	Turbulence Structures	68
5.3	Mean Velocities	70
5.4	Budgets of Turbulent Kinetic Energy (TKE)	73
5.5	Budgets of TKE Components	75
5.6	Conclusion	78
6	A K-profile Parameterization of Langmuir Turbulence in Shallow Water	80
6.1	Introduction	80
6.2	Vertical Turbulent Mixing Models for the Coastal Ocean	81
6.3	K-Profile Parameterization	82
6.3.1	The Standard KPP Parameterization	82
6.4	A Modified KPP	85
6.4.1	Modification of KPP Based on Near-Surface Dynamics	86
6.4.2	Modification of KPP Model Accounting for Non-Local Transport	90
6.5	A Priori Evaluation of the Modified KPP Model	93
6.6	Bottom Boundary Condition	98
6.7	Conclusion	100
7	Influence of Strong Tidal Current on LC in Shallow Continental Shelf	102
7.1	Introduction	102
7.2	LES Equations and Flow Configuration	105
7.3	Results	108
7.4	Conclusion	114
8	Summary and Conclusions	116
	References	123
	Appendices	127
	Appendix A: Rights and Permissions	128
	A.1 Permission to Use Figure 1.2	128
	A.2 Permission to Use Figure 1.5	130
	A.3 Permission to Use Figure 7.1	131
	A.4 Permission to Use Figure 2.2 and 7.2	133

List of Tables

Table 3.1 Summary of wind and wave forcing parameters in simulations.	32
---	----

List of Figures

Figure 1.1 Two-dimensional image of a turbulent jet.	2
Figure 1.2 Schematic of boundary layer.	3
Figure 1.3 Subdivision of turbulent boundary layer.	4
Figure 1.4 Sketch of Kolmogorov energy spectrum for all turbulent flows.	7
Figure 1.5 Sketch of functions $f(x)$ and filtered function $f(x)$ with spatial filter of width Δ .	9
Figure 2.1 Sketch showing Langmuir cells (on left) and associated windrows (on right) along downwind direction.	18
Figure 2.2 Maps of the SeaWiFS particulate backscatter in the South Atlantic bight before (left) and during (right) a full-depth Langmuir cell event observed at the Navy R2 tower.	19
Figure 2.3 Ekman upwelling in the coastal ocean.	21
Figure 3.1 Computational domain and boundary conditions.	30
Figure 3.2 (a) Stokes drift velocity (b) Stokes drift velocity vertical shear.	32
Figure 4.1 Snapshots of instantaneous downwind velocity fluctuation on horizontal $x_1 - x_2$ planes at different depths in the upper half of the water column.	43
Figure 4.2 Snapshots of instantaneous downwind velocity fluctuation on the horizontal ($x_1 - x_2$) planes at different depths in the bottom half of the water column.	44
Figure 4.3 Instantaneous velocity fluctuations averaged over the downwind (x_1) direction in flow without LC (a)–(c) and in flow with LC with $La_t = 0.7$ and $\lambda = 6H$ (d)–(f).	46
Figure 4.4 Instantaneous velocity fluctuations averaged over the downwind (x_1) direction in flow with LC with $La_t = 1.0$ and $\lambda = 6H$ (a)–(c) and in flow with LC with $La_t = 0.7$ and $\lambda = 6H$ (d)–(f).	47

Figure 4.5 Instantaneous velocity fluctuations averaged over the downwind (x_1) direction in flow with LC with $La_t = 0.4$ and $\lambda = 6H$ (a)–(c) and in flow with LC with $La_t = 0.7$ and $\lambda = 6H$ (d)–(f).	48
Figure 4.6 Instantaneous velocity fluctuations averaged over the downwind (x_1) direction in flow with LC with $La_t = 0.7$ and $\lambda = 4H/3$ (a)–(c) and in flow with LC with $La_t = 0.7$ and $\lambda = 6H$ (d)–(f).	49
Figure 4.7 Normal components of the resolved Reynolds stress in flow without LC (a) and in flows with LC (b), (c).	50
Figure 4.8 (a) Root mean square (rms) of resolved vertical velocity and (b) contribution to resolved vertical velocity rms from full-depth LC.	50
Figure 4.9 Instantaneous snapshots of vertical velocity fluctuations at $x_1 = L_1/2$, where L_1 is the downwind length of the computational domain.	52
Figure 4.10 Mean downwind velocity (a) and mean downwind velocity deficit in the upper half of the water column (b) in flows with and without LC.	54
Figure 4.11 Budgets of TKE scaled by u_τ^2 in the surface log-layer.	57
Figure 4.12 Production to dissipation ratio in the surface log-layer.	58
Figure 4.13 Near-surface balance of TKE component budget terms (scaled by u_τ^2) in flows with and without LC.	59
Figure 4.14 Near-surface budget terms of $\langle \bar{u}'_1 \bar{u}'_3 \rangle$ (scaled by u_τ^2) in flows with and without LC.	60
Figure 4.15 (a) Production by mean velocity shear and (b) turbulent transport budget terms of $\langle \bar{u}'_1 \bar{u}'_3 \rangle$ (scaled by u_τ^2) in flows with and without LC.	61
Figure 4.16 (a) Mean velocity in upper half of water column and (b) Reynolds shear stress, $\langle \bar{u}'_1 \bar{u}'_3 \rangle$ in flows with and without LC.	62
Figure 4.17 A posteriori evaluation of the RANS eddy viscosity based on LES fields.	65
Figure 5.1 Instantaneous vertical velocity fluctuation (u'_3/u_τ) averaged over the downwind x_1 direction showing upwelling and downwelling limbs of Couette cells in (a) and LC in (b) (c).	69
Figure 5.2 Mean velocity profiles: panels (a) and (c) show the variation with λ at fixed La_t with $\lambda = 6H$, $La_t = 0.7$ the reference and panels (b) and (d) show the variation with La_t at fixed λ .	71
Figure 5.3 Mean velocity profiles within downwelling and upwelling limbs of Couette cells (a) and LC (b)–(d).	72

Figure 5.4 Near-bottom balance of TKE budget terms (scaled by u_τ^2) in flows with and flow without LC.	74
Figure 5.5 Ratio of production to dissipation of TKE.	75
Figure 5.6 Near-bottom balance of TKE component budget terms (scaled by u_τ^2) in flow with and without LC.	76
Figure 5.7 Near-bottom balance of Reynolds shear stress, $\langle \bar{u}'_1 \bar{u}'_3 \rangle$, budget terms (scaled by u_τ^2) in flows with and flow without LC.	77
Figure 6.1 Parameter γ in Eqn. (6-11) evaluated using LES fields within the surface log-layer.	88
Figure 6.2 Near-surface budget terms of $\langle \bar{u}'_1 \bar{u}'_3 \rangle$ (scaled by u_τ^2) in flows with and without LC.	89
Figure 6.3 Comparison between RANS and LES of flows with LC at $Re_\tau = 395$.	96
Figure 6.4 Momentum balance for modified nonlocal KPP in flows with LC at $Re_\tau = 395$.	97
Figure 6.5 Mean downwind velocity predicted in RANS with modified KPP and various different values of B coefficient in the log-law used for near-wall modeling.	100
Figure 7.1 Fields of fluctuating velocity components in downwind (u), crosswind (v) and vertical (w) directions and backscatter amplitude (A5) measured using an acoustic Doppler current profiler (Gargett and Wells 2007).	103
Figure 7.2 Fields of fluctuating velocity components in the downwind (u), crosswind (v) and vertical (w) directions and backscatter amplitude measured using an acoustic Doppler current profiler (Gargett and Savidge 2008).	104
Figure 7.3 Sketch of LES domain in simulations with oscillating crosswind body force.	106
Figure 7.4 Tidal phases represented via oscillating force f_2 in Eqn. 7.2 in LES of full-depth LC with crosswind tidal forcing.	107
Figure 7.5 Initial instantaneous velocity fluctuations averaged over the downwind (x_1) direction in flow with LC with $La_t = 0.7$ and $\lambda = 6H$.	108
Figure 7.6 Phase 1 instantaneous velocity fluctuations averaged over the downwind (x_1) direction in flow with LC with $La_t = 0.7$ and $\lambda = 6H$.	109
Figure 7.7 Phase 2 instantaneous velocity fluctuations averaged over the downwind (x_1) direction in flow with LC with $La_t = 0.7$ and $\lambda = 6H$.	110

Figure 7.8 Phase 3 instantaneous velocity fluctuations averaged over the downwind (x_1) direction in flow with LC with $La_t = 0.7$ and $\lambda = 6H$.	110
Figure 7.9 Phase 4 instantaneous velocity fluctuations averaged over the downwind (x_1) direction in flow with LC with $La_t = 0.7$ and $\lambda = 6H$.	111
Figure 7.10 Phase 5 instantaneous velocity fluctuations averaged over the downwind (x_1) direction in flow with LC with $La_t = 0.7$ and $\lambda = 6H$.	111
Figure 7.11 Root mean square (rms) of resolved velocity throughout the tidal cycle.	112
Figure 7.12 Mean downwind velocity near bottom and near surface throughout the tidal cycle.	113

List of Symbols

l	Mixing length
κ	Von Karman constant
ν	Kinematic viscosity
τ^ν	Molecular viscous stress
λ	Dominant wavelength of surface waves
La_t	Turbulent Langmuir number
Re	Reynolds number ($U_o D / \nu$)
D	Characteristic length scales
U_o	Characteristic velocity
L_{mix}	Mixing length
\bar{u}_i	i^{th} Component of the non-dimensional time-filtered velocity
x_i	i^{th} Component of position vector
U^+	Normalized mean streamwise velocity
y^+	Normalized wall normal distance
x_1	Downwind direction
x_2	Crosswind direction
x_3	Vertical direction
u_1	Velocity in the downwind direction
u_2	Velocity in the crosswind direction
u_3	Velocity in the vertical direction

$\bar{u}_{surface}$	Downwind velocity at surface
H	Total depth
p	Pressure
ρ_0	Constant density
t	Time
Re_t	Turbulent Reynolds number (UL/ν)
N	Number of grid points
Δ_f	Filter width
τ_{ij}	Reynolds stress tensor
G	Filter function
τ_{ij}^{SGS}	Sub-grid scale (SGS) stresses
\bar{P}	Resolved pressure
$\bar{\Pi}$	Space and time filtered modified pressure
ε_{ijk}	Totally antisymmetric third-rank tensor
ω_i	i^{th} Component of the non-dimensional time-filtered vorticity
U^S	Non-dimensional Stokes drift velocity
Re_t	Friction Reynolds number
S_{ij}	Mean strain rate tensor
P_{ij}	Mean shear production rate
Q_{ij}	Mean shear production rate
T_{ij}	Turbulent transport rate
T_{ij}^{sgs}	SGS transport rate
D_{ij}	Viscous diffusion rate
A_{ij}	Pressure transport rate

B_{ij}	Pressure-strain redistribution rate
ε_{ij}	Viscous dissipation rate
ε_{ij}^{sgs}	SGS dissipation rate
H	Channel half depth
$u_{\tau w}$	Friction velocity associated with wind stress
τ_w	Wind stress
τ_{ij}^{RNS}	RANS Reynolds stress tensor
ρ	Density
u_s	Surface Stokes drift velocity
ω	Dominant frequency
K	Dominant surface gravity wave wavenumber
a	Amplitude of surface gravity waves
P	Space-filtered pressure
ν_t	Eddy viscosity
Cs	Dimensionless Smagorinsky coefficient for momentum equation
S_{ij}	Filtered strain-rate tensor
x_3^+	Distance to the surface in plus units
Us	Stokes drift velocity
k	Turbulent kinetic energy
ε	Turbulent kinetic energy (TKE) dissipation rate
C_μ	κ - ε Model coefficient
h	Depth of the water column
ν_{hor}	Horizontal eddy viscosity
ν_{ver}	Vertical eddy viscosity

δ	Depth of the surface boundary layer
$w(\sigma)$	Velocity scale
$G(\sigma)$	Shape function
σ	Dimensionless vertical coordinate
ν'_t	Modified eddy viscosity
Γ	Counter-gradient flux
δ_{ij}	Kronecker's delta
Af_2	Oscillating body force

Abstract

Langmuir turbulence in the upper ocean is generated by the interaction between the wind-driven shear current and the Stokes drift velocity induced by surface gravity waves. In homogenous (neutrally stratified) shallow water, the largest scales of Langmuir turbulence are characterized by full-depth Langmuir circulation (LC). LC consists of parallel counter-rotating vortices aligned roughly in the direction of the wind. In shallow coastal shelves, LC has been observed engulfing the entire water column, interacting with the boundary layer and serving as an important mechanism for sediment re-suspension.

In this research, large-eddy simulations (LES) of Langmuir turbulence with full-depth LC in a wind-driven shear current have revealed deviations from classical log-layer dynamics in the surface and bottom of the water column. For example, mixing due to full-depth LC induces a large wake region eroding the classical bottom (bed) log-law velocity profile. Meanwhile, near the surface, Stokes drift shear serves to intensify small scale eddies leading to enhanced mixing and disruption of the surface velocity log-law.

The modified surface and bottom log-layer dynamics induced by Langmuir turbulence and full-depth LC have important implications on Reynolds-averaged Navier-Stokes simulations (RANSS) of the general coastal ocean circulation. Turbulence models in RANSS are typically calibrated under the assumption of log-layer dynamics, which could potentially be invalid during occurrence of Langmuir turbulence and associated full-depth LC. A K-Profile Parameterization (KPP) of the Reynolds shear stress in RANSS is introduced capturing the basic mechanisms by

which shallow water Langmuir turbulence and full-depth LC impact the mean flow. Single water column RANS simulations with the new parameterization are presented showing good agreement with LES.

1 Introduction

1.1 A Brief Introduction to Turbulence

Most fluid flows occurring in nature are turbulent flows. These flows occur over a wide spectrum extending from interstellar gas cloud motion to blood flow in our veins. Atmospheric flows and oceanic currents are further examples of turbulence in nature. Many if not most flows of applied science and engineering significance in the fields of geophysics, environmental sciences, and engineering can be characterized by turbulence. The Navier-Stokes equations (named after Claude-Louis Navier and George Gabriel Stokes) are universally believed to contain the physics of all flows including turbulent flows (within the continuum hypothesis). These equations describe the motion of fluids (liquid and gases) in space and time.

1.1.1 The Physical Nature of Turbulence

Even though many turbulent flows can be easily observed in day-to-day life, there is no precise and commonly accepted definition of turbulence, as it is considered highly complex and one of the least known physical processes. However, there do exist a number of generally accepted characteristics of turbulence:

- Turbulent flows are irregular.
- Turbulent flows are rotational and three-dimensional.
- Turbulent flows are both diffusive and dissipative

- Turbulent flows consist of a wide range of length and time scales.
- Turbulence is a characteristic of the flow and not of the fluid, and occurs at high Reynolds number.
- Turbulence is a continuum phenomenon.

Velocity fluctuations characteristic of turbulent flows are caused by irregular jostling between eddies consisting of packets of fluid elements (see Figure 1.1). The size of eddies is wide ranging being as large as the size of the flow domain to as small as on the order of millimeters.

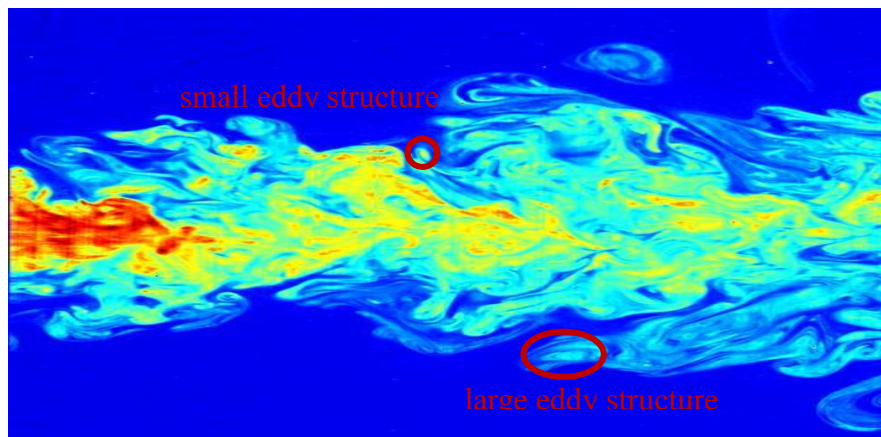


Figure 1.1 Two-dimensional image of a turbulent jet. [Jet by C. Fukushima and J. Westerweel, Technical University of Delft is licensed under CC BY 3.0. Accessed November 15, 2013]

1.1.2 Turbulent Boundary Layer

The concept of boundary layer was first introduced by Ludwig Prandtl in 1904. In this theory, when a viscous fluid flows over a stationary solid boundary, frictional forces slow down the motion of the fluid and the flow divides into two regions (Figure 1.2).

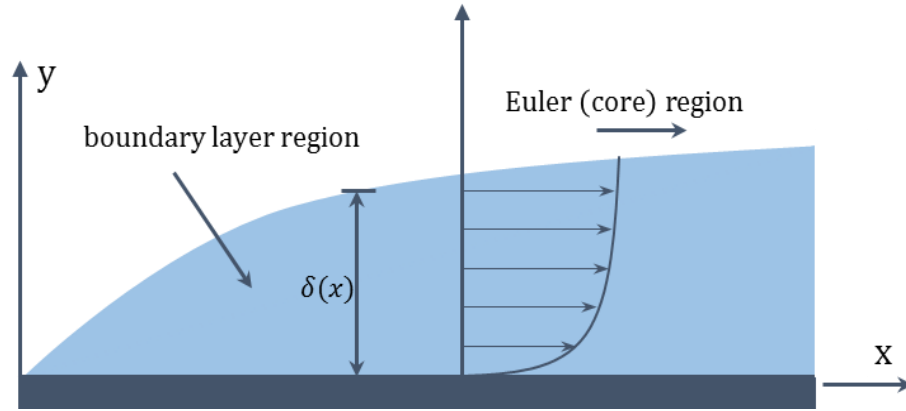


Figure 1.2 Schematic of boundary layer

- i) A thin layer adjoining the solid boundary where the viscous effects are dominant, known as a viscous boundary layer region.
- ii) The region beyond where the viscous effects are very small and flow behavior is similar to that of ideal fluid flow. This region is known as the Euler or core flow region.

A boundary layer may be laminar or turbulent. In laminar boundary layer, fluid flows in the form of laminates, i.e., layer sliding over adjacent layers. On the other hand, a turbulent boundary layer is characterized by eddy mixing across the layers. This mixing leads to exchange of momentum and energy across different regions of the boundary layer.

In a simplification of turbulent boundary layer theory, Prandtl postulated a mixing length model in which an eddy retains its identity for a certain distance ' l ' before colliding with other eddies, analogous to the concept of mean free path in thermodynamics. This mixing length ' l ' is further postulated to be proportional to the wall-normal distance between the eddy and the wall (boundary):

$$l = \kappa y \quad (1-1)$$

where κ is the empirical Von Karman's constant, ($\kappa = 0.41$) and y is wall-normal distance from the wall.

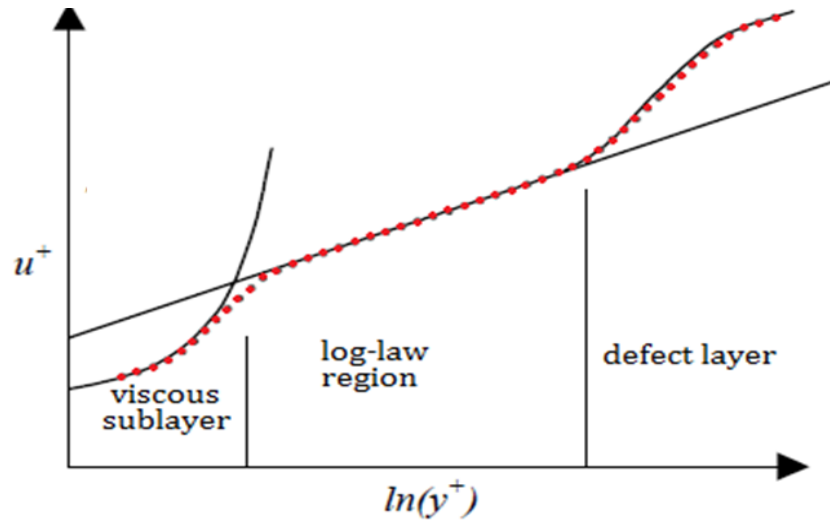


Figure 1.3 Subdivision of turbulent boundary layer

A turbulent boundary layer can be divided into three regions as depicted in Figure 1.3. In the inner layer, very close to the wall, Prandtl's mixing length theory does not hold. This region is referred to as the viscous sublayer or laminar sublayer. In this region, molecular viscosity plays a dominant role in momentum transport and velocity dependence can be approximated as $U^+ = y^+$ where $U^+ = U/u_\tau$ is normalized mean streamwise velocity (i.e. velocity in "plus units"), $y^+ = yu_\tau/\nu$ is the normalized distance (i.e. distance in "plus units") to the wall with $u_\tau = \sqrt{\tau_w/\rho}$ the friction velocity, ν the kinematic viscosity and τ_w the mean wall shear stress.

In the middle or log region, where turbulence plays the leading role in momentum transport, the mean streamwise velocity possess a logarithmic dependence and can be derived from Prandtl's mixing length model (Schlichting, 1960) as:

$$U^+ = \frac{1}{\kappa} \ln y^+ + B \quad \text{where } B \approx 5.5 \quad (1-2)$$

This equation is known as the log law and can be applied in the region of $30 < y^+ < 200$.

Note that except in cases of strong adverse pressure gradients (e.g. flow through a diffuser) or highly convective flows, the logarithmic velocity profile is a good approximation of velocity across the middle (shear dominated) layer.

Finally, in the outer layer, or so-called defect layer, mean velocity can be predicted by Coles' Law of the Wake [(Coles, 1956)]:

$$U^+ = \left(\frac{1}{\kappa} \ln y^+ + B \right) + \Pi(y^+) \quad (1-3)$$

where Π is an empirical wake function dependent on Reynolds number.

1.1.3 Basic Equation of Turbulent Flows

The fundamental equations that describe any Newtonian, incompressible fluid motion in a bounded domain Ω are the continuity equation in (1-4) and the momentum equation or Navier-Stokes equation in (1-5), both appearing in dimensionless form.

$$\frac{\partial u_i}{\partial x_i} = 0 \quad (1-4)$$

$$\frac{\partial u_i}{\partial t} + u_j \frac{\partial u_i}{\partial x_j} = - \frac{\partial P}{\partial x_i} + \frac{\partial \tau_{ij}^v}{\partial x_j} \quad (1-5)$$

In these equations u_i denotes the velocity field and P is the pressure field divided by constant density (ρ). The nonlinear term in the left hand side of equation (1.2) is referred to as the advective term. This term is the source of turbulence and when this term becomes significantly larger than the diffusive term ($\partial \tau_{ij}^v / \partial x_j$) in the right hand side, the flow becomes unstable and turbulent. Note that τ^v in the diffusive term is the molecular viscous stress, which is defined as

$$\tau^v = \frac{1}{Re} \left(\frac{\partial u_i}{\partial x_j} + \frac{\partial u_j}{\partial x_i} \right) \quad (1-6)$$

Here Re is Reynolds number ($Re = U_0 D/\nu$), representative of the importance of advection relative to diffusion. U_0 and D are characteristic velocity and length scales respectively used to non-dimensionalize the equations.

Even though the Navier-Stokes equations are well defined and derived from fundamental laws of physics, no general solution exists except for some simple flows. These equations are very sensitive to initial and boundary conditions. For laminar flows, it is possible to obtain analytical solution for these equations, but due to randomness in turbulent flows, finding an analytical solution of Navier-Stokes equations becomes next to impossible. However, turbulence is not completely random; presence of coherent motions in terms of spatial and temporal averages reflects some finite characteristics. A coherent motion (or eddy) can be defined as a *“three-dimensional region of the flow over which at least one fundamental flow variable (velocity component, density, temperature, etc.) exhibits significant correlation with itself or with another variable over a range of space and/or time that is significantly larger than the smallest local scales of the flow”* (Robinson, 1991).

1.2 Numerical Approach to Turbulence Simulation

As previously discussed, the difficulties and complexity with analytical and physical approaches are so enormous that the engineering and applied sciences communities have moved to the numerical approach for finding solutions to turbulent flows. Although numerical approaches have had significant success, there is no single approach that can tackle all flows (Davidson, 2004).

A turbulent flow is characterized by a wide range of scales (in both space and time), ranging from large scales at which energy typically is supplied to small scales at which energy is dissipated in the form of heat by viscosity. Interaction among various scales of eddies results in the transfer of energy from large eddies to smaller ones. This phenomenon is known as the energy cascade and, can be represented in terms of the Kolmogorov energy spectrum $E(k)$ where k is wave number (see Figure 1.4). Spatial scales (or eddies) are classified in three sub-ranges based on the energy spectrum. The range of energy containing large eddies is referred to as the integral scale. The mid-range of eddies is referred to as the inertial sub-range where the energy spectra is characterized by the well-known Kolmogorov's $-5/3$ law. The smallest eddies are within the energy dissipating range or the Kolmogorov scale. Note that the $k^{-5/3}$ shape of the energy spectrum within the inertial is universal (i.e. this shape of spectrum occurs in all turbulent flows).

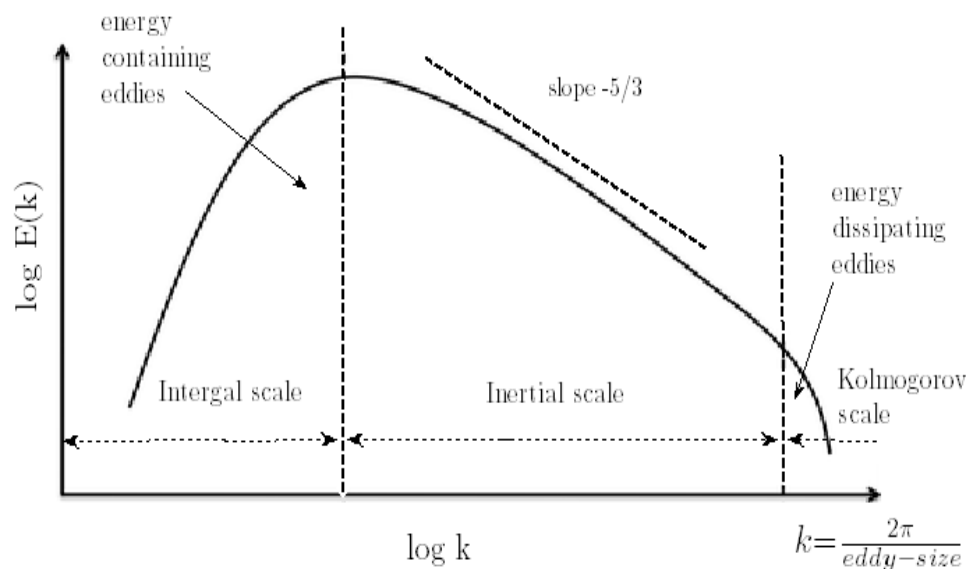


Figure 1.4 Sketch of Kolmogorov energy spectrum for all turbulent flows

1.2.1 Direct Numerical Simulation

A complete description of flow field variables (e.g. $u_i(x_i, t), P(x_i, t)$) can be obtained by numerically solving the continuity and Navier-Stokes equations. This most natural approach is termed direct numerical solution (DNS) as it resolves all scales of the turbulence. The range of scale in turbulent flows increases with Reynolds number. As per Kolmogorov theory, these smallest scales are of $O(Re^{-4/3})$. Thus in order to resolve all the scales, spatial separation of sampling points or grid points (Δx) should be $\Delta x \sim Re^{-4/3}$ and the total number of grid points required for a three dimensional computation should be $N \sim Re^{9/4}$.

Most of the flows in applied sciences and engineering applications have Reynolds number in range of $10^4 < Re < 10^8$. Therefore, the requirement of massive computational resources for DNS of turbulent flows limits its applicability to few existing applications and supercomputers. Thus, DNS cannot be considered as a brute force method for applied and industrial problems. Instead, it should be considered as a scientific tool that can be used similar to a physical laboratory experiment for development and validation.

1.2.2 Large Eddy Simulation

Large eddy simulation (LES) is an alternative technique to DNS based on scale separation between large energy containing eddies and small energy dissipating eddies of flow. The scale separation operator is defined as a low pass filter in wave number space. This corresponds to a spatial filter that decomposes the flow field variable in two components as

$$u = \bar{u} + u' \text{ and } P = \bar{P} + P' \quad (1-7)$$

where \bar{u} and \bar{P} are the filtered components and u' and P' are unresolved (residual or subgrid) components. The effect of filtering can be seen in Figure 1.5 where the filter damps scales smaller or of the size of the filter width Δ (Tejada-Martínez, 2002).

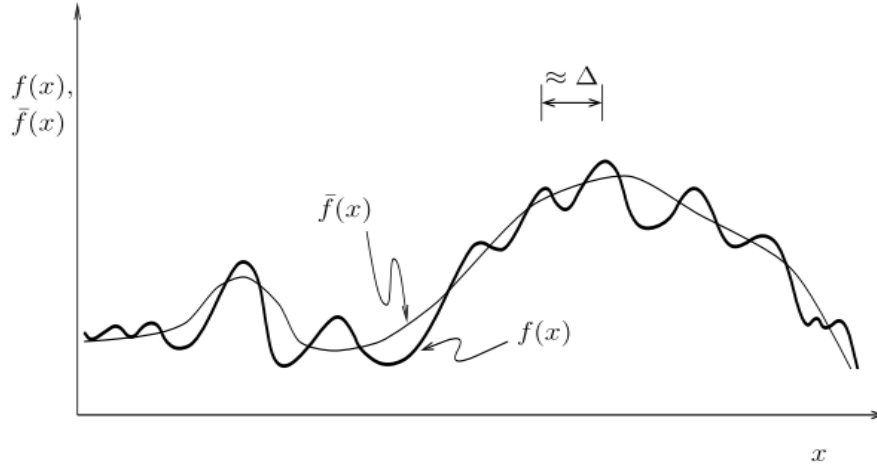


Figure 1.5 Sketch of functions $f(x)$ and filtered function $\bar{f}(x)$ with spatial filter of width Δ . [Reprinted with permission from A. Tejada-Martínez, Dynamic Subgrid-scale Modeling for Large Eddy Simulation of Turbulent Flows with a Stabilized Finite Element Method, PhD thesis, Rensselaer Polytechnic Institute, November 2002. Copyright 2002, A. Tejada-Martínez.]

Applying the spatial filtering operation to the incompressible continuity and Navier-Stokes equations, the LES equations can be obtained:

$$\frac{\partial \bar{u}_i}{\partial x_i} = 0 \quad (1-8)$$

$$\frac{\partial \bar{u}_i}{\partial t} + \frac{\partial \bar{u}_i \bar{u}_j}{\partial x_j} = -\frac{\partial \bar{P}}{\partial x_i} + \frac{1}{Re} \frac{\partial^2 \bar{u}_i}{\partial x_j^2} - \frac{\partial \tau_{ij}^{LES}}{\partial x_j} \quad (1-9)$$

Solution of these equations gives the filtered or resolved velocity and pressure components corresponding to the larger (more energetic) scales of the flow. Filtering the Navier-Stokes equation introduces a stress apart from the molecular viscous stress usually referred as the

residual stress, τ_{ij}^{LES} . This stress represents the influence of the smaller (less energetic) residual (or filtered-out) components on the resolved components, and is defined as

$$\tau_{ij}^{LES} = \overline{u_i u_j} - \overline{u_i} \overline{u_j} \quad (1-10)$$

The residual stress is often referred to as the subgrid-scale (SGS) stress because typically, in what is often referred to as implicit LES, the numerical discretization (including the grid) implicitly act as the LES filter, filtering out the small scales that are unresolvable (unsupported) by the grid. Thus, the local filter width is roughly equal to the local grid cell size.

The SGS stress presents a closure problem because it requires knowledge of unfiltered velocity u_i , which is not accessible (i.e. unknown) in LES. The SGS stress is typically decomposed into deviatoric (trace-free) and isotropic components respectively:

$$\tau_{ij}^{LES} = \tau_{ij}^{LES(d)} + \frac{1}{3} \delta_{ij} \tau_{kk}^R \quad (1-11)$$

where the deviatoric component is defined as

$$\tau_{ij}^{LES(d)} = (\overline{u_i u_j} - \overline{u_i} \overline{u_j}) - \frac{1}{3} \delta_{ij} (\overline{u_k u_k} - \overline{u_k} \overline{u_k}) \quad (1-12)$$

Typically the isotropic component (i.e. the second term in the RHS of (1.8)) is lumped with the pressure in the momentum equation giving rise to a modified pressure and the deviatoric component is modeled in terms of resolved quantities. The deviatoric SGS stress (or simply the SGS stress) can be modeled by making use of an eddy viscosity model:

$$\tau_{ij}^{LES(d)} = -2\nu_t^{LES} \bar{S}_{ij} \quad (1-13)$$

where ν_t^{LES} is the LES eddy viscosity and the filtered strain rate is defined as $\bar{S}_{ij} = (\bar{u}_{i,j} + \bar{u}_{j,i})/2$. Physical arguments suggests that ν_t^{LES} should be defined as a product of characteristic length scale (typical filter width) and a characteristic velocity scale (Davidson, 2004). In theory, the LES filter or grid filter should fall within the inertial subrange of the energy spectrum (Figure 1.4) thereby guaranteeing the resolution of eddies within the inertial subrange. This also facilitates the derivation of a model for the eddy viscosity ν_t^{LES} that is valid for all turbulent flows (Smagorinsky, 1963) given the universality of the inertial subrange as mentioned earlier.

Even though LES is substantially less demanding than DNS in terms of computational resources, in theory LES still requires that resolved scales be within the inertial sub-range. In near-wall regions, the length scales corresponding to the inertial subrange become smaller as the approximate size of energy containing eddies is of the order of their distance from the wall. Thus, in order to resolve the inertial subrange and associated dynamically important eddies a high resolution mesh is required in near-wall regions. LES is sometimes performed in conjunction with a near-wall model in order to avoid high resolution of the near-wall region (Pope, 2000).

1.2.3 Reynolds Averaged Navier-Stokes Simulation (RANSS)

A less expensive approach for numerical solution of the Navier-Stokes equation is RANSS. The notion behind RANSS is similar to LES, but rather than employing a spatial filter as is done in LES, an ensemble average is employed in RANSS. However, RANSS does not attempt to resolve any of the turbulent scales, but rather the mean component of the flow only. In contrast, LES aims to capture the mean component plus all turbulent scales down to the inertial subrange.

In RANSS, a flow field variable can be represented in terms of a mean (large scale) and a fluctuating component in what is often referred to as the Reynolds decomposition:

$$u = \langle u \rangle + u' \text{ and } P = \langle P \rangle + P' \quad (1-14)$$

where fluctuations u' and P' are measures of the turbulent intensity of flow field variables and in statistical equilibrium flows (i.e. in statistically steady flows) have zero mean ($\langle u' \rangle = 0$ and $\langle P' \rangle = 0$). Mean quantities $\langle u \rangle$ and $\langle P \rangle$ can be defined by ensemble or long-term time averaging.

- i. Ensemble Averaging: This can be represented by repeating a flow experiment N times with identical initial and boundary conditions. Ensemble averaging consists of taking the arithmetic mean of variables of the N experiments and can be represented as

$$\langle u \rangle = \lim_{N \rightarrow \infty} \frac{1}{N} \sum_{i=1}^N u_i \quad (1-15)$$

- ii. Time Averaging: This was Reynolds' original approach and alternatively referred to as Reynolds averaging, which describes a mean flow field variable as

$$\langle u \rangle(t) = \frac{1}{T} \int_{t-T}^t u(s) ds \quad (1-16)$$

where averaging time scale T must be greater than the characteristic time scale of the turbulence (τ). In case of statistically equilibrium turbulence, mean flow field variables become time independent, thus can be defined as

$$\langle u \rangle_T = \frac{1}{T} \int_{t-T}^t u(t) dt \quad (1-17)$$

Reynolds averaging the continuity and momentum equations and making use of the decomposition in (1-11) leads to the following Reynolds-averaged equations:

$$\frac{\partial \langle u_i \rangle}{\partial x_i} = 0 \quad (1-18)$$

$$\frac{\partial \langle u_i \rangle}{\partial t} + \langle u_j \rangle \frac{\partial \langle u_i \rangle}{\partial x_j} = -\frac{\partial \langle P \rangle}{\partial x_i} + \frac{1}{Re} \frac{\partial^2 \langle u_i \rangle}{\partial x_j^2} - \frac{\partial \tau_{ij}^{RNS}}{\partial x_j} \quad (1-19)$$

Reynolds averaging generates a stress (a one-point velocity second-order correlation tensor) universally known as the Reynolds stress as a by-product of the advective non-linearity. This Reynolds stress represents the effect of the unresolved turbulence on the resolved mean flow and is defined as

$$\tau_{ij}^{RNS} = -\langle u'_i u'_j \rangle \quad (1-20)$$

The Reynolds stress $\langle u'_i u'_j \rangle$ is in terms of unknown velocity fluctuations (not computed in RANSS), thus a mathematical/physical model is needed to provide closure for this stress.

RANS turbulence models can be divided into two categories, eddy viscosity-based models and non-linear eddy viscosity (second moment closure) models. Eddy viscosity models are based on the Boussinesq assumption that approximates the Reynolds stress tensor as a function of the mean-strain rate tensor and eddy viscosity:

$$\tau_{ij}^{RNS} = 2\nu_t^{RNS} \langle S_{ij} \rangle + \frac{2}{3} k \delta_{ij} \quad (1-21)$$

where k is turbulent kinetic energy (TKE) defined as $k = \langle u'_i u'_i \rangle / 2$ and the mean-strain rate tensor is $\langle S_{ij} \rangle = (\partial \langle u_i \rangle / \partial x_j + \partial \langle u_j \rangle / \partial x_i) / 2$.

Most popular eddy viscosity-based models in engineering applications are the k - ε and k - ω models (Umlauf et al., 2003). In the k - ε model, the eddy viscosity is taken as $\nu_t^{RNS} = C_\mu k^2 / \varepsilon$, where k is TKE, ε is TKE dissipation rate and C_μ is a coefficient calibrated as 0.09 based on classical log-layer dynamics. In the k - ε model, transport equations are solved in order to predict k and ε . In contrast, a non-linear eddy viscosity model solves modeled differential equations for the Reynolds stress components in (1-20) instead of expressing the stress components via (1-21). In geophysical applications, the widely used Mellor-Yamada models (Mellor and Yamada, 1982) make use of similar eddy viscosity expressions as the one shown above in terms of k , requiring solution of a transport equation for k .

In simulation of large domains ($\sim 10^5 m$) involving, for example, the general circulation of the ocean or the atmospheric boundary layer, transport equations based on eddy viscosity models are accurate but computationally expensive. A zero (algebraic) equation model (i.e. without any PDE to describe transport of turbulent stress and fluxes) is less expensive. In these models, a simple algebraic relation, for example, based on Prandtl's mixing length theory is used to predict eddy viscosity:

$$\nu_t^{RNS} = L_{mix}^2 \sqrt{2 \langle S_{ij} \rangle \langle S_{ij} \rangle} \quad (1-22)$$

Here L_{mix} is the mixing length, which is proportional to the standard deviation of vertical displacement of fluid parcels. Thus, the definition of L_{mix} is different from problem to problem.

For example, in a fully developed turbulent region of equilibrium boundary layers, L_{mix} can be

approximated using a simple linear relationship, $L_{mix} = \kappa y$, where κ is the von Karman constant, $\kappa = 0.41$, and y is wall normal distance to the wall. Note that Prandtl's mixing length $L_{mix} = \kappa y$, may be used to derive the log law (as was mentioned earlier) in what is often referred to as similarity theory.

In oceanic applications, Prandtl's mixing theory has been extended to the ocean surface boundary layer; in these cases y is the normal distance to the surface. Furthermore, algebraic models such as the K-profile parameterization (KPP) (Large et al. 1994) have been designed to calculate eddy viscosity based on Prandtl's mixing length theory within the surface log-layer while blending with an eddy viscosity based on local water column stability (stratification) in the interior of the water column. The KPP will be studied in detail in Chapter 6.

1.3 Chapter Summary

In this chapter, summaries of turbulence and boundary layer theory were provided. Furthermore, numerical methodologies for tackling turbulence such as DNS, LES and RANSS were described. In the case of LES and RANSS, it was observed that the presence of unresolved motions requires stress closure models in terms of resolved quantities. In RANSS the closure model plays an important role in the accuracy of the predicted mean flow component given that this model accounts for the effect of the entire range of turbulent scales. In LES, the SGS (or subgrid-scale) closure plays a less important role given that it only needs to account for the effect of less energetic scales of size smaller than roughly the grid size.

2 Turbulence in the Upper Ocean

2.1 Context and Motivation

The coastal ocean and shallow sea regions are among the most challenging marine environments to model or simulate computationally. These regions are associated with several geometric constraints and varying bathymetry, and subjected to complex array of lateral, internal and surface forces. These forces include Coriolis, tidal, wind, wave and buoyancy forces, and contain a broad range of spatial and temporal scales. Thus, the resulting circulation patterns contain both steady and time varying features. These circulation patterns can be characterized by vertical stratification, trapped internal waves, intense internal currents, coastal upwelling and downwelling and intense turbulent mixing at both surface and bottom boundary layers with the mixing engulfing the entire water column in some cases. The latter condition is of interest here.

2.2 Langmuir Circulation

In wind driven shear flows, exchange of momentum, energy and species from wind to the ocean interior is primarily through wind-current interaction (Donelan, 1998). This wind-current interaction has major influence on turbulent mixing in the upper ocean boundary layer, which consequently affects surface boundary fluxes of scalars. One of the usually associated phenomena with this interaction is Langmuir circulation (LC) which consists of parallel counter rotating vortices oriented roughly in the downwind direction (see sketch in Figure 2.1) as

originally observed by (Langmuir, 1938). It is well known that interaction between the Stokes drift velocity induced by the surface gravity waves with the wind-driven current gives rise to Langmuir turbulence, characterized by LC. More specifically, LC corresponds to coherent scales in the Langmuir turbulence. Wind speeds greater than 3 m s^{-1} present ideal conditions for the generation of LC. Floating particles and foam tend to accumulate at the surface convergence of these cells lining up in what is often referred to as windrows. Typical length scales of these windrows (or LC) vary across a wide range. For example, the distance between the windrows has been observed to be between 2 and 300 meters. The length of the windrows in the direction of the wind has been observed to be between 200 and 3000 meters.

In the upper ocean, turbulence is generated via a number of mechanisms such as surface-wave breaking, wave-current interaction (giving rise to Langmuir-dominated turbulence), wind shear (giving rise to shear-dominated turbulence) and destabilizing surface heat fluxes (giving rise to convective turbulence). A recent study by Belcher et al. (2012) found that wind and wave forcing conditions in the Southern Ocean are favorable to Langmuir-dominated turbulence over 80% of the time throughout the year. Meanwhile in the North Atlantic, during winter, conditions are favorable to Langmuir-dominated turbulence for about 70% of the time. Overall their conclusion was that Langmuir turbulence is important everywhere in the world's ocean and thus must be parameterized in climate models.

Given its frequent occurrence, Langmuir turbulence has major impact on surface boundary layer turbulence and it significantly enhances the vertical mixing in the upper ocean mixed layer (UOML) that helps to sustain nearly uniform salinity, temperature and overall density in this layer. The UOML refers to the uppermost 30 to 70 meters of the ocean strongly influenced by

vertical turbulent mixing generated by the mechanisms mentioned earlier (i.e. surface breaking waves, destabilizing surface heat fluxes wind shear and wave-current interaction).

Langmuir turbulence also plays a dominant role in passive scalar transport of dissolved gases. Transfer of gases (such as CO₂) from the air side to the water side across the air-water interface as well as the vertical fluxes of these dissolved gases throughout the water column are governed by the dynamics of turbulent vertical mixing in the oceanic surface boundary layer. Recent LES in (Akan et al., 2013) has shown that Langmuir turbulence in a fully mixed water column with full-depth LC serves to increase the scalar transfer rate across the air-water interface by up to 60%, consistent with the laboratory experiments of (Veron and Melville, 2001).

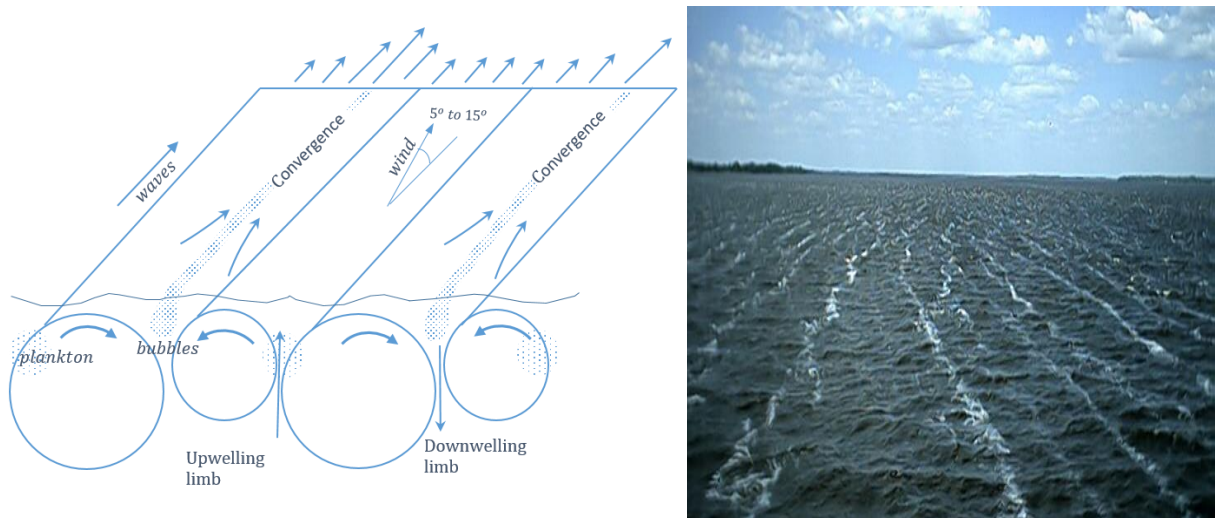


Figure 2.1 Sketch showing Langmuir cells (on left) and associated windrows (on right) along downwind direction. Windrows consist of lines of foam accumulated along the surface convergence zones of the Langmuir cells. Note the downwelling and upwelling limbs of the cells serving to enhance vertical mixing beneath the surface.[windrows (right) :Reprinted with permission from Andreas M. Thurnherr, Columbia University, Source: <http://www.ldeo.columbia.edu/~ant/Langmuir> .Accessed November 15, 2013]

Typically, Langmuir circulation has been observed in the UOML over deep water. However, recent measurements reported in (Gargett et al., 2004) and (Gargett and Wells, 2007) confirmed the presence of LC in shallow continental shelves in fully mixed water columns ranging from 15

meters deep to 30 meters deep. These Langmuir cells were observed engulfing the whole depth of the water column and interacting with the bottom boundary layer. These full-depth cells have been termed Langmuir supercells as they profoundly affect turbulent kinetic energy and Reynolds stresses throughout the entire water column including the bottom boundary layer, consequently affecting transport of sediments and benthic (bottom-dwelling) micro-organisms across shallow shelf regions. This can be seen through satellite maps (Figure 2.2) of in-water particles provided by Gargett and Savidge (2008).

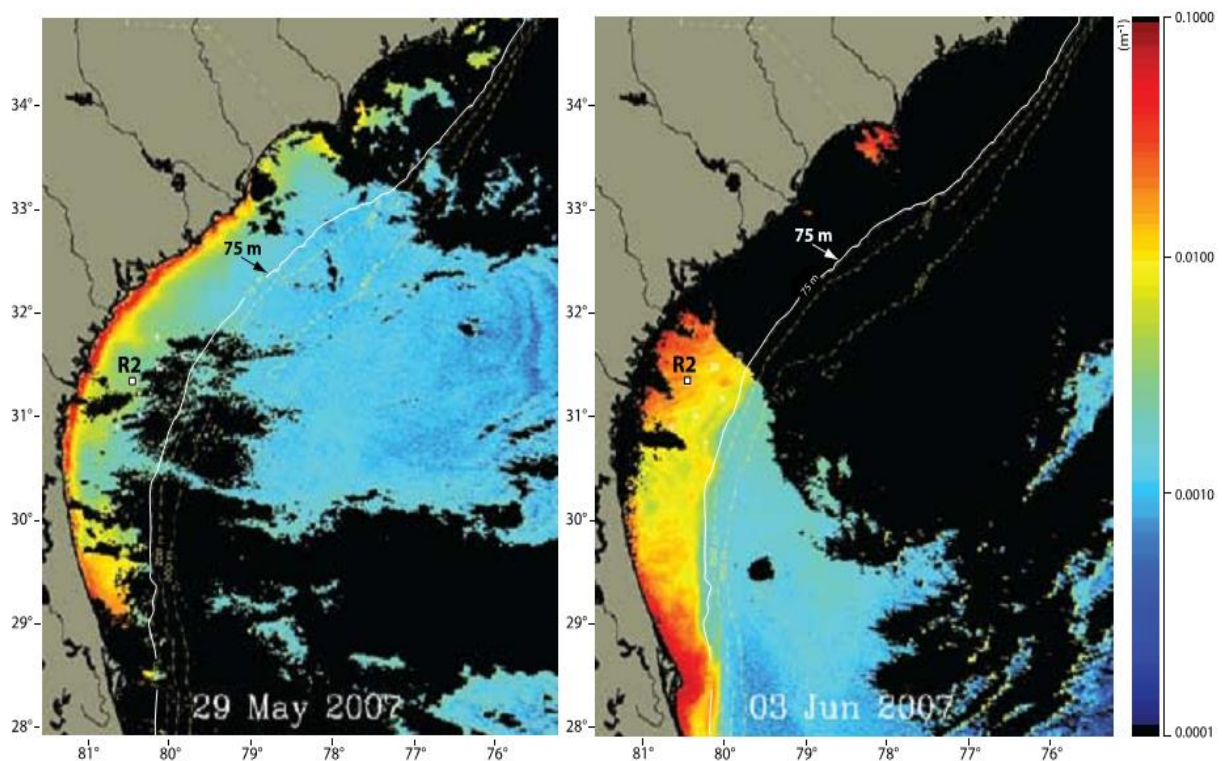


Figure 2.2 Maps of the SeaWiFS particulate backscatter in the South Atlantic bight before (left) and during (right) a full-depth Langmuir cell event observed at the Navy R2 tower (denoted with an open circle). The simultaneous occurrence of high particulate backscatter and full-depth Langmuir cells suggest that the latter could be a major contributor to sediment re-suspension and cross-shelf particle transport. Note that black areas offshore are cloud covered. [Savidge, W.B., A. Gargett, R.A. Jahnke, J.R. Nelson, D.K. Savidge, R.T. Short, and G. Voulgaris. 2008. Forcing and dynamics of seafloor-water column exchange on a broad continental shelf. *Oceanography* 21(4):179–184]

These maps show backscatter of water column particles in the South Atlantic Bight before and during a full-depth LC event observed at the R2 Navy tower. These maps provide evidence that the full-depth LC event measured at the R2 tower during the passage of a storm was likely a shelf-wide event, playing a key role in the re-suspension and cross-shelf transport of sediments.

Langmuir turbulence with full-depth Langmuir cells may also potentially play an important role in coastal upwelling dynamics in addition to the traditional processes involving stratification, bottom topography and Coriolis forcing effects. The Coriolis effect gives rise to Ekman transport consisting of surface currents directed at right angles to the direction of the winds. More specifically, Ekman transport is directed to the right (left) of the wind direction in the Northern Hemisphere (Southern Hemisphere). In the coastal shelf, along-shore winds can cause Ekman transport away from the shore, as warm surface waters flowing away from the coast are replaced by colder nutrient-rich waters (important for fisheries) brought by upwelling cross-shore currents (see Figure 2.3). As shown by the two-dimensional simulations of (Durski, 2004) strong mixing of the water column in regions closest to the coast may limit the cross-shore extent of upwelling currents, forcing these currents to terminate off-shore (i.e. at distances farther away from the coast). This results in a shut-down of near-coast, cross-shelf transport of nutrients, as well-mixed water becomes trapped at the coast. It is hypothesized that the shut-down mechanism may be enhanced by the intense vertical mixing caused by the action of full-depth Langmuir cells. Improved understanding and thus representation of water column dynamics during occurrences of full-depth LC (which is the overarching goal of the present research) should lead to future studies of the previously described hypothesis.

The previous examples are among many examples of how Langmuir turbulence can impact physical, biological and chemical processes in the upper ocean mixed layer and throughout the

full-depth of the water column in shallow coastal shelf regions. Reviews containing a large number of examples is given by (Thorpe, 2004) and (Barstow, 1983).

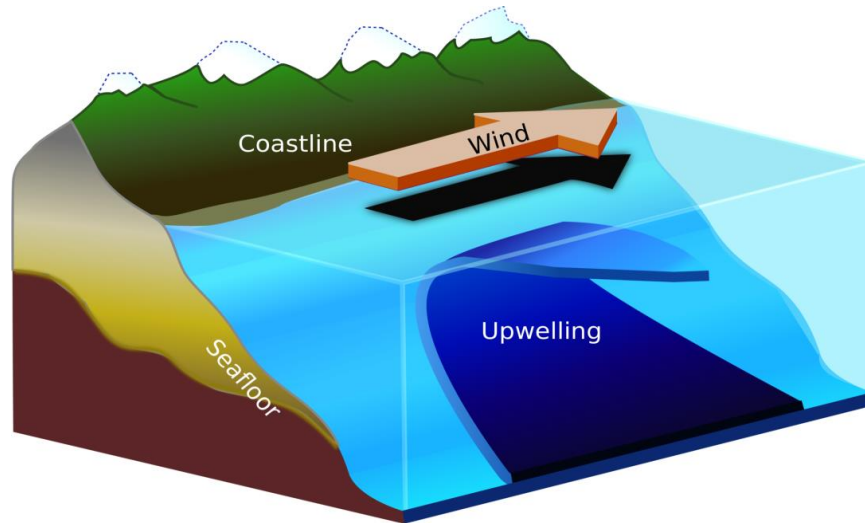


Figure 2.3 Ekman upwelling in the coastal ocean.[by Lichtspiel, Released in public domain. Retrieved from <http://en.wikipedia.org/wiki/Upwelling>, Accessed on November 15, 2013]

2.3 LES of Langmuir Turbulence

Conventionally, mean velocity depth-profiles within the bottom boundary layer (BBL) and surface boundary layer (SBL) in the ocean are represented by the universal law of wall (Pope, 2000) described earlier. As presence of Langmuir turbulence with full-depth LC significantly enhances the vertical mixing throughout the entire water column in shallow coastal regions, it may also affect both the BBL and SSL dynamics in shallow coastal shelves. In this work, we extend the LES of Tejada-Martinez and Grosch (2007) in order to investigate the effect of shallow water Langmuir turbulence characterized by full-depth LC on BBL and SBL dynamics, specifically on log-layer dynamics.

In the LES, the governing equations are based on the theory of Craik and Leibovich (1976). A theory for the generating mechanism behind Langmuir turbulence and associated LC was developed by (Craik and Leibovich, 1976). In Craik-Leibovich theory (CL theory), the interaction between the wind-driven shear current and Stokes drift velocity induced by surface gravity waves generating Langmuir turbulence is parameterized via the Craik-Leibovich vortex force appearing in the momentum equation (Navier-Stokes equation). This force consists of the cross product between the depth-dependent Stokes drift velocity and the resolved vorticity. Inclusion of the Craik-Leibovich vortex force in the governing equations allows for simulations without having to resolve the surface gravity waves. Thus, the surface can be taken as non-deforming or flat, resulting in more economical computations. The Craik-Leibovich theory has enabled a large number of numerical investigations of Langmuir turbulence in the oceanic surface mixed layer over deep water [(Skillingstad and Denbo, 1994), (McWilliams et al. 1997), (Kawamura, 2000), (Harcourt and D'Asaro, 2008) and (Grant and Belcher, 2009) and many others]. For shallow water, (Tejada-Martínez and Grosch, 2007) conducted numerical investigation using LES following the field measurement of full-depth Langmuir cells reported by (Gargett et al., 2004) and (Gargett and Wells, 2007) and found good agreement between the field measurements and computations in terms of the velocity fluctuation magnitude and structure characterizing the full-depth LC.

2.4 Objectives

Although LES has proven its capability in resolving turbulent quantities and the physics of flow consisting of LC in both shallow and deep oceans, its applicability is limited by the number of degrees of freedom since a high resolution mesh is required to resolve dynamically important

eddies in near-wall and near-surface regions at high Reynolds numbers. Thus LES simulations of Langmuir turbulence such as those of Tejada-Martinez and Grosch (2007) have been performed at much lower Reynolds numbers than those measured in the field.

A less computationally expensive approach alternative to LES is that of RANSS, as described in the introductory chapter. In RANSS only the mean component of the flow is resolved and the effect of the turbulent scales on the mean component is parameterized via a turbulence model. For example, RANSS is typically used for simulation of the coastal ocean circulation where large scale components such as upwelling and downwelling currents are resolved and turbulence effects on these large scale components are often accounted for (or parameterized) via eddy viscosity-based models such as the $k-\varepsilon$ model or Mellor-Yamada models mentioned earlier. These models have been derived under the assumption of classical boundary layer dynamics while excluding the possibility for the presence of Langmuir turbulence and associated full-depth Langmuir cells. *In light of this, the main objective of this dissertation is to use LES to understand how Langmuir turbulence with full-depth LC affects near-surface and near-bottom boundary layers in order to propose and test a new RANSS turbulence parameterization that accounts for this turbulence regime.*

A secondary objective of this work is to use LES to begin understanding the impact of tidal forcing on shallow water Langmuir turbulence and its interaction with bottom and surface boundary layers. It is well-known, that in shallow shelves, tidal currents generate significant bottom boundary layer turbulence, and the potential interaction between this turbulence and the surface-generated Langmuir turbulence is not well-understood. Previous LES studies of Langmuir turbulence with full-depth LC have only simulated bottom and surface boundary layer turbulence generated by the wind-driven shear current without the action of tides.

2.5 Organization of the Dissertation

The rest of this dissertation is organized as follows.

Chapter 3 presents the LES equations consisting of the filtered Craik-Leibovich equations. These equations are essentially the Navier-Stokes equations augmented with the Craik-Leibovich vortex force representing the generating mechanism for Langmuir turbulence. Chapter 3 also presents transport equations for turbulent kinetic energy (TKE), TKE components, and Reynolds shear stress. Analysis of the terms in these equation using computed LES velocity and pressure fields will provide insight on the impact of Langmuir turbulence on bottom and surface boundary layers.

Chapter 4 presents LES simulations of shallow water Langmuir turbulence in a wind-driven shear current under various wind and wave forcing conditions. Focus is placed on the influence of the Langmuir turbulence on the surface boundary layer.

Chapter 5 presents further analysis of the LES simulations focusing on bottom boundary layer dynamics. The impact of the full-depth LC (characterizing the Langmuir turbulence) on bottom log-layer dynamics is revealed.

Based on the understanding gained in Chapters 4 and 5 on how the Langmuir turbulence influences the surface and bottom boundary layers, Chapter 6 presents a novel turbulence parameterization accounting for the impact of Langmuir turbulence and full-depth LC throughout the entire water column. The new turbulence parameterization is tested in single water column RANS simulations of wind-driven shear flow characterized by Langmuir turbulence with full-depth LC and results show improved agreement with LES results over

traditional turbulence parameterizations that do not take into account the effect of Langmuir turbulence.

Chapter 7 returns to LES of shallow water Langmuir turbulence in order to understand the impact of a crosswind oscillating tidal current on the turbulence structure. These simulations have been motivated by field measurements of full-depth LC under weak and strong tidal currents by Gargett and Wells (2007) and Gargett and Savidge (2008). Furthermore, these simulations open the door for future research further exploring the turbulence structure under the combined influence of a wind stress and tidal forcing with and without Langmuir forcing.

Finally, Chapter 7 presents a summary of the key conclusions obtained in this research and provides suggestions for future research.

3 LES of Full-Depth Langmuir Circulation: Computational

Methodology and Setup

3.1 Governing LES Equations

In order to understand near-bottom and near-surface boundary layer dynamics in the presence of Langmuir turbulence with full-depth LC, LES of wind-driven shallow water flow with and without tidal forcing has been performed. The formulation described in this chapter is for the case without tidal forcing; the case with tidal forcing will be addressed in Chapter 7.

The continuity and Navier-Stokes (N-S) equations are the basic governing equations for turbulent flows. Interaction between Stokes drift velocity induced by surface gravity waves and the wind-driven shear current leads to the generation of Langmuir turbulence characterized by LC. The governing equations for LES of Langmuir turbulence are the filtered continuity and Navier-Stokes equations augmented with the Craik-Leibovich (C-L) vortex force [(Craik and Leibovich, 1976)], the latter force serving to parameterize the generating mechanism for Langmuir turbulence without having to directly resolve the surface gravity waves.

3.2 Spatially Filtered Navier-Stokes Equation (Craik-Leibovich Equation)

The non-dimensional, low-pass spatially and time filtered continuity and Navier-Stokes equation augmented with the Craik-Leibovich vortex force can be written as

$$\frac{\partial \bar{u}_i}{\partial x_i} = 0 \quad (3-1)$$

$$\frac{\partial \bar{u}_i}{\partial t} + \bar{u}_j \frac{\partial \bar{u}_i}{\partial x_j} = -\frac{\partial \bar{\Pi}}{\partial x_i} + \frac{1}{Re_\tau} \frac{\partial^2 \bar{u}_i}{\partial x_j^2} - \frac{\partial \tau_{ij}^{LES(d)}}{\partial x_j} + \frac{1}{La_t^2} \epsilon_{ijk} U_j^S \bar{\omega}_k \quad (3-2)$$

where ϵ_{ijk} is the totally antisymmetric third-rank tensor and over bar denotes the application of low pass space and time filters. The filter consists of the spatial filter in traditional LES (described earlier) compounded with a time filter for the purpose of filtering out the surface gravity waves, as per the Craik-Leibovich (1976) formulation. Variables \bar{u}_i and $\bar{\omega}_i$ are the filtered i^{th} component of velocity and vorticity in a Cartesian co-ordinate system (x_1, x_2, x_3) . The space and time filtered modified pressure is denoted as $\bar{\Pi}$. The exact expression for $\bar{\Pi}$ in terms of the original pressure and the Stokes drift velocity is defined by (McWilliams et al., 1997):

$$\bar{\Pi} = \bar{P} + \frac{1}{2} \Gamma \quad (3-3)$$

where \bar{P} is the non-dimensional, space- and time-filtered pressure divided by density and

$$\Gamma = \frac{1}{La_t^4} U_i^S U_i^S + \frac{1}{La_t^2} \bar{u}_i U_i^S$$

with U_i^S denoting the pre-determined Stokes drift velocity induced by surface waves.

The C-L vortex force is the last term in equation (3-2) consisting of the Stokes drift velocity crossed with the flow vorticity.

These equations have been made dimensionless with water column half depth δ and friction velocity u_τ . Friction velocity u_τ is associated with wind stress τ_w and can be expressed as $u_\tau = \sqrt{\tau_w/\rho}$, where ρ is the density of the water. Friction Reynolds number ($Re_\tau = u_\tau \delta/\nu$) is the measure of the strength of advection relative to diffusion.

The turbulent Langmuir number La_t appearing in the dimensionless Craik-Leibovich equation consists of the ratio of friction velocity u_τ to characteristic Stokes drift velocity U_0 and is expressed as $La_t = \sqrt{u_\tau/U_0}$, where $U_0 = \omega k a^2$, with ω the dominant frequency, k the dominant wave number (inversely proportional to the dominant wavelength, λ) and a the dominant amplitude of the surface gravity waves generating Langmuir turbulence. Note that, the dominant wave number of surface gravity waves is $k = 2\pi/\lambda$. The turbulent Langmuir number La_t is inversely proportional to strength of wave forcing relative to wind forcing.

The non-dimensional Stokes drift velocity appearing in Eqn. (3-2) is taken to be non-zero only in the downwind (x_1) direction and is defined by (Phillips O.M., 1967) as

$$U_1^s = \frac{\cosh(2k(x_3 + 1))}{2 \sinh^2(2k)} \quad (3-4)$$

and $U_2^s = U_3^s = 0$

Note that the dimensionless vertical coordinate x_3 extends from -1 at the bottom of the water column to +1 at the surface in the wind-driven shear flow simulations to be presented in upcoming chapters. Furthermore, the Stokes drift velocity profile in (3-4) decays with depth; its decay rate is inversely proportional to the dominant wavelength of the surface waves, λ . Expanding the C-L vortex force (i.e. the last term in (3-2)) and using the Stokes drift defined in (3-4), it can be shown that this force does not contribute to the downwind (x_1) momentum equation as the Stokes drift velocity is zero in cross-wind and vertical directions (x_2 and x_3).

As described earlier, the deviatoric LES subgrid scale (SGS) stress τ_{ij}^{LES} is generated by spatial filtering of the momentum equation. The SGS stress is modeled using the eddy viscosity-based dynamic Smagorinsky model as

$$\tau_{ij}^{LES} = 2\nu_t^{LES}\bar{S}_{ij} \quad (3-5)$$

where eddy viscosity is $\nu_t^{LES} = (C_s\bar{\Delta})^2|\bar{S}|$ with C_s denoting the Smagorinsky coefficient, $\bar{\Delta}$ is the width of the low pass spatial LES filter, $|\bar{S}|$ is the norm of the filtered strain rate tensor defined as $|\bar{S}| = (2\bar{S}_{ij}\bar{S}_{ij})^{1/2}$ and \bar{S}_{ij} is filtered strain rate tensor $\bar{S}_{ij} = (\bar{u}_{i,j} + \bar{u}_{j,i})/2$. Note that in practice, the low-pass filter used to obtain the spatially filtered equations in Eqn. 3.2 is implicitly set by an undefined combination of the numerical method and the grid discretizing the filtered equations. Thus, typically $\bar{\Delta}$ is representative of the characteristic grid-cell size. In this study, model coefficient $(C_s\bar{\Delta})^2$ is computed dynamically as described by (Lilly, 1992).

All flow variables and equations have been specified in dimensionless form for ease of presentation of important dimensionless parameters such as Re_τ and La_t . Henceforth all variables are taken as dimensional unless specified otherwise.

3.3 Flow Configuration

The flow domain for the LES in this study is shown in Fig 3.1. The flow is subjected to constant wind shear stress at the surface with zero normal flow. The surface stress is prescribed in such a way that the friction Reynolds number is $Re_\tau = 395$. Although in the coastal ocean Langmuir turbulence occurs under much higher Reynolds numbers (of $O(100,000)$), Tejada-Martinez et al. (2009) have shown that the turbulence simulated at a lower Reynolds number such as $Re_\tau = 395$ is able to scale up favorably to the turbulence measured in the field by Gargett and Wells (2007). This was done by re-dimensionalizing the LES velocity solution with wind stress friction velocity (u_τ) and water column half depth (δ) of the field measurements.

No-slip boundary condition is applied at the bottom wall of the domain in Figure 3.1 and periodic boundary condition is set in horizontal directions (x_1 and x_2). The latter condition is representative of a coastal shelf region far from (unaffected by) lateral boundaries.

The domain size in (x_1 and x_2) directions is $4\pi\delta$ and $8\pi\delta/3$ respectively. In the vertical (x_3) direction, the water depth is $H=2\delta$. The crosswind domain size $8\pi\delta/3$ is expected to be sufficiently wide to be able to resolve one Langmuir cell (i.e. one counter-rotating cell pair as sketched in Figure 2.1). This length ($8\pi\delta/3 \approx 4H$) falls within the range of values reported for span wise (crosswind) length of one Langmuir cell ($3H-6H$) during the field observations of (Gargett et al., 2004) and (Gargett and Wells, 2007).

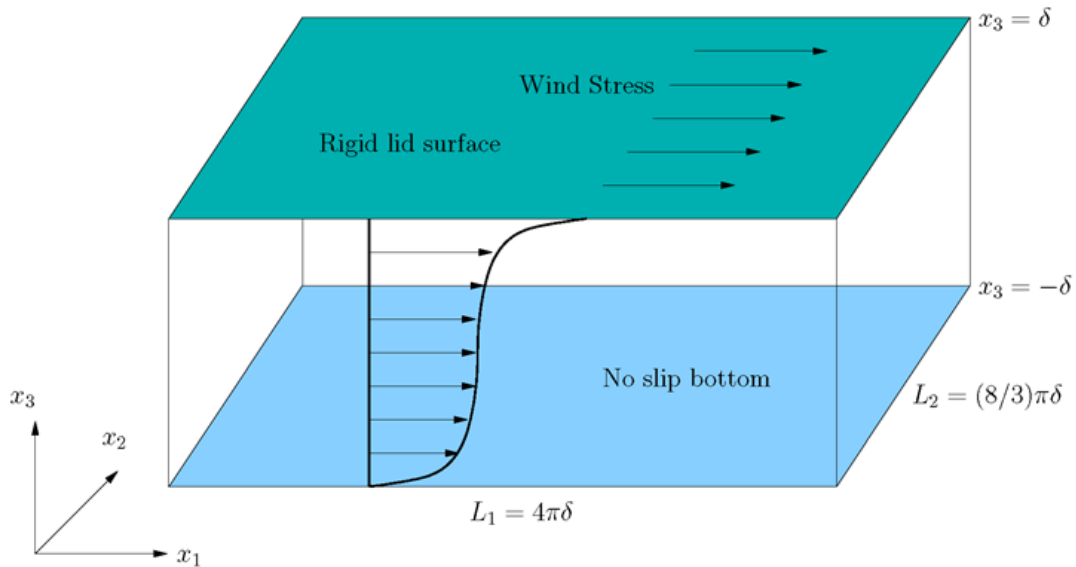


Figure 3.1 Computational domain and boundary conditions.

The computational grid for flows with and without LC (i.e. with and without Langmuir turbulence) contains 32 points in x_1 , 64 points in x_2 and 97 points in x_3 directions. This grid is uniform in x_1 and x_2 directions, however in the vertical direction (x_3), the grid is highly stretched

using a hyperbolic function in order to resolve the bottom and surface viscous boundary layers. Note that the grid stretching is symmetric about mid-depth in the vertical direction, thus both surface and bottom viscous boundary layers have the same resolution. In all simulations the first grid point off the wall or the surface is at a distance $x_3^+ = 1$, so the viscous sublayer ($0 < x_3^+ < 7$) is adequately resolved. Note that x_3^+ is a measure of the distance to the boundary (surface or bottom of the water column) in wall or plus units [*i. e.* $x_3^+ = zRe_\tau$], where z is the dimensionless distance to the bottom or to the surface.

The governing equations in (3-1) and (3-2) within the previously described domain configuration were solved using the hybrid spectral/finite-difference solver of Tejada-Martinez and Grosch (2007), in which horizontal (x_1 and x_2) directions are discretized using fast Fourier transforms and the vertical (x_3) direction is discretized using 5th and 6th order compact finite-difference schemes.

In the upcoming chapters, results from wind driven flows with or without LC are presented. Four simulations have been performed and corresponding wind and wave forcing parameters are summarized in Table 3.1 below. Main parameter inputs to the Craik-Leibovich vortex force appearing in the LES equations are the turbulent Langmuir number, La_t , representative of wind forcing relative wave forcing, and λ , the dominant wavelength of surface gravity waves generating Langmuir turbulence. Case-II in Table 3.1 with $La_t = 0.7$ and $\lambda = 12\delta$ corresponds to the wind and wave forcing conditions during the full-depth LC field measurements of (Gargett et al., 2004) and (Gargett and Wells, 2007). Note that wavelength $\lambda = 12\delta = 6H$ represents a shallow/intermediate surface wave and $\lambda = 8\delta/3 = 4H/3$ corresponds to a short (deep-water) wave. Figure 3.2 shows depth profiles of the Stokes drift velocity (appearing in the Craik-

Leibovich vortex force) and Stokes drift vertical shear. Stokes drift shear is important because it serves as the source for the generation of LC, as can be seen from the transport equation for downwind vorticity derived from the momentum equation with Craik-Leibovich vortex forcing (Holm, 1996).

Table 3.1 Summary of wind and wave forcing parameters in simulations.

Case-I	$La_t = \infty$	$\lambda = NA$	flow without LC
Case-II	$La_t = 0.7$	$\lambda = 6H$	flow with LC
Case-III	$La_t = 0.4$	$\lambda = 6H$	
Case-IV	$La_t = 0.7$	$\lambda = 4H/3$	

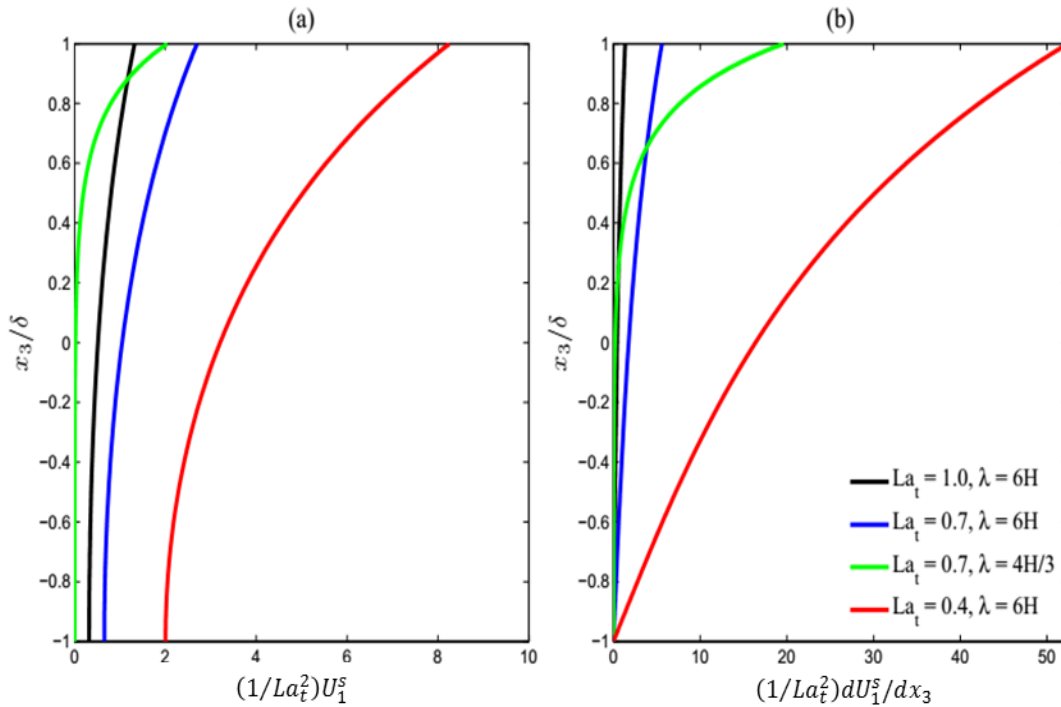


Figure 3.2 (a) Stokes drift velocity (b) Stokes drift velocity vertical shear

3.4 Turbulence Statistics

In the present study, we are interested in understanding the impact of Langmuir turbulence and associated full depth LC on surface and bottom log-layer dynamics and throughout the bulk of the water column in terms of quantities such as mean velocity, root mean square of velocity, sink and sources of resolved turbulent kinetic energy (TKE), energy transfers between TKE components and sink and sources of resolved Reynolds shear stress. Such understanding is crucial for the development of a turbulence parameterization that takes into account the influence of Langmuir turbulence and associated LC on the Reynolds stress appearing in the RANSS equations in (1-6).

In order to understand TKE and Reynolds shear stress behavior under the influence of Langmuir turbulence, a Reynolds decomposition of the LES-resolved variables is first adopted:

$$\bar{u}_i = \langle \bar{u}_i \rangle + \bar{u}'_i \quad (3-6)$$

where the first term on the right hand side is mean resolved velocity and the second term on the RHS is resolved velocity fluctuation. The Reynolds-averaging operation, denoted by brackets, is performed by averaging the LES solution in time and over downwind (x_1) and crosswind (x_2) directions. This decomposition and Reynolds-averaging the Craik-Leibovich momentum equation in (3-2) can be shown to lead to transport equations for the Reynolds shear stress, turbulent kinetic energy (TKE) and TKE components.

The general transport equation for the resolved Reynolds stress tensor $\langle \bar{u}'_i \bar{u}'_j \rangle$ is written as

$$\frac{\partial \langle \bar{u}'_i \bar{u}'_j \rangle}{\partial t} + \langle \bar{u}_k \rangle \frac{\partial \langle \bar{u}'_i \bar{u}'_j \rangle}{\partial x_k} = P_{ij} + Q_{ij} + T_{ij} + T_{ij}^{sgs} + D_{ij} + A_{ij} + B_{ij} + \varepsilon_{ij} + \varepsilon_{ij}^{sgs} \quad (3-7)$$

where

$$P_{ij} = -\langle \bar{u}'_i \bar{u}'_k \rangle \frac{\partial \langle \bar{u}_j \rangle}{\partial x_k} - \langle \bar{u}'_j \bar{u}'_k \rangle \frac{\partial \langle \bar{u}_i \rangle}{\partial x_k} \quad (\text{mean shear production rate})$$

$$Q_{ij} = \frac{1}{La_t^2} [\epsilon_{jlk} U_l^s \langle \bar{\omega}'_k \bar{u}'_i \rangle + \epsilon_{ilk} U_l^s \langle \bar{\omega}'_k \bar{u}'_j \rangle] \quad (\text{C-L (Langmuir) forcing rate})$$

$$T_{ij} = -\frac{\partial \langle \bar{u}'_i \bar{u}'_j \bar{u}'_k \rangle}{\partial x_k} \quad (\text{turbulent transport rate})$$

$$T_{ij}^{sgs} = \frac{\partial}{\partial x_k} [\langle \bar{u}'_i \tau_{jk}^{d'} \rangle + \langle \bar{u}'_j \tau_{ik}^{d'} \rangle] \quad (\text{SGS transport rate})$$

$$D_{ij} = \frac{1}{Re_\tau} \frac{\partial^2 \langle \bar{u}'_i \bar{u}'_j \rangle}{\partial x_k^2} \quad (\text{viscous diffusion rate})$$

$$A_{ij} = -\frac{\partial}{\partial x_k} [\delta_{jk} \langle \Pi' \bar{u}'_i \rangle + \delta_{ik} \langle \Pi' \bar{u}'_j \rangle] \quad (\text{pressure transport rate})$$

$$B_{ij} = 2 \langle \bar{\Pi}' \bar{S}'_{ij} \rangle \quad (\text{pressure-strain redistribution rate})$$

$$\epsilon_{ij} = -\frac{2}{Re_\tau} \left\langle \frac{\partial \bar{u}'_i}{\partial x_k} \frac{\partial \bar{u}'_j}{\partial x_k} \right\rangle \quad (\text{viscous dissipation rate})$$

$$\epsilon_{ij}^{sgs} = -\left\langle \tau_{ik}^{d'} \frac{\partial \bar{u}'_j}{\partial x_k} \right\rangle - \left\langle \tau_{jk}^{d'} \frac{\partial \bar{u}'_i}{\partial x_k} \right\rangle \quad (\text{SGS dissipation rate})$$

In the flows simulated here, the dominant Reynolds shear stress component is $\langle \bar{u}'_1 \bar{u}'_3 \rangle$. Furthermore, time, downwind (x_1) and crosswind (x_2) derivatives of Reynolds averaged quantities are zero based on the definition given in (3-6) above. Taking this into consideration, expanding the pressure $\bar{\Pi}$ following its definition in (3-3) and combining the Langmuir forcing rate with the pressure transport rate and pressure strain correlation, the transport equation for $\langle \bar{u}'_1 \bar{u}'_3 \rangle$ is given as

$$0 = P_{13} + Q_{13} + T_{13} + T_{13}^{sgs} + D_{13} + A_{13} + B_{13} + \varepsilon_{13} + \varepsilon_{13}^{sgs} \quad (3-8)$$

where

$$P_{13} = -\langle \bar{u}'_3 \bar{u}'_3 \rangle \frac{d\langle \bar{u}'_1 \rangle}{dx_3} \quad (\text{mean shear production rate})$$

$$Q_{13} = \frac{1}{La_t^2} \langle \bar{u}'_1 \bar{u}'_1 \rangle \frac{dU_1^s}{dx_3} \quad (\text{Stokes drift shear production rate})$$

$$T_{13} = -\frac{d\langle \bar{u}'_1 \bar{u}'_3 \bar{u}'_3 \rangle}{dx_3} \quad (\text{turbulent transport rate})$$

$$T_{13}^{sgs} = \frac{d\langle \bar{u}'_3 \tau_{13}^{d'} \rangle}{dx_3} \quad (\text{SGS transport rate})$$

$$D_{13} = \frac{1}{Re_\tau} \frac{d^2 \langle \bar{u}'_1 \bar{u}'_3 \rangle}{dx_3^2} \quad (\text{viscous diffusion rate})$$

$$A_{13} = -\frac{d\langle \bar{P}' \bar{u}'_1 \rangle}{dx_3} \quad (\text{pressure transport rate})$$

$$B_{13} = 2\langle \bar{P}' \bar{S}'_{13} \rangle \quad (\text{pressure-strain redistribution rate})$$

$$\varepsilon_{13} = -\frac{2}{Re_\tau} \left\langle \frac{\partial \bar{u}'_1}{\partial x_3} \frac{\partial \bar{u}'_3}{\partial x_3} \right\rangle \quad (\text{viscous dissipation rate})$$

$$\varepsilon_{13}^{sgs} = -\left\langle \tau_{13}^{d'} \frac{\partial \bar{u}'_3}{\partial x_3} \right\rangle - \left\langle \tau_{33}^{d'} \frac{\partial \bar{u}'_1}{\partial x_3} \right\rangle \quad (\text{SGS dissipation rate})$$

Similarly, the transport equations for $\langle \bar{u}'_1 \bar{u}'_1 \rangle$ is

$$0 = P_{11} + T_{11} + T_{11}^{sgs} + D_{11} + A_{11} + B_{11} + \varepsilon_{11} + \varepsilon_{11}^{sgs} \quad (3-9)$$

$$P_{11} = -2\langle \bar{u}'_1 \bar{u}'_3 \rangle \frac{d\langle \bar{u}'_1 \rangle}{dx_3} \quad (\text{mean shear production rate})$$

$$T_{11} = -\frac{d\langle \bar{u}'_1 \bar{u}'_2 \bar{u}'_3 \rangle}{dx_3} \quad (\text{turbulent transport rate})$$

$$T_{11}^{sgs} = 2\frac{d\langle \bar{u}'_1 \tau_{13}^{d'} \rangle}{dx_3} \quad (\text{SGS transport rate})$$

$$D_{11} = \frac{1}{Re} \frac{d^2\langle \bar{u}'_1 \bar{u}'_1 \rangle}{dx_3^2} \quad (\text{viscous diffusion rate})$$

$$A_{11} = -2\frac{d\langle \bar{P}' \bar{u}'_1 \rangle}{dx_1} \quad (\text{pressure transport rate})$$

$$B_{11} = 2\langle \bar{P}' \bar{S}'_{11} \rangle \quad (\text{pressure-strain redistribution rate})$$

$$\varepsilon_{11} = -\frac{2}{Re_\tau} \left\langle \frac{\partial \bar{u}'_1}{\partial x_3} \frac{\partial \bar{u}'_1}{\partial x_3} \right\rangle \quad (\text{viscous dissipation rate})$$

$$\varepsilon_{11}^{sgs} = -2 \left\langle \tau_{13}^{d'} \frac{\partial \bar{u}'_1}{\partial x_3} \right\rangle \quad (\text{SGS dissipation rate})$$

The transport equation for $\langle \bar{u}'_2 \bar{u}'_2 \rangle$ is

$$0 = P_{22} + T_{22} + T_{22}^{sgs} + D_{22} + A_{22} + B_{22} + \varepsilon_{22} + \varepsilon_{22}^{sgs} \quad (3-10)$$

$$P_{22} = -2\langle \bar{u}'_2 \bar{u}'_3 \rangle \frac{d\langle \bar{u}'_2 \rangle}{dx_3} \quad (\text{mean shear production rate})$$

$$T_{22} = -\frac{d\langle \bar{u}'_2 \bar{u}'_2 \bar{u}'_3 \rangle}{dx_3} \quad (\text{turbulent transport rate})$$

$$T_{22}^{sgs} = 2\frac{d\langle \bar{u}'_2 \tau_{23}^{d'} \rangle}{dx_3} \quad (\text{SGS transport rate})$$

$$D_{22} = \frac{1}{Re_\tau} \frac{d^2 \langle \bar{u}'_2 \bar{u}'_2 \rangle}{dx_3^2} \quad (\text{viscous diffusion rate})$$

$$A_{22} = -2 \frac{d \langle \bar{P}' \bar{u}'_2 \rangle}{dx_2} \quad (\text{pressure transport rate})$$

$$B_{22} = 2 \langle \bar{P}' \bar{S}'_{22} \rangle \quad (\text{pressure-strain redistribution rate})$$

$$\varepsilon_{22} = -\frac{2}{Re_\tau} \left\langle \frac{\partial \bar{u}'_2}{\partial x_3} \frac{\partial \bar{u}'_2}{\partial x_3} \right\rangle \quad (\text{viscous dissipation rate})$$

$$\varepsilon_{22}^{sgs} = -2 \left\langle \tau_{23}^{d'} \frac{\partial \bar{u}'_2}{\partial x_3} \right\rangle \quad (\text{SGS dissipation rate})$$

The transport equations for $\langle \bar{u}'_3 \bar{u}'_3 \rangle$ is

$$0 = P_{33} + Q_{33} + T_{33} + T_{33}^{sgs} + D_{33} + A_{33} + B_{33} + \varepsilon_{33} + \varepsilon_{33}^{sgs} \quad (3-11)$$

$$P_{33} = -2 \langle \bar{u}'_3 \bar{u}'_3 \rangle \frac{d \langle \bar{u}'_3 \rangle}{dx_3} \quad (\text{mean shear production rate})$$

$$Q_{33} = -\frac{2}{La_t^2} \langle \bar{u}'_1 \bar{u}'_3 \rangle \frac{dU_1^s}{dx_3} \quad (\text{Stokes drift production rate})$$

$$T_{33} = -\frac{\partial \langle \bar{u}'_3 \bar{u}'_3 \bar{u}'_3 \rangle}{\partial x_3} \quad (\text{turbulent transport rate})$$

$$T_{33}^{sgs} = 2 \frac{d \langle \bar{u}'_3 \tau_{33}^{d'} \rangle}{dx_3} \quad (\text{SGS transport rate})$$

$$D_{33} = \frac{1}{Re_\tau} \frac{d^2 \langle \bar{u}'_3 \bar{u}'_3 \rangle}{dx_3^2} \quad (\text{viscous diffusion rate})$$

$$A_{33} = -2 \frac{d \langle \bar{P}' \bar{u}'_3 \rangle}{dx_3} \quad (\text{pressure transport rate})$$

$$B_{33} = 2\langle \bar{P}' \bar{S}'_{33} \rangle \quad (\text{pressure-strain redistribution rate})$$

$$\varepsilon_{33} = -\frac{2}{Re_\tau} \left\langle \frac{\partial \bar{u}'_3}{\partial x_3} \frac{\partial \bar{u}'_3}{\partial x_3} \right\rangle \quad (\text{viscous dissipation rate})$$

$$\varepsilon_{33}^{sgs} = -2 \left\langle \tau_{33}^d \frac{\partial \bar{u}'_3}{\partial x_3} \right\rangle \quad (\text{SGS dissipation rate})$$

Similarly, the transport equation for resolved turbulent kinetic energy, $\bar{q} \equiv \langle \bar{u}'_i \bar{u}'_i \rangle / 2$ can be expressed as

$$0 = P + Q + T + T^{sgs} + D + A + \varepsilon + \varepsilon^{sgs} \quad (3-12)$$

where

$$P = \langle \bar{u}'_1 \bar{u}'_3 \rangle \frac{d\langle \bar{u}'_1 \rangle}{dx_3} \quad (\text{mean shear production rate})$$

$$Q = -\frac{1}{La_t^2} \langle \bar{u}'_1 \bar{u}'_3 \rangle \frac{\partial U_1^s}{\partial x_3} \quad (\text{Stokes drift shear production rate})$$

$$T = -\frac{d\langle \bar{q} \bar{u}'_3 \rangle}{dx_3} \quad (\text{turbulent transport rate})$$

$$T^{sgs} = \frac{d\langle \bar{u}'_1 \tau_{13}^d \rangle}{dx_3} \quad (\text{SGS transport rate})$$

$$D = \frac{1}{Re_\tau} \frac{d^2 \bar{q}}{dx_3^2} \quad (\text{viscous diffusion rate})$$

$$A = -\frac{d\langle \bar{p}' \bar{u}'_3 \rangle}{dx_3} \quad (\text{pressure transport rate})$$

$$\varepsilon = -\frac{1}{Re_\tau} \left\langle \frac{\partial \bar{u}'_1}{\partial x_3} \frac{\partial \bar{u}'_1}{\partial x_3} \right\rangle \quad (\text{viscous dissipation rate})$$

$$\varepsilon^{sgs} = -\langle \tau_{13}^d \bar{S}'_{13} \rangle \quad (\text{SGS dissipation rate})$$

Simulations conducted here run until the flows reach statistical equilibrium (i.e. until horizontally and time averaged quantities remain nearly the same for time windows of increasing size). Furthermore, for flows under statistical equilibrium, the budget terms on the right hand sides of (3-7) through (3-12) should sum to zero.

In the next chapters, LES resolved fields are used to compute the budget terms in equations (3-7) through (3-12). Analysis of these budget terms will prove to be useful for understanding the impact of shallow water Langmuir turbulence on surface and bottom boundary layer dynamics and ultimately for the determination of a Reynolds shear stress turbulence parameterization that is able to account for shallow water Langmuir turbulence and associated full-depth LC.

3.5 Chapter Summary

In this chapter governing LES equations and Craik-Leibovich (C-L) vortex forcing were discussed. The flow domain for the simulations performed was also presented. Additionally, transport equations for turbulent kinetic energy and resolved Reynolds stress components were described. In upcoming chapters, LES velocity fields will be used to analyze surface and bottom boundary layer dynamics in terms of turbulence statistics including the budgets previously described and overall turbulence structure.

4 Surface Dynamics in LES of Langmuir Turbulence with Full-Depth LC

4.1 Introduction

Research on the relationship between the interior of the water column and near-surface dynamics has contributed towards physical understanding of the role of the ocean on air-sea interaction and climate. Physical processes such as surface heat and mass transfer which affect the weather and climate as well as the water column stability and chemical composition of the ocean are often governed largely by processes taking place in the few tens of meters of water adjoining the ocean surface. Understanding the near-surface dynamics in the presence of Langmuir turbulence is important given the strong impact of LC on surface mass transfer efficiency recently evidenced by the laboratory measurements of (Veron and Melville, 2001) and by the computations of (Akan et al., 2013).

This chapter presents a study of the structure of Langmuir turbulence and full-depth LC and their effect on momentum mixing and near surface dynamics. The analysis is based on LES-resolved fields resulting from the flow configurations described in the previous chapter. This analysis is required in order to determine a new Reynolds shear stress parameterization taking into account shallow water Langmuir turbulence.

4.2 Turbulence Structure

Coherent structures or eddies are features of the turbulent flow field. These structures are flow patterns that can be recognized atop the chaotic turbulent motions. These coherent structures are continuously evolving, being created and destroyed. In LES with Craik-Leibovich vortex forcing (or Langmuir forcing) in the momentum equation, the forcing serves to generate Langmuir turbulence. In homogenous shallow water, the largest, most coherent and persistent scales of this turbulence regime consist of full-depth LC. Next, the coherent structures in wind-driven flow with and without LC (i.e. with and without Langmuir forcing) are described. Note that throughout the rest of this dissertation, the terminology “with LC” and “without LC” are taken to be equivalent to “with Langmuir turbulence” and “without Langmuir turbulence”, respectively. This has been done because historically Langmuir turbulence has been referred to as Langmuir circulation.

In flow without LC, downwind velocity fluctuations visualized on horizontal ($x_1 - x_2$) planes within the bottom and surface viscous sublayers are characterized by downwind (x_1) elongated small-scale streaks alternating in sign in the crosswind (x_2) direction (Figure 4.1a and Figure 4.2d). These small-scale streaks are typical of classical viscous sublayers (Smith and Metzler, 1983). On horizontal planes closer to the middle of the water column, downwind length and crosswind width of the streaks become greater. In the middle of the water column (Figure 4.1d) the downwind elongation of the streaks covers the entire length of the domain and the crosswind width of the streaks is close to $H = 2\delta$ (i.e. the water column depth). These large scale streaks are similar in structure and size to Couette streaks found in classical Couette flow, occurring between parallel no-slip plates moving in opposite direction (Pappavasilou and

Hanratty, 1997). Thus, henceforth we refer to the streaks in the present LES of wind-driven flow without LC as Couette streaks.

Simulations with LC are initiated by turning on the CL vortex force when the wind-driven flow without LC is in statistical equilibrium. The CL vortex force causes a merging of the Couette streaks, giving rise to streaks of larger crosswind size (denoted as Langmuir streaks) once the flow achieves a new statistical equilibrium state (see Figure 4.1 e–h and Figure 4.2 e–h). Note that the Langmuir streak signature is evident from the bottom viscous sublayer up through the surface viscous sublayer. This is not the case for Couette streaks, which have strong signature at mid-depth but have weaker signature elsewhere (see Figure 4.1 a–d and Figure 4.2 a–d).

As noted by Pappavasilou and Hanratty (1997), in Couette flow, the mean streamwise velocity is asymmetric, thus production of turbulent kinetic energy by mean velocity vertical shear is everywhere non-zero from wall to wall. Such production favors the growth of near wall turbulent structures outward towards the core region, and ultimately structures that extend from wall to wall. These characteristics also apply to the wind-driven flow without CL vortex forcing in the present study and are responsible for the Couette streaks previously analyzed. Ultimately, these Couette streaks give rise to the wider Langmuir streaks once the CL vortex force is turned on, as mentioned earlier.

Couette and Langmuir streaks are coherent in the downwind direction (x_1). This suggests averaging velocity fluctuations over x_1 in order to stress coherency in this direction. This also helps reveal the crosswind (x_2)–vertical (x_3) variation of the wall-to-wall structures described

previously. In the present work, the terminology “wall-to-surface (full-depth) structures” is more appropriate than “wall-to-wall”.

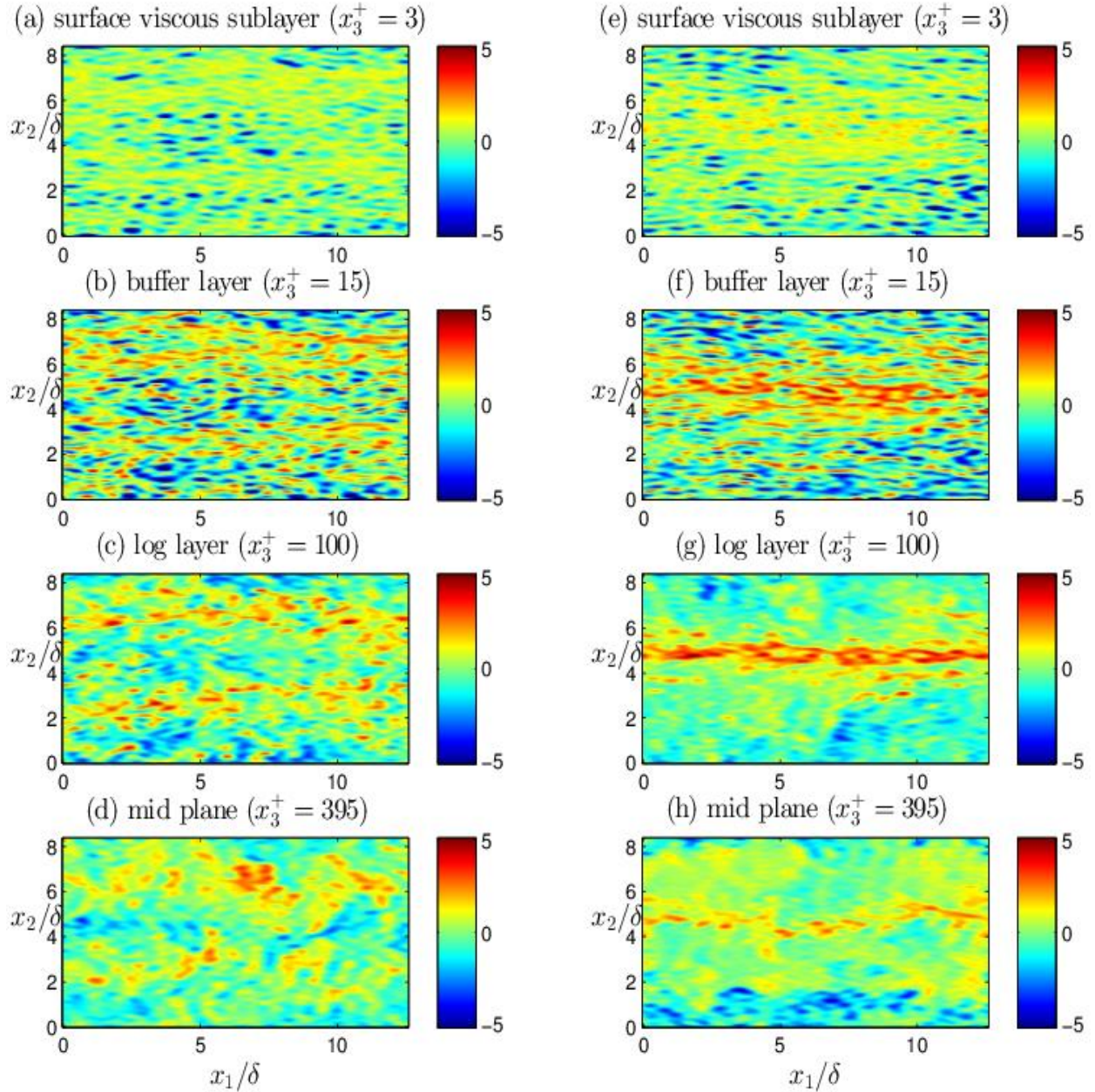


Figure 4.1 Snapshots of instantaneous downwind velocity fluctuation on horizontal ($x_1 - x_2$) planes at different depths in the upper half of the water column. Depths are given in terms of x_3^+ denoting distance from the surface of the water column in plus units. Downwind velocity fluctuation is scaled by wind stress friction velocity: \bar{u}'_1/u_τ . Wind-driven flow without LC ($La_t = \infty$) is shown in the panels on the left (a-d) and wind-driven flow with LC ($La_t = 0.7 \lambda = 6H$) is shown in the panels on the right (e-h).

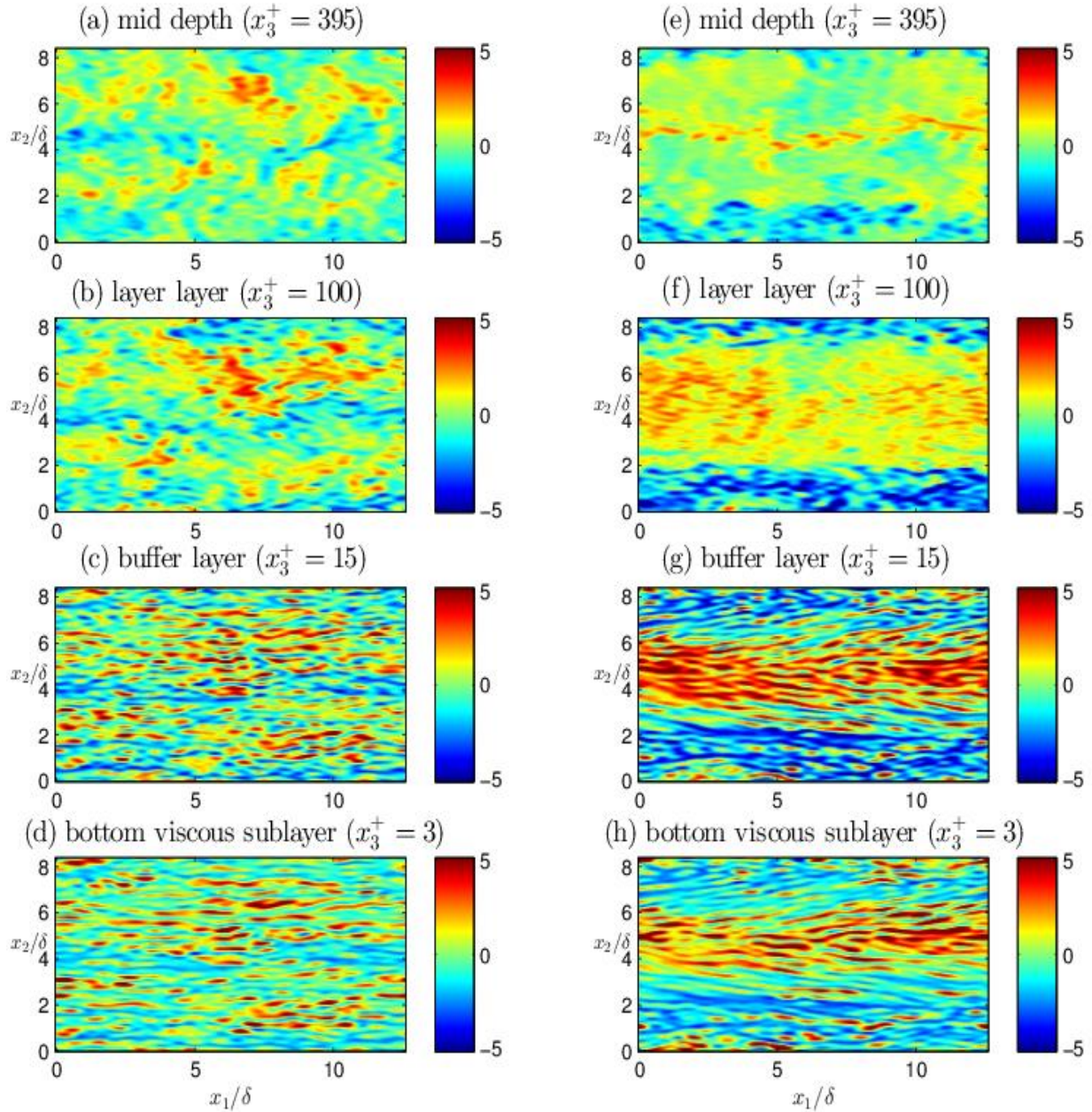


Figure 4.2 Snapshots of instantaneous downwind velocity fluctuation on the horizontal ($x_1 - x_2$) planes at different depths in the bottom half of the water column. Depths are given in terms of x_3^+ denoting distance from the bottom of the water column in plus units. Downwind velocity fluctuation is scaled by wind stress friction velocity: \bar{u}_1'/u_τ . Wind-driven flow without LC ($La_t = \infty$) is shown in (a)–(d), and wind-driven flow with LC ($La_t = 0.7 \lambda = 6H$) is shown in (e)–(h).

Figure 4.3 through 4-6 show the $x_2 - x_3$ variation of all three components of x_1 -averaged (partially averaged) velocity fluctuations in wind-driven flows with and without CL vortex

forcing (i.e. with and without LC). All flows with CL vortex forcing (Figure 4.3d–f and Figures 4.4 through 4.6) are characterized by a full-depth one-cell structure in close agreement with the full-depth Langmuir cells observed in the field measurements of Gargett and Wells (2007) and Gargett et al (2004). For example, the single-cell structure in the flows with CL vortex forcing possesses a crosswind width $\approx 4H$ (8δ) consistent with the field measurements of Gargett and collaborators. Note that although the computational domain size in the crosswind direction was chosen following the expected Langmuir cell crosswind width as described earlier, it has been confirmed that the crosswind length of the domain does not set (or force) the crosswind length of the resolved Langmuir cell. Confirmation was made by Tejada-Martinez and Grosch (2007) by performing LES of wind-driven flow with CL vortex forcing in which the crosswind length of the domain was double the length of the one chosen here. In that simulation they were able to resolve two full-depth Langmuir cells each with crosswind width consistent with the measurements of Gargett and collaborators. Other favorable comparisons between flows with CL vortex forcing and field measurements during episodes of full-depth LC are described by Tejada-Martinez and Grosch (2007) and Tejada-Martinez et al (2009). Thus, henceforth, flows with CL vortex forcing will be continued to be referred to as flows with LC and conversely. Here we focus on the impact of wind and wave forcing parameters (U and λ) on the structure of the full-depth Langmuir cell generated and on surface log layer dynamics, which had not been explored in the earlier studies.

In flows with LC, crosswind velocity fluctuations are intensified near the surface and exhibit a surface convergence zone corresponding to the surface convergence of the Langmuir cell (Figure 4.4a and d). Surface convergence leads to the generation of the LC downwelling limb, characterized by negative vertical velocity fluctuations (Figure 4.4b and e). Furthermore, the

downwelling limb coincides with a region of positive downwind velocity fluctuations (Figure 4.4c and f) which serves to enhance the mean downwind current within this zone, as sketched in Figure 2.1 in Chapter 2.

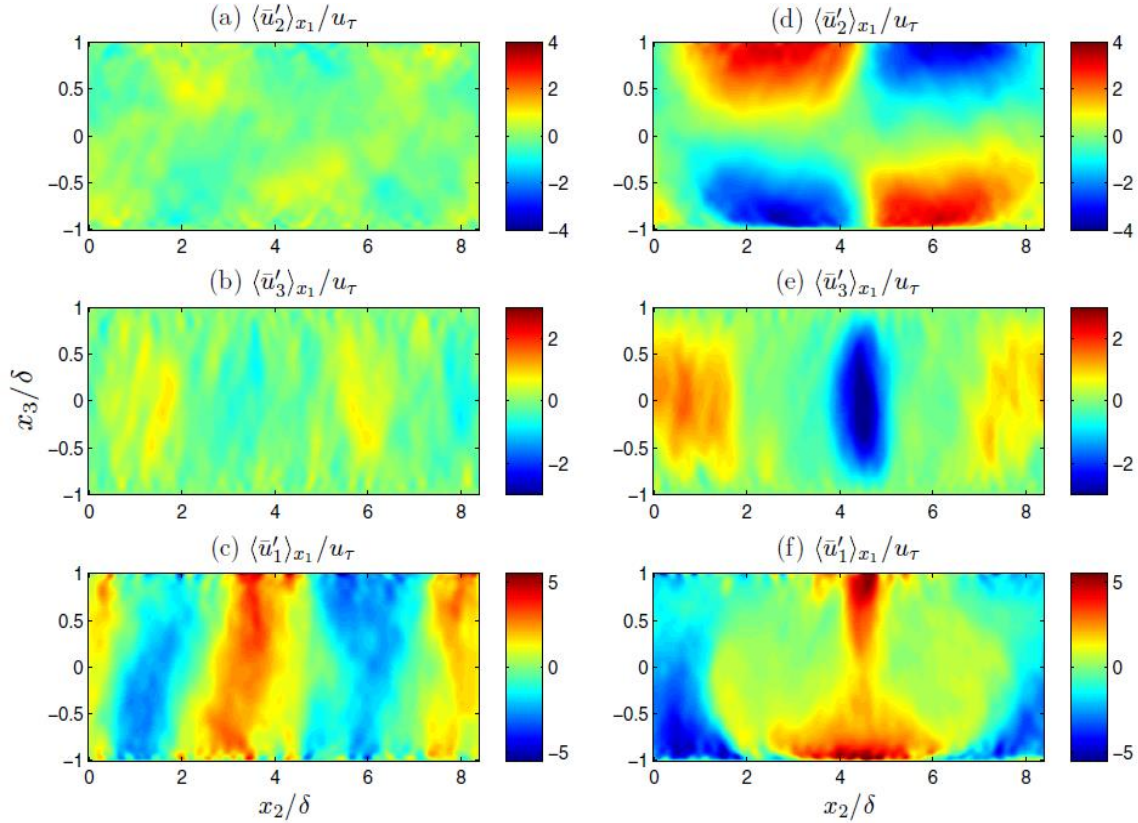


Figure 4.3 Instantaneous velocity fluctuations averaged over the downwind (x_1) direction in flow without LC (a)–(c) and in flow with LC with $La_t = 0.7$ and $\lambda = 6H$ (d)–(f). First row of panels shows crosswind velocity fluctuation, the second row shows vertical velocity fluctuation and the third row shows downwind fluctuation.

A decrease in turbulent Langmuir number from $La_t = 1.0$ down to $La_t = 0.7$ while holding the wavelength of surface waves constant at $\lambda = 6H$ leads to an intensification of the averaged velocity fluctuations associated with full-depth LC, especially in terms of crosswind velocity fluctuation at the surface and bottom of the water column (Figure 4.4a and d). A decrease in La_t from 0.7 to 0.4 leads to a re-structuring of the cell reflected through higher averaged vertical velocities within the upwelling limb of the cell (Figure 4-5b and e) as well as

more intense crosswind velocity fluctuation at the surface, but less intense at the bottom (Figure 4-5a and d) .

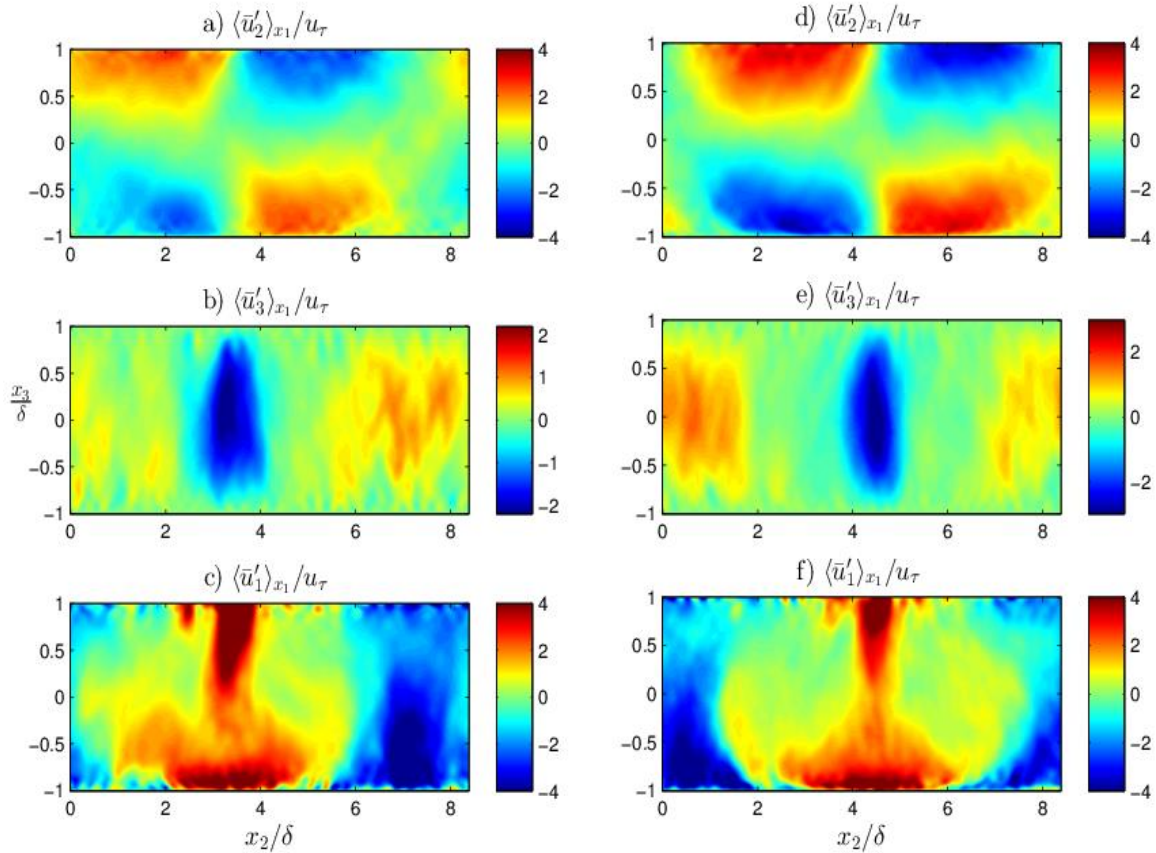


Figure 4.4 Instantaneous velocity fluctuations averaged over the downwind (x_1) direction in flow with LC with $La_t = 1.0$ and $\lambda = 6H$ (a)–(c) and in flow with LC with $La_t = 0.7$ and $\lambda = 6H$ (d)–(f). First row of panels shows crosswind velocity fluctuation, the second row shows vertical velocity fluctuation and the third row shows downwind fluctuation.

A decrease in λ from $6H$ to $4H/3$ with La_t fixed at 0.7 leads to less coherent LC, characterized by averaged velocity fluctuations weaker in magnitude, especially in terms of crosswind and vertical velocity fluctuations (see Figure 4.6a and d and Figure 4.6b and e, respectively). This is to be expected because the magnitude of the CL vortex force and Stokes drift velocity shear decay with depth faster for smaller values of λ (see Figure 3.2).

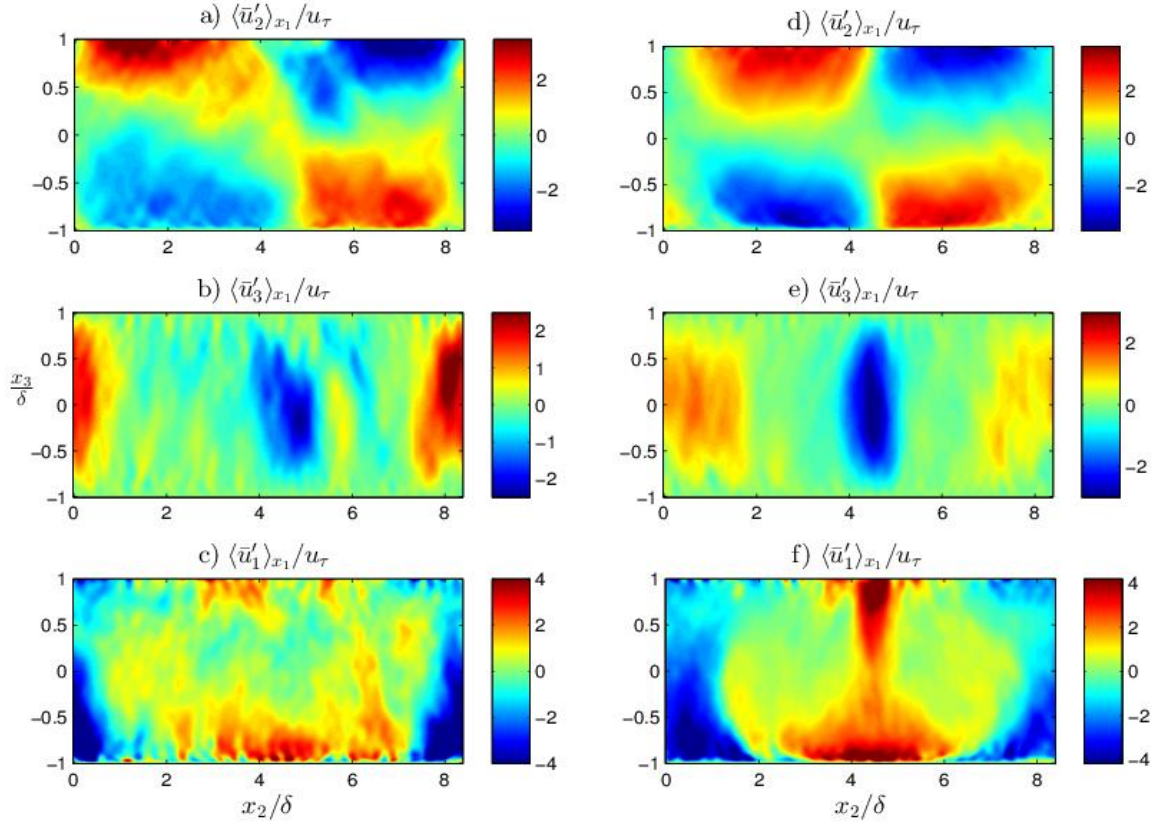


Figure 4.5 Instantaneous velocity fluctuations averaged over the downwind (x_1) direction in flow with LC with $La_t = 0.4$ and $\lambda = 6H$ (a)–(c) and in flow with LC with $La_t = 0.7$ and $\lambda = 6H$ (d)–(f). First row of panels shows crosswind velocity fluctuation, the second row shows vertical velocity fluctuation and the third row shows downwind fluctuation.

Finally, note that the flow without the CL vortex force (i.e. flow without LC) is characterized by a two-cell structure (Figure 4.3a–c) which is weaker and less coherent than the LC resolved in the flows with CL forcing. The two-cell structure is similar in size and structure to Couette cells resolved in the LES of Couette flow of Papavassiliou and Hanratty (1997).

The structure of the turbulence in flows with and without LC is further investigated by analyzing the normal components of the resolved Reynolds stress (Figure 4.7). The main difference between the flow without LC and the flows with LC is that in the former the stresses are ordered as $\langle \bar{u}'_1 \bar{u}'_1 \rangle > \langle \bar{u}'_2 \bar{u}'_2 \rangle > \langle \bar{u}'_3 \bar{u}'_3 \rangle$ throughout the entire water column (Fig. 4.7a). This ordering is typical of shear-dominated turbulence.

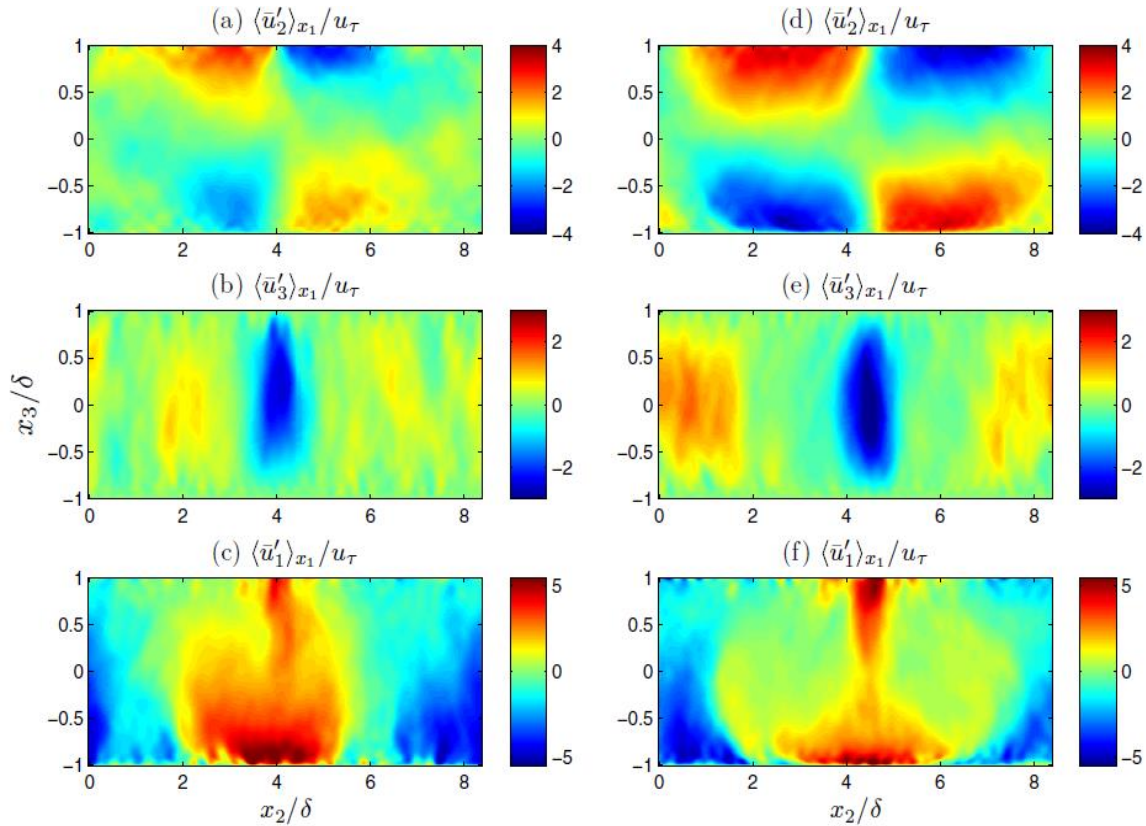


Figure 4.6 Instantaneous velocity fluctuations averaged over the downwind (x_1) direction in flow with LC with $La_t = 0.7$ and $\lambda = 4H/3$ (a)–(c) and in flow with LC with $La_t = 0.7$ and $\lambda = 6H$ (d)–(f).

In the flows with LC this ordering is changed dramatically, especially in the middle and the upper half of the water column (Fig. 4.7b). For example, in the flow with $La_t = 0.7$ and $\lambda = 6H$, in the middle of the water column $\langle \bar{u}'_1 \bar{u}'_1 \rangle \approx \langle \bar{u}'_3 \bar{u}'_3 \rangle > \langle \bar{u}'_2 \bar{u}'_2 \rangle$. Flow with $La_t = 0.7$ and $\lambda = 6H$ exhibits elevated values of $\langle \bar{u}'_2 \bar{u}'_2 \rangle$ near the bottom and the surface, relative to the flow without LC. This can be attributed to the surface convergence and bottom divergence zones of the LES-resolved full-depth LC which serve to increase the magnitudes of crosswind velocity fluctuations. A similar trend is also observed in the flow with LC with $La_t = 0.7$ and $\lambda = 4H/3$ (Fig. 4.7c); however, the near-bottom and near-surface elevated values of crosswind velocity fluctuations are not as prominent due to weaker full-depth LC.

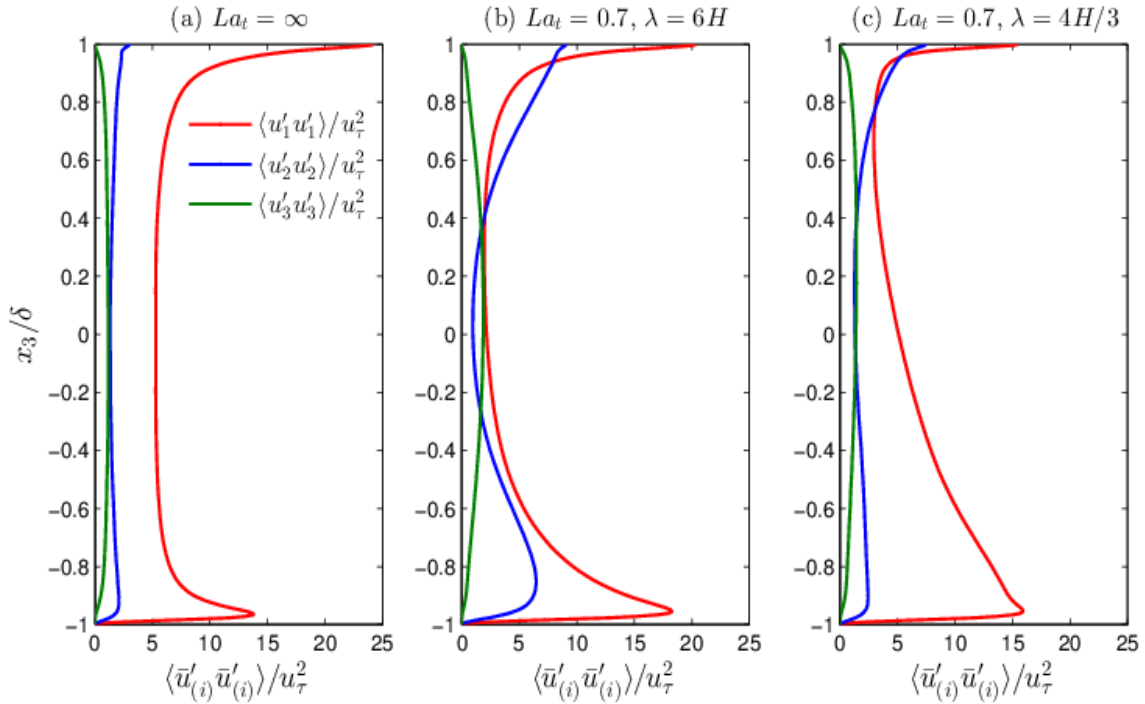


Figure 4.7 Normal components of the resolved Reynolds stress in flow without LC (a) and in flows with LC (b), (c).

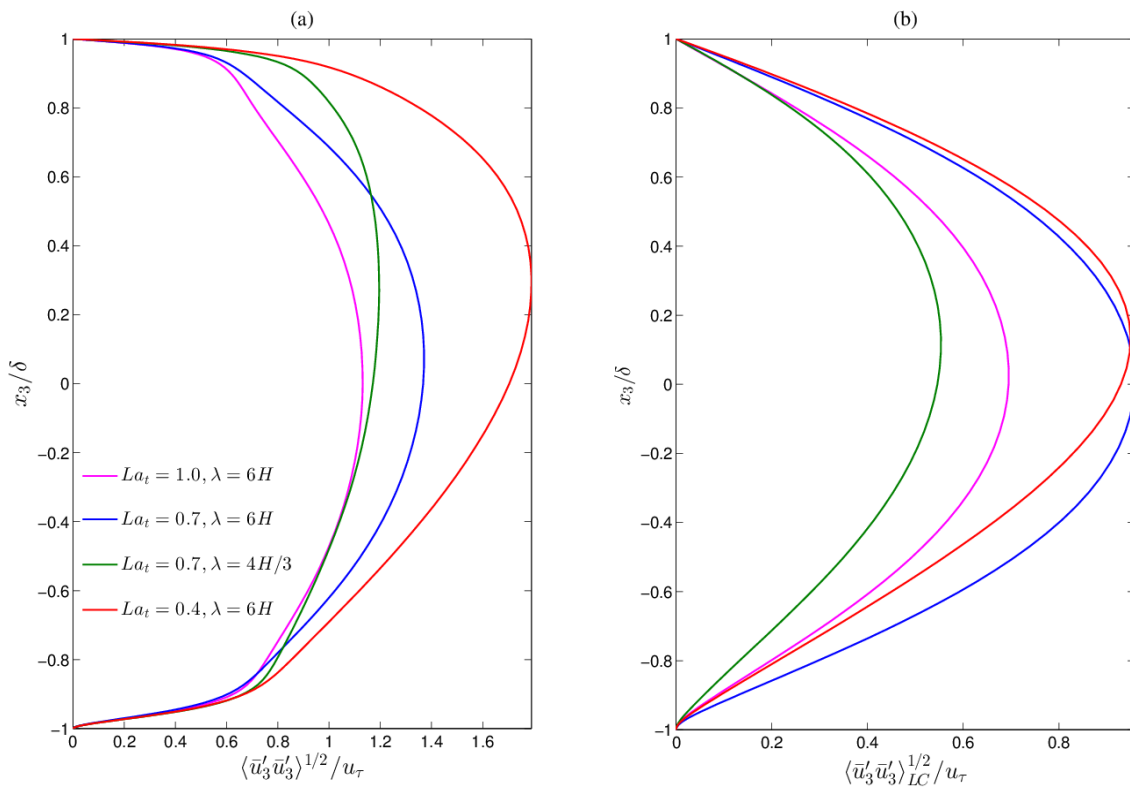


Figure 4.8 (a) Root mean square (rms) of resolved vertical velocity and (b) contribution to resolved vertical velocity rms from full-depth LC.

Of particular interest is a comparison in $\langle \bar{u}'_3 \bar{u}'_3 \rangle$ between the LC flows with different La_t and λ . Figure 4.8 (a) shows that the flow with $(La_t = 0.7, \lambda = 4H/3)$ is characterized by higher $\langle \bar{u}'_3 \bar{u}'_3 \rangle$ near the surface, compared to the flow with $(La_t = 0.7, \lambda = 6H)$. This can be attributed to intensification of small scale near-surface eddies in the former case (seen in Figure 4.9b, c) despite the weaker full-depth cells in the $\lambda = 4H/3$ case compared to the $\lambda = 6H$ case (observed earlier in Figure 4.4). Intensification of near-surface eddies in the $(La_t = 0.7, \lambda = 4H/3)$ case relative to the $(La_t = 0.7, \lambda = 6H)$ case is due to higher near-surface Stokes drift shear in the former (seen in Figure 3.2.b in Chapter 3).

Figure 4.8b shows $\langle \bar{u}'_3 \bar{u}'_3 \rangle_{LC}$ defined as the contribution from full-depth LC to overall vertical velocity variance $\langle \bar{u}'_3 \bar{u}'_3 \rangle$. The contribution $\langle \bar{u}'_3 \bar{u}'_3 \rangle_{LC}$ is computed using a triple decomposition of resolved velocity (Tejada-Martinez et al., 2007; Akan et al., 2013) leading to

$$\langle \bar{u}'_3 \bar{u}'_3 \rangle_{LC} = \langle \langle \bar{u}'_3 \rangle_{t,x_1} \langle \bar{u}'_3 \rangle_{t,x_1} \rangle \quad (4-1)$$

In this expression the interior brackets denote a partial Reynolds averaging over time and downwind direction (x_1) (the same averaging used to define the partial averaged fluctuations in Figures 4.3 through 4.6). The outer bracket in Eqn. (4-1) denotes full Reynolds averaging over time, downwind (x_1) and crosswind directions (x_2). Figure 4.8b shows that the vertical velocity variance associated with full-depth LC is much less in the case with $(La_t = 0.4, \lambda = 4H/3)$ than in the cases with $(La_t = 0.7, \lambda = 6H)$ and $(La_t = 0.4, \lambda = 6H)$. This is consistent with Figure 4.5 and Figure 4.6 discussed earlier showing that the strength of LC in the case with $\lambda = 4H/3$ is weaker than in the two other cases with $\lambda = 6H$.

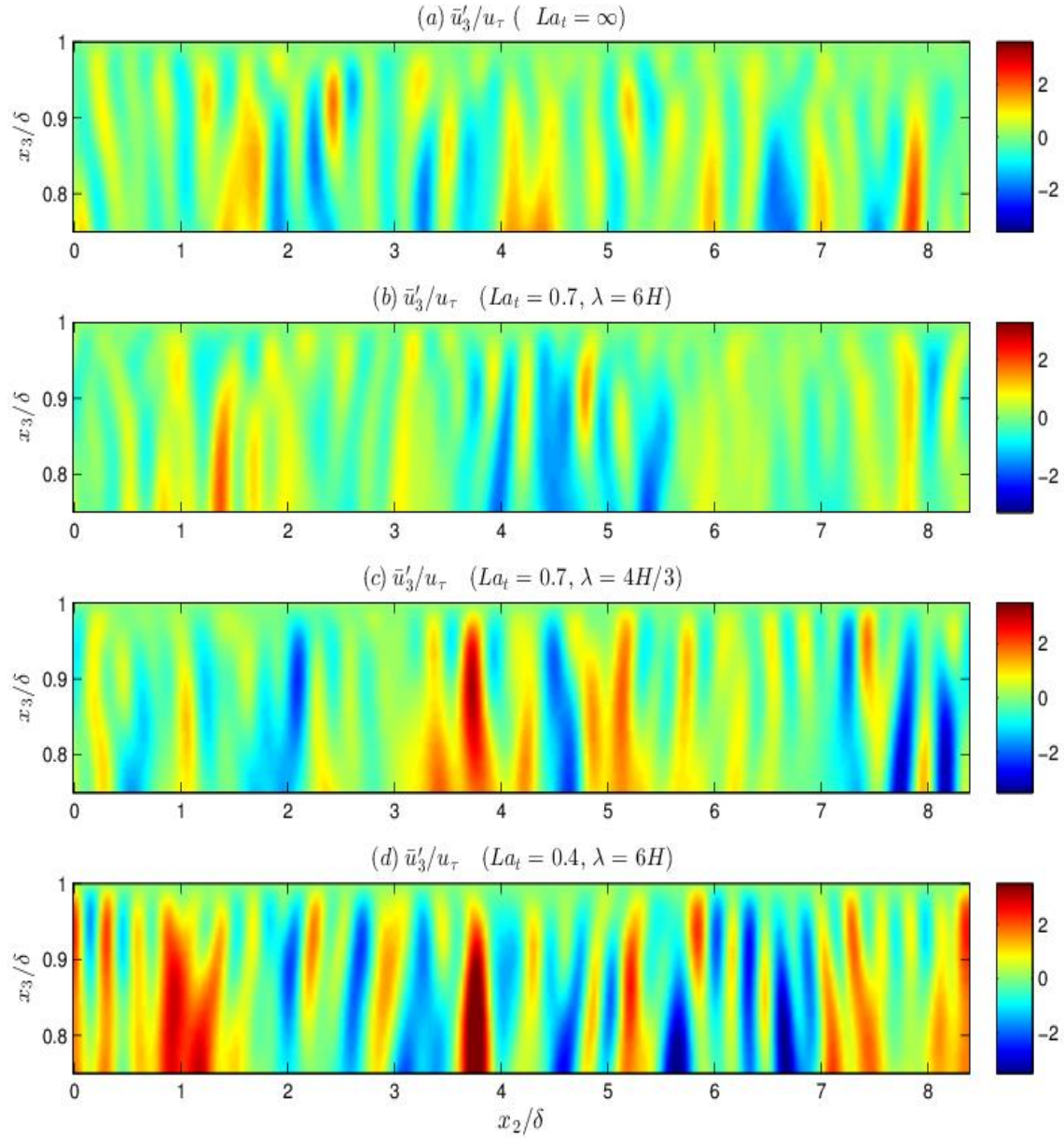


Figure 4.9 Instantaneous snapshots of vertical velocity fluctuations at $x_1 = L_1/2$, where L_1 is the downwind length of the computational domain. These panels show the near-surface region extending from $x_3/\delta = 0.75$ through $x_3/\delta = 1$ (i.e. the upper one-eighth of the water column) Recall that the bottom of the water column is located at $x_3/\delta = -1$ and the surface is at $x_3/\delta = 1$. These panels highlight the downwelling and upwelling limbs of small scale vortices near the surface.

Furthermore, Figure 4.8b shows that the full-depth LC in the $(La_t = 0.4, \lambda = 6H)$ case is stronger than in the $(La_t = 0.7, \lambda = 6H)$ case in the upper-half of the water column and vice-

versa. This is consistent with Figure 4.5a, d showing a more intense surface convergence of the LC in the $(La_t = 0.4, \lambda = 6H)$ case than in the $(La_t = 0.7, \lambda = 6H)$ case induced by the stronger upwelling limb of the former case (Figure 4.5b, e). The opposite occurs in the lower half of the water column where the bottom divergence of the LC in the $(La_t = 0.4, \lambda = 6H)$ case is less intense than in the $(La_t = 0.7, \lambda = 6H)$ case due to the weaker downwelling limb of the former.

Although there are differences between the cases with $(La_t = 0.7, \lambda = 6H)$ and $(La_t = 0.4, \lambda = 6H)$ in terms of $\langle \bar{u}'_3 \bar{u}'_3 \rangle_{LC}$, these differences are not as pronounced as the differences in terms of $\langle \bar{u}'_3 \bar{u}'_3 \rangle$ seen in Figure 4-8a. This suggests that a decrease in La_t from 0.7 to 0.4 with fixed λ gives rise to intensification of Langmuir turbulence scales of smaller size and less coherent than the full-depth LC. Intensification of these smaller Langmuir turbulence scales is due to the increase in Stokes drift shear throughout the entire water column induced by lowering La_t from 0.7 to 0.4 (with λ fixed at 6H; see Figure 3.2b).

4.3 Disruption of the Near-Surface Log-Law

Next, the impact of shallow water Langmuir turbulence within the near-surface log-layer is examined in terms of mean velocity and budgets of turbulent kinetic energy (TKE). In all flows with LC, the Langmuir turbulence and associated full-depth LC homogenize momentum throughout most of the water column, which leads to near constant mean downwind velocity profiles, as seen in Figure 4.10a. Figure 4.10b shows mean downwind velocity deficit in the upper half of the water column. Mean downwind velocity deficit is defined as

$(\langle \bar{u}_{surface} \rangle - \langle \bar{u}_1 \rangle) / u_\tau$, where $\bar{u}_{surface}$ is downwind velocity, \bar{u}_1 , evaluated at the surface. It is

well known that the mean downwind velocity deficit under a shear-driven air-water interface exhibits behavior similar to the law of the wall in wall-bounded boundary layers. This is the case for the flow without LC, for which the mean downwind velocity deficit is characterized by a well-developed log-law (Figure 4.10b).

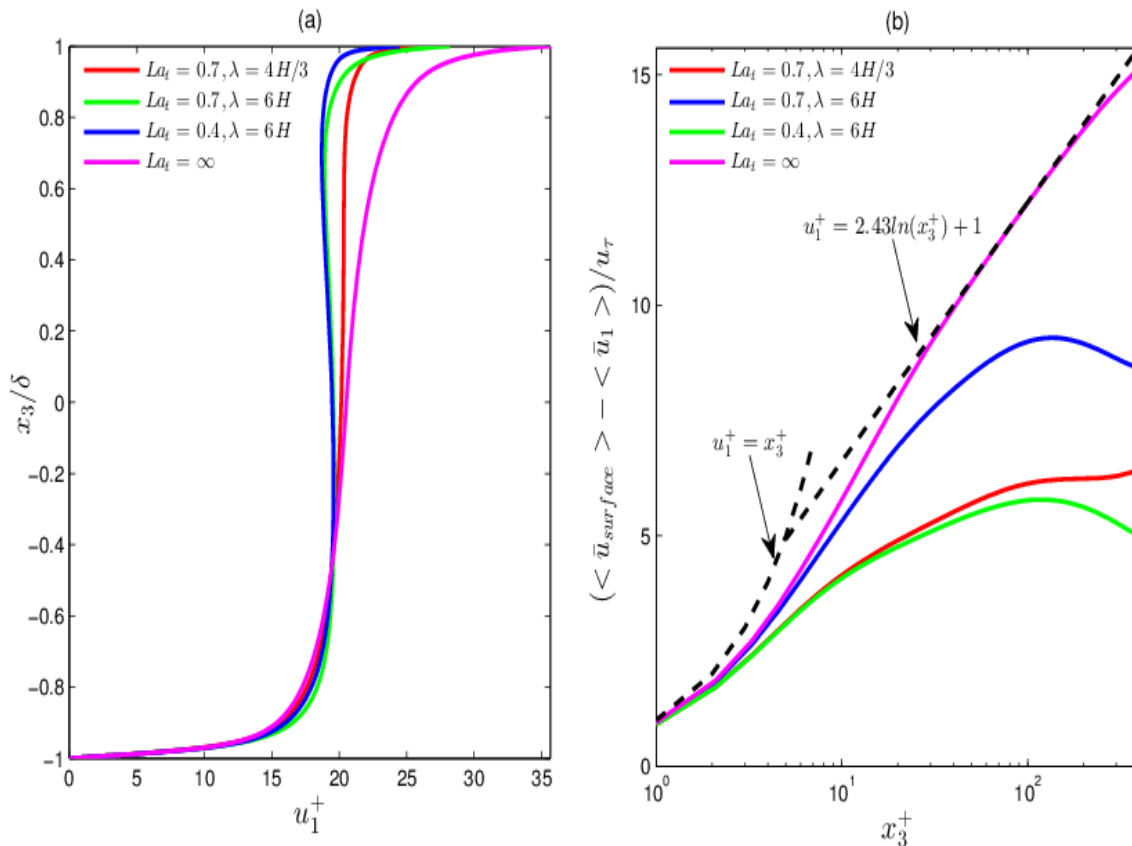


Figure 4.10 Mean downwind velocity (a) and mean downwind velocity deficit in the upper half of the water column (b) in flows with and without LC. x_3^+ measures the distance to the surface in plus units. Please see a zoomed-in version of mean downwind velocity in (a) within the upper half of the water column in Figure 4.16a.

As can be seen in Figure 4.10b, in flows with LC the log law profile of the velocity deficit is disrupted or eroded. This can be attributed to increased mixing induced by intensification of near-surface small scale eddies relative to the flow without LC (as seen earlier in Figure 4-9). As noted earlier, this intensification of near-surface small scale eddies is associated with near-

surface Stokes drift shear. For example, in Figure 4.10b, comparing the case with $La_t = 0.7$ and $\lambda = 6H$ to the case with $La_t = 0.7$ and $\lambda = 4H/3$, it is seen that a decrease in λ while holding La_t fixed leads to a more pronounced disruption of the log law. The smaller value of λ serves to increase Stokes drift shear near the surface (see Figure 3.2b) leading to higher levels of mixing near the surface caused by intensified small-scale eddies (see Figure 4.9b, c). A decrease in La_t can also lead to higher Stokes drift shear near the surface and thus greater disruption of the surface velocity log-law, as can be seen comparing the case with $La_t = 0.7$ and $\lambda = 6H$ to the case with $La_t = 0.4$ and $\lambda = 6H$ (see Figure 4.10b and 3.2b).

The impact of increasing Stokes drift shear on mean velocity can also be seen in Figure 4.16a, showing a zoomed-in version of Figure 4.10a in the upper-half of the water column. In Figure 4.16a it can be seen that the flows with LC with greatest near-surface Stokes drift shear (cases with $(La_t = 0.4, \lambda = 6H)$ and $(La_t = 0.7, \lambda = 4H/3)$, respectively) are characterized by thinner velocity boundary layers at the surface. For example, the boundary layer at the surface in the $(La_t = 0.7, \lambda = 4H/3)$ case is thinner than in the $(La_t = 0.7, \lambda = 6H)$ case due to the greater near-surface Stokes drift shear of the former despite its weaker full-depth LC described earlier. As will be discussed further below, the strength of full-depth LC plays a prominent role in determining the extent of negative mean velocity shear observed Fig. 4.16a in the upper-half of the water column in several of the flows with LC.

4.4 Budgets of Turbulent Kinetic Energy (TKE)

Figure 4.11 plots all TKE budget terms for flows with and without LC within the surface log-layer. TKE budgets were defined in Chapter 3 in Eqn. (3-12). In all flows with LC, production by Stokes drift velocity shear plays an important role. The magnitude of this production term

depends on λ , the wavelength of surface waves. Recall that the Stokes drift velocity decays with depth and, furthermore, the decay is faster for shorter wavelengths, which results in greater Stokes drift shear (see the Stokes drift velocity definition in Eqn. (3-4) and Figure 3.2.b). Thus, as expected, in flow with LC with $La_t = 0.7$ and $\lambda = 4H/3$, production by Stokes drift shear reaches higher values than in the flow with the same La_t but with longer wavelength $\lambda = 6H$ (see Fig. 4.11b, d). In the case of the flow with LC with $La_t = 0.4$ and $\lambda = 6H$ (Figure 4.11c), production by Stokes drift shear is greater than production by mean velocity shear throughout the entire x_3^+ range shown, partly due to the mixing of momentum (resulting in a diminishing of mean velocity shear) caused by strong small-scale near-surface eddies combined with the strong full-depth LC relative to the other flows studied.

The flow without LC (Figure 4.11a) is characterized by a well-developed log-layer for which the classical balance between production by mean shear and dissipation holds. In this case, dissipation of TKE is caused by viscous (molecular) stress and also by the LES SGS (subgrid-scale) stress defined in Chapter 3. Balances in flows with LC within the log-layer are drastically different from that in the flow without LC, as turbulent transport and pressure transport in flows with LC play non-negligible roles. Consequently, a strict balance between production and dissipation does not occur, as seen in the production-to-dissipation ratios plotted in Figure 4.11. For the flow without LC this ratio is nearly unity. However, for the flows with LC, the ratios deviate greatly from unity. The extent of this deviation depends on both La_t and λ as seen from Figure 4.11. A decrease in La_t while holding λ fixed can cause a larger deviation. Moreover, an increase in λ while holding La_t fixed can also cause larger deviation.

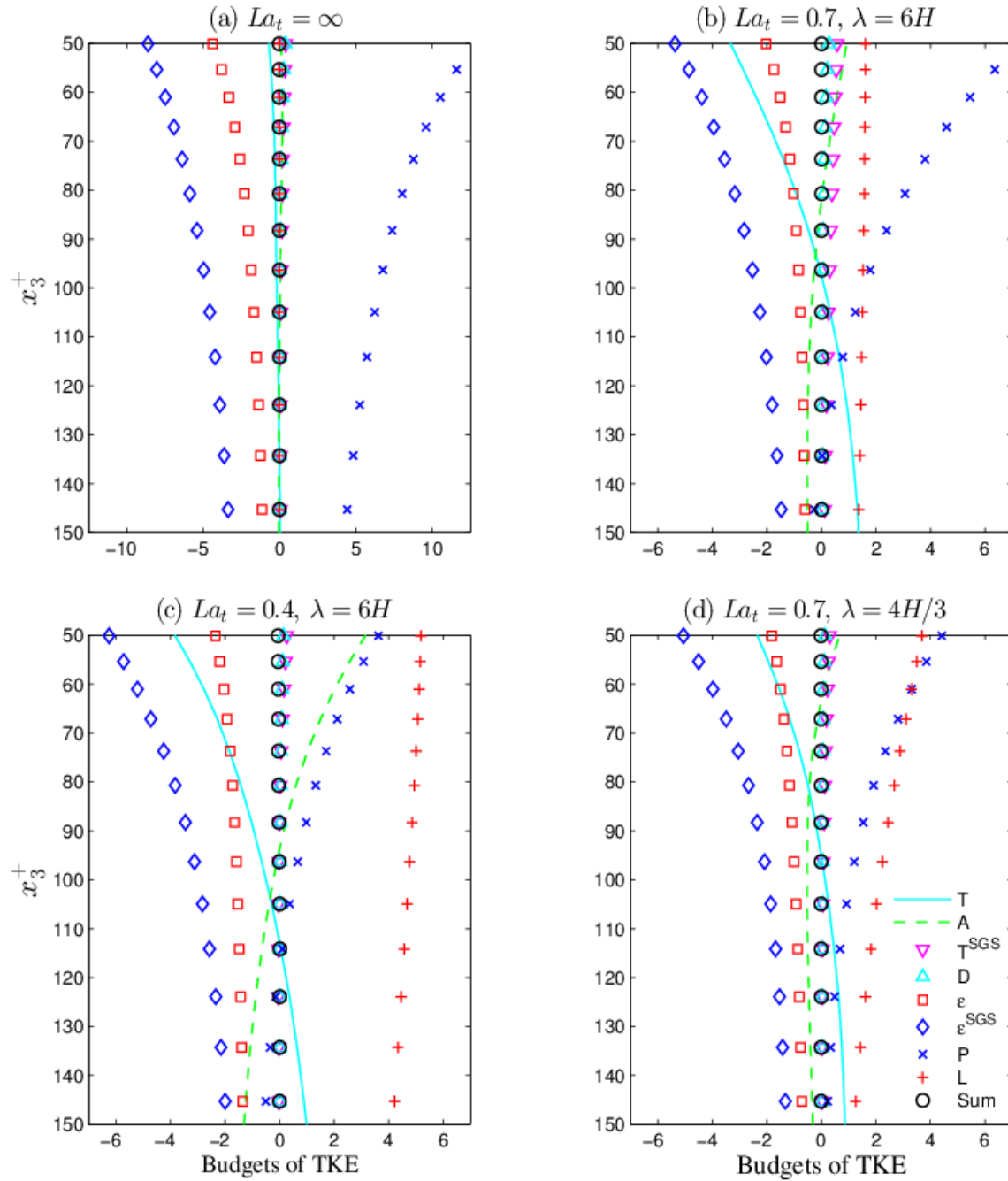


Figure 4.11 Budgets of TKE scaled by u_τ^2 in the surface log-layer. x_3^+ measures the distance to the surface in plus units. T is turbulent transport, A is pressure transport, T^{sgs} is SGS transport, D is viscous diffusion, ϵ is viscous dissipation, ϵ^{sgs} is SGS dissipation, P is mean velocity shear production, and L is production by Stokes drift velocity shear. Definitions of these terms are given in previous chapter. Note that under statistical equilibrium, budget terms sum to zero.

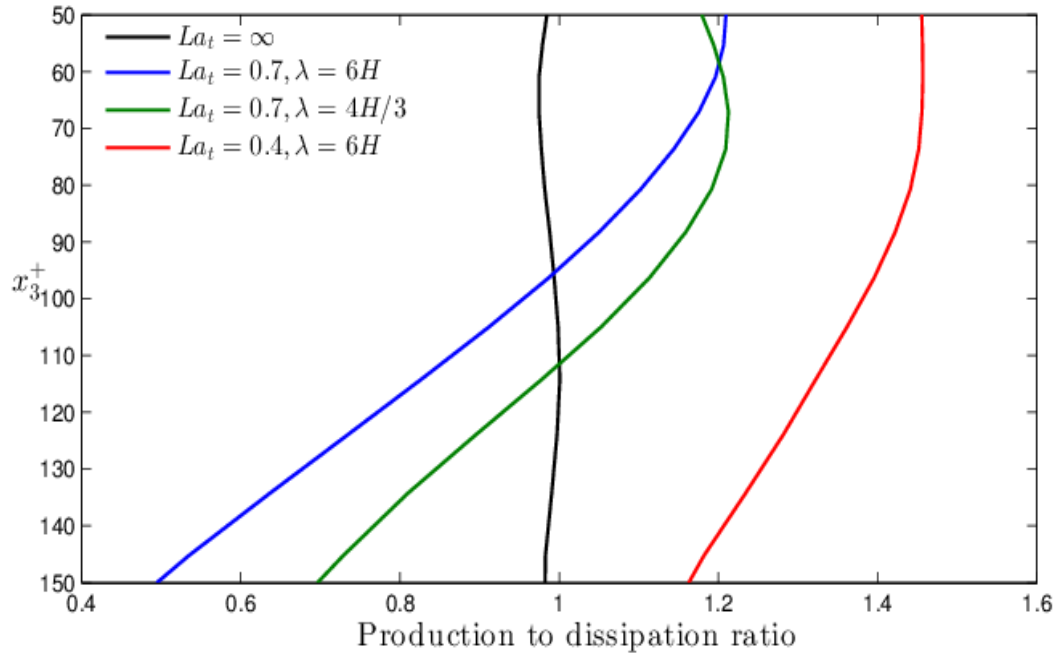


Figure 4.12 Production to dissipation ratio in the surface log-layer. x_3^+ measures distance to the surface in plus units. In flow without LC, production is by mean shear only. In flow with LC, production is by mean shear and Stokes drift shear. In all flows, net dissipation is viscous (molecular) dissipation plus SGS dissipation.

4.5 Budgets of TKE Components

Figure 4.13 plots budget terms for all TKE components for flows with and without LC within the surface log-layer, showing transfer of energy between the individual components of TKE. In the flow without LC, as is also the case in traditional boundary layers, mean shear acts as the main source of downwind TKE $\langle \bar{u}'_1 \bar{u}'_1 \rangle$ while pressure-strain correlation serves to re-distribute this energy to crosswind $\langle \bar{u}'_2 \bar{u}'_2 \rangle$ and vertical $\langle \bar{u}'_3 \bar{u}'_3 \rangle$ components (Figure 4.13, first row of panels). In the flows with LC, Stokes drift shear serves as a source of vertical TKE, while pressure-strain correlation re-distributes this energy to the crosswind component (Figure 4.13, second and third rows of panels). Noteworthy is the fact that pressure-strain re-distribution acts as a source of vertical TKE in the flow without LC, but its role is reversed in flows with LC acting as a sink.

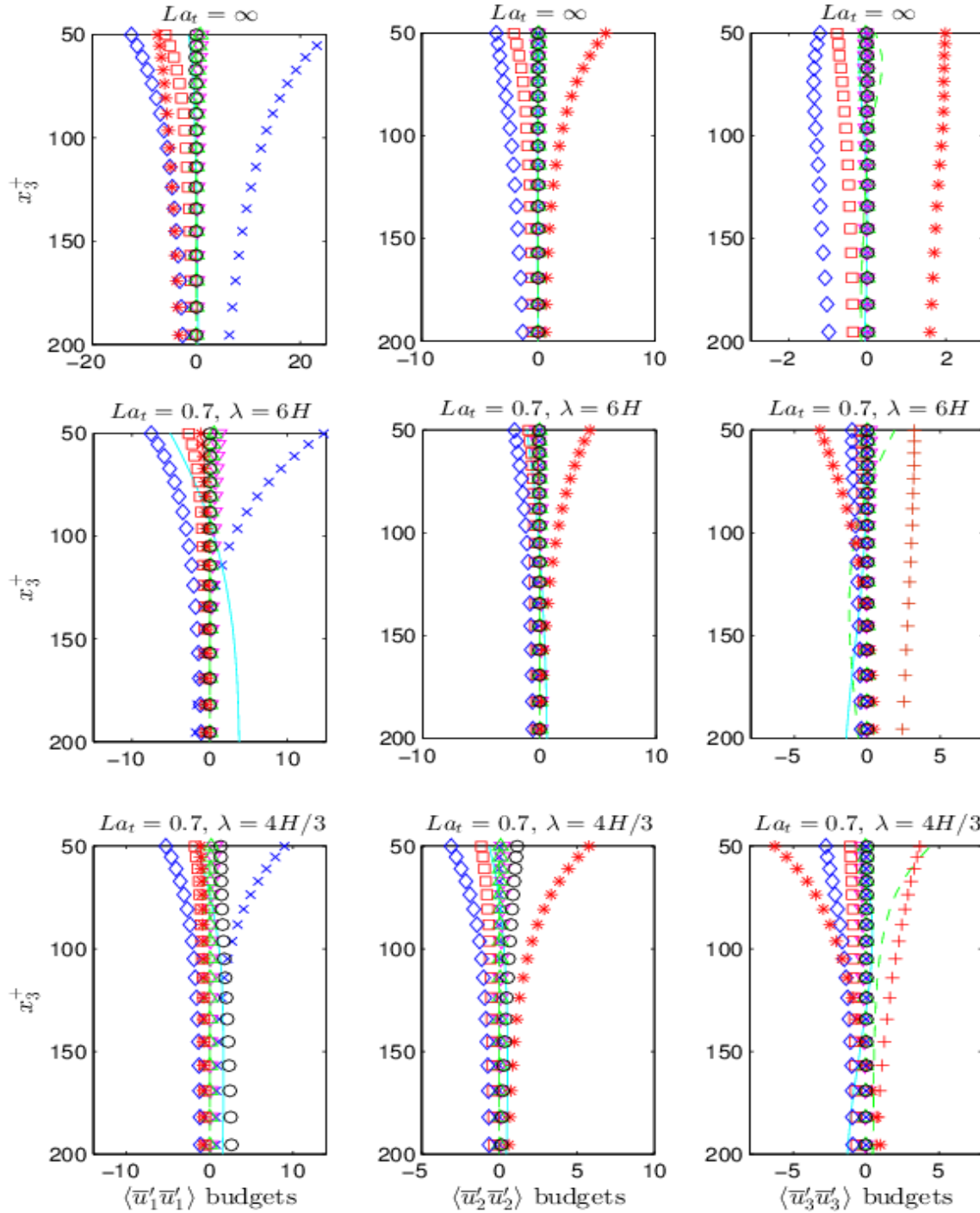


Figure 4.13 Near-surface balance of TKE component budget terms (scaled by u_t^2) in flows with and without LC. — is turbulent transport, — — is pressure transport, ∇ is SGS transport, Δ is viscous diffusion, \square is viscous dissipation, \diamond is SGS dissipation, $*$ is pressure strain redistribution, \times is mean velocity shear production, $+$ is production by Stokes drift velocity shear and o is the sum of all terms. x_3^+ measures distance to the surface in plus units.

4.6 Budgets of Reynolds Shear Stress

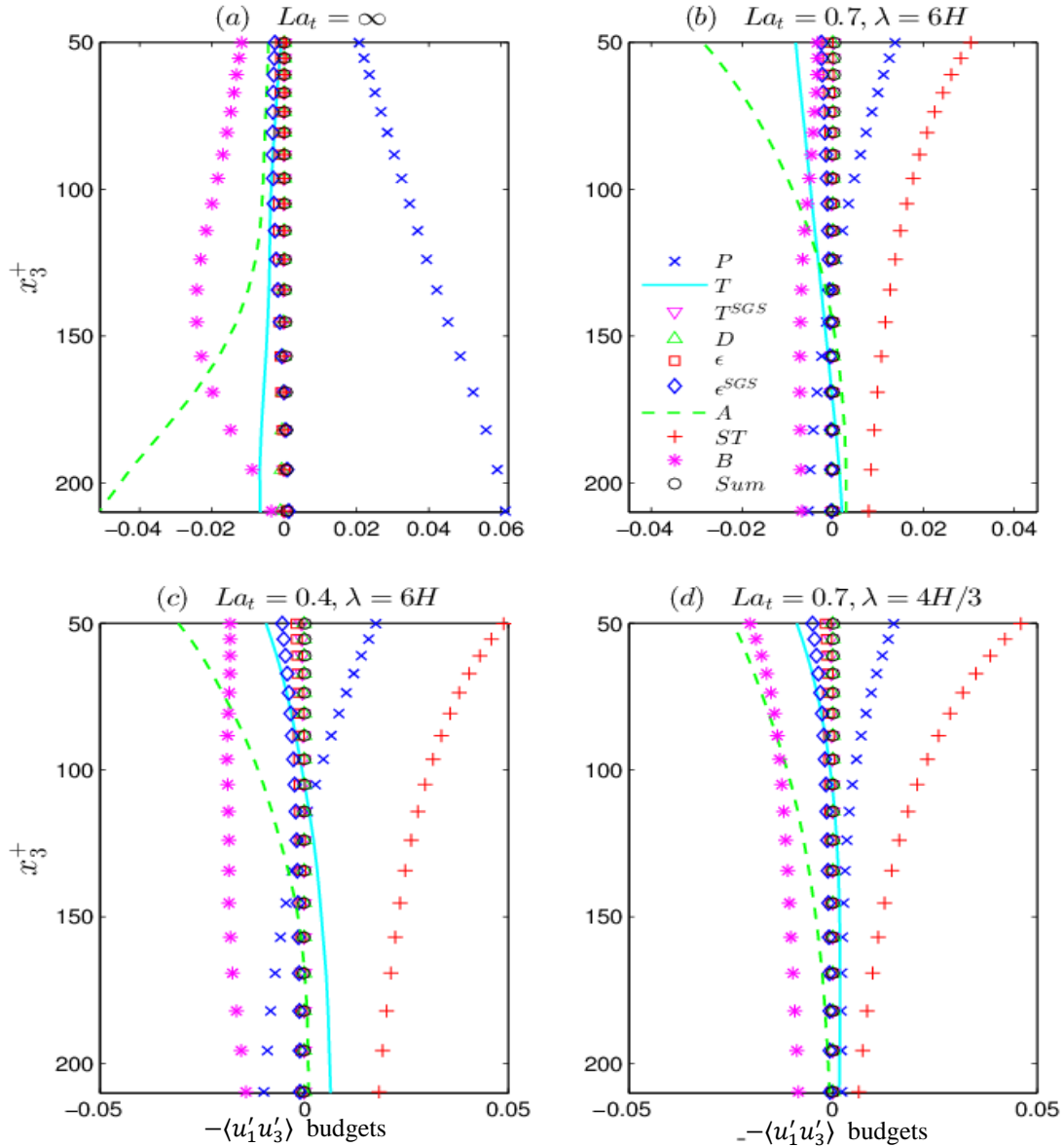


Figure 4.14 Near-surface budget terms of $-\langle \bar{u}'_1 \bar{u}'_3 \rangle$ (scaled by u_τ^2) in flows with and without LC. x_3^+ measures distance to the surface in plus units. P is production by mean velocity shear, T is turbulent transport, T^{SGS} is SGS transport, D is viscous diffusion, ϵ is viscous dissipation, ϵ^{SGS} is SGS dissipation, A is pressure transport, ST is production by Stokes drift shear and B is pressure-strain correlation.

Figure 4.14 shows near-surface budget terms for the Reynolds shear stress (downwind-vertical) component $-\langle \bar{u}'_1 \bar{u}'_3 \rangle$. These budget terms were defined earlier in Chapter 3, Eqn. (3-8).

Within the surface log layer, in the flow without LC (Fig. 4.14a), the only source is production

by mean velocity shear. In flows with LC (Fig. 4.14b, c, d) production by mean velocity shear is a secondary source to production by Stokes drift shear. In flows with LC, near the surface, production by mean velocity shear is significant, however, this production diminishes at depths $100 \leq x_3^+ \leq 150$ below the surface. In some of the LC cases [e.g. the cases with $(La_t=0.7, \lambda = 6H)$, $(La_t=0.4, \lambda = 6H)$, and $(La_t=1.0, \lambda = 6H)$] the mean shear source switches sign becoming a sink at depths below the $100 \leq x_3^+ \leq 150$ range. In Figure 4.14, for the case with $(La_t=0.4, \lambda = 6H)$, it can be seen that turbulent transport replaces production by mean shear as a secondary source to Stokes drift shear when mean shear becomes a sink. This trend of turbulent transport becoming more significant as a source compensating for mean velocity shear becoming a sink can be seen Figure 4.15.

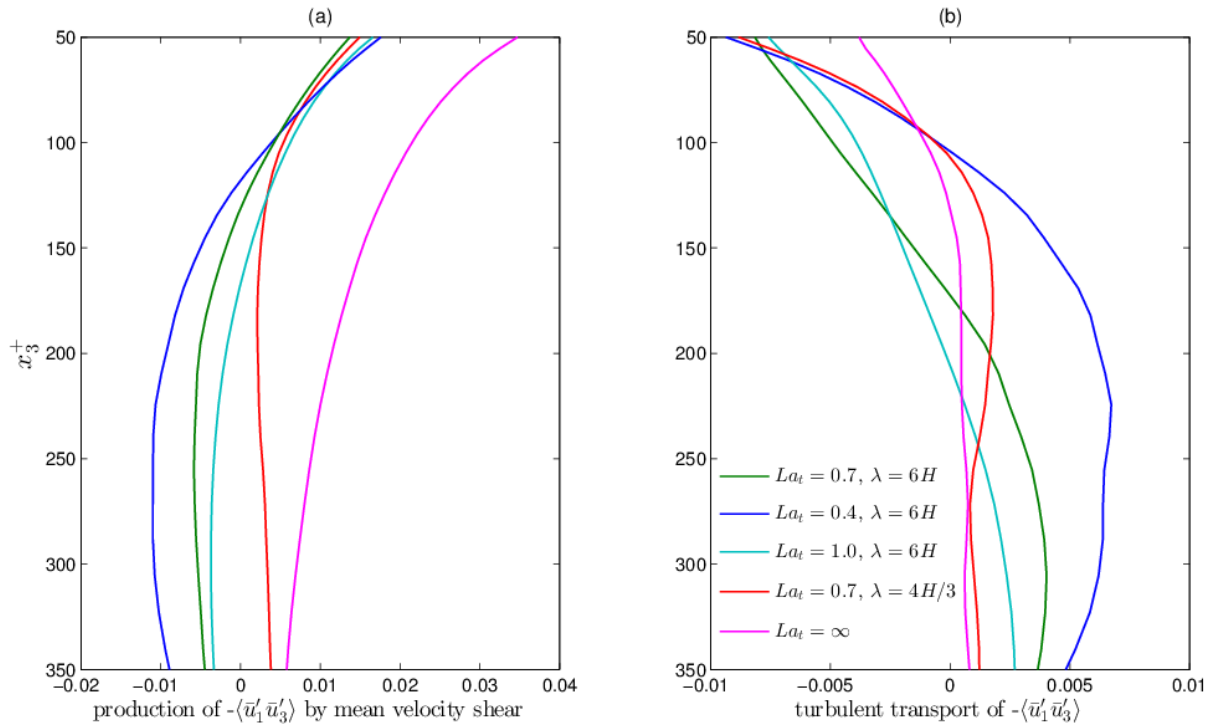


Figure 4.15 (a) Production by mean velocity shear and (b) turbulent transport budget terms of $-\langle \bar{u}'_1 \bar{u}'_3 \rangle$ (scaled by u_T^2) in flows with and without LC. x_3^+ measures distance to the surface in plus units.

Negative mean velocity shear (i.e. the vertical gradients of the mean velocities shown in Figure 4.16a) and its previously described relationship with turbulent transport are linked to strength of full-depth LC (discussed earlier in this chapter). For example, in Figure 4.16a, it can be seen that in flow with $(La_t = 1.0, \lambda = 6H)$ the extent of negative mean velocity shear is not as great as it is for the cases with stronger full-depth LC with $(La_t = 0.7, \lambda = 6H)$ and $(La_t = 0.4, \lambda = 6H)$. In the flow with $(La_t = 0.7, \lambda = 4H/3)$, the full-depth cells are weaker than in the other flows with LC and, correspondingly, in this case mean velocity shear is always positive (Fig. 4.16a, red curve). Given the previous relationship between strength of LC, negative mean velocity shear and turbulent transport, the latter may be linked directly to transport induced by the full-depth LC.

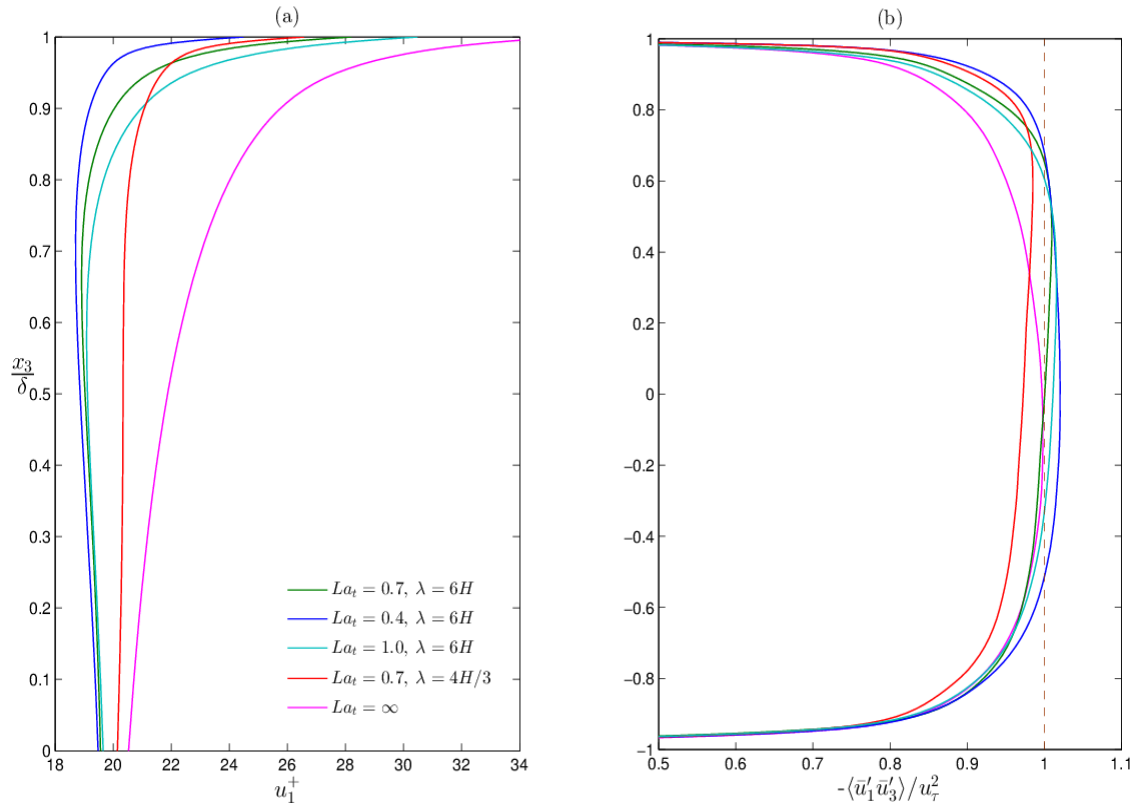


Figure 4.16 (a) Mean velocity in upper half of water column and (b) Reynolds shear stress, $-\langle \bar{u}'_1 \bar{u}'_3 \rangle$ in flows with and without LC. x_3^+ measures distance to the surface in plus units.

Figure 4.16b shows that the Reynolds shear stress is greater or equal to zero throughout the entire water column despite the negative mean velocity shear induced by Langmuir turbulence in some of the flows with LC (Figure 4.16a). This suggests a breakdown of the Boussinesq approximation in traditional RANS turbulence models, which for the wind-driven shear flows being considered here model the Reynolds shear stress $-\langle \bar{u}'_1 \bar{u}'_3 \rangle$ as

$$\tau_{13}^{RNS} = 2\nu_t^{RNS} \frac{d\langle u_1 \rangle}{dx_3} \quad (4-2)$$

The previous analysis of Reynolds shear stress budgets in Figures 4.14 ad 4.145 suggest that for Langmuir turbulence, the Reynolds shear stress model in Eqn. (4-2) should also include a term proportional to Stokes drift shear due to its leading contribution to the production of $-\langle \bar{u}'_1 \bar{u}'_3 \rangle$. Furthermore, such a model should also contain a nonlocal term (i.e. a term not proportional to local velocity gradients) based on the significant contribution by turbulent transport as a source to the Reynolds shear stress budgets in cases when mean velocity shear becomes negative.

In more physical terms, the Reynolds shear stress represents a turbulent vertical momentum flux (i.e. vertical flux of downwind velocity fluctuations by vertical velocity fluctuations). The fact that this flux remains positive while mean velocity shear becomes negative suggests the presence of a counter-gradient flux. In the flows studied here, the full-depth Langmuir cells provide this counter-gradient or non-local flux. This flux is not related to mean velocity local shear, but rather to the global (full-depth) upwelling and downwelling limbs of the cells. The downwelling limbs serve to transport positive downwind velocity fluctuations from the surface down to the bottom of the water column and the upwelling limbs serve to do the opposite, both contributing towards a positive Reynolds shear stress (i.e. towards a positive $-\langle \bar{u}'_1 \bar{u}'_3 \rangle$). This can

be seen from Figures (4-4) through (4-6) showing the full-depth downwelling limbs of the cells (characterized by negative velocity fluctuations) generally coinciding with full-depth regions of positive downwind velocity fluctuations and vice-versa.

Although full-depth LC can induce negative mean velocity shear throughout the core region of the water column, near the surface (approximately in the uppermost one-eighth of the water column), mean velocity shear is positive for all cases with LC, and thus the Boussinesq approximation holds. As noted earlier, in this region, in cases with LC, Stokes drift shear serves to enhance near-surface small scale eddies (see Figure 4.9) ultimately leading to greater near-surface mixing. This is reflected through the rms of vertical velocity in Figure 4.8a explained earlier. This is also reflected through the Reynolds shear stress profiles shown in Figure 4.16b. For example, in the upper one-eighth portion of the water column, the Reynolds shear stresses in flows with ($La_t = 0.4$, $\lambda = 6H$) and ($La_t = 0.7$, $\lambda = 4H/3$), respectively, are greater than in the other flows with LC. This behavior is similar to the behavior of rms of vertical velocity seen earlier in Figure 4.8a and suggests an amplified RANS eddy viscosity near the surface.

The need for an enhanced near-surface eddy viscosity can be confirmed a posteriori based on LES fields. The eddy viscosity is computed by dividing the LES-resolved Reynolds shear stress by the LES mean velocity shear:

$$\nu_t^{RNS} = \langle \bar{u}'_1 \bar{u}'_3 \rangle \frac{d\langle \bar{u}_1 \rangle}{dx_3} \quad (4-3)$$

The predicted eddy viscosities for all flows studied are shown in Figure 4.17. As expected, the highest near-surface eddy viscosities correspond to the flows with the highest near-surface Stokes drift shear, i.e. the flows with ($La_t = 0.4$, $\lambda = 6H$) and ($La_t = 0.7$, $\lambda = 4H/3$), respectively.

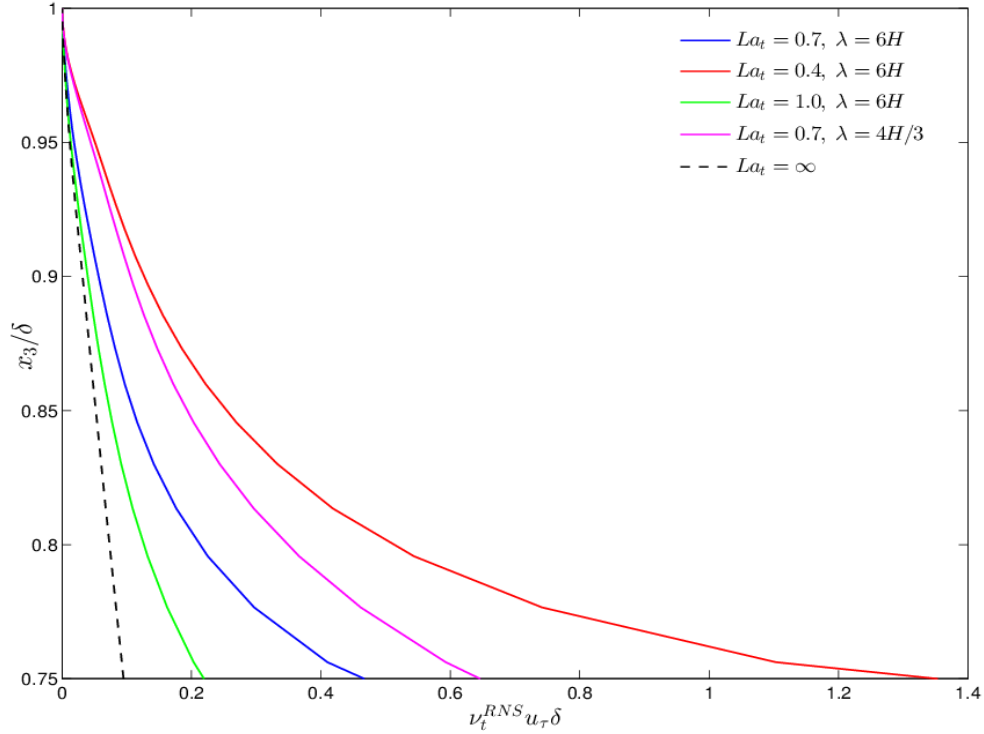


Figure 4.17 A posteriori evaluation of the RANS eddy viscosity based on LES fields.

4.7 Summary and Conclusions

Results from LES of wind-driven shallow water flow with Langmuir turbulence with full-depth LC have been analyzed in terms of turbulence structure, mean velocity, TKE budgets and Reynolds shear stress budgets with an emphasis on the near-surface region of the water column.

Full-depth LC was shown to manifest itself as a secondary component to the mean flow. Furthermore, full-depth LC corresponds to the largest scale of the Langmuir turbulence in homogeneous shallow water flows. LC is generated by the interaction between surface gravity waves and the wind-driven shear current (parameterized by the Craik-Leibovich vortex force in the governing momentum equation).

Langmuir turbulence led to the disruption of surface log-layer dynamics in terms of the mean downwind velocity and the production and dissipation rates of TKE. This disruption consisted of deviations from (i) the classical log-law velocity profile and (ii) the classical balance between production and dissipation rates of TKE, both exhibited by wind-driven flows without LC in the near-surface region of the water column.

Visualizations of LES velocity fluctuations revealed that the signature of full-depth LC can extend into the surface and bottom viscous sublayers altering the structure of the well-known low- and high-speed, small-scale streaks occurring within the viscous sublayers of wind-driven flow without LC.

The present LES study revealed that both, the turbulent Langmuir number (La_t , inversely proportional to wave forcing relative to wind forcing) and the wavelength (λ) of surface waves generating LC, play important roles in determining the Langmuir turbulence structure and overall dynamics. For example, a decrease in La_t from 1.0 to 0.7 while holding λ fixed lead to stronger full-depth LC characterized by higher magnitudes of crosswind and vertical velocity fluctuations throughout the water column. A decrease in La_t from 0.7 to 0.4 while holding λ fixed lead to a re-structuring of the full-depth LC, characterized by stronger vertical velocity fluctuations within the upwelling limb of the cells and stronger crosswind velocity fluctuation at the surface but weaker at the bottom. Analysis of rms of vertical velocity fluctuation and its contribution from full-depth LC revealed that the decrease in La_t from 0.7 to 0.4 while holding λ fixed led to a more significant enhancement of Langmuir turbulence scales smaller than the scale of full-depth LC compared to enhancement of the full-depth LC itself. Furthermore, a decrease in λ while holding La_t fixed, led to weaker full-depth LC, yet stronger near-surface small scale

eddies. The latter was due to the higher near-surface Stokes drift shear caused by the decrease in λ . Ultimately, it was seen that intensification of near-surface small scale eddies leads to greater disruption of the classical surface log-law velocity profile.

Analysis of mean velocity profiles and budget terms of Reynolds shear stress led to the conclusion that sufficiently strong full-depth LC may lead to negative mean velocity shear and thus the breakdown of the Boussinesq assumptions in RANS turbulence closures (models) for the Reynolds shear stress. Furthermore, from the budgets of Reynolds shear stress it was seen that Stokes drift production is the primary source. In cases where mean velocity shear is negative, turbulent transport assumes the role of secondary source. Given the previous relationship between strength of LC, negative mean velocity shear and turbulent transport, the latter may be linked directly to non-local transport induced by the full-depth LC.

Overall, results indicate that a Reynolds shear stress (RANS turbulence) model able to represent shallow water Langmuir turbulence should include the following:

- i. an enhanced eddy viscosity near the surface to account for intensification of near surface small scale mixing induced by Stokes drift shear,
- ii. a counter-gradient or non-local flux accounting for the mixing induced by full-depth LC, and
- iii. a flux down the gradient of Stokes drift velocity.

Chapter 6 presents a KPP model possessing the three previously listed components.

5 Bottom Boundary Layer Dynamics in LES of Langmuir Turbulence with Full-Depth LC

5.1 Introduction

Field measurements of Gargett et al. (2004), Gargett and Wells (2007) and (Gargett and Savidge, 2008) have shown that full-depth LC is an important mechanism for sediment resuspension and ultimately suggest strong interaction between the LC and the bottom boundary layer. This chapter presents analysis of LES results in order to understand the impact of full-depth LC on bottom boundary layer dynamics. Focus is on the impact of full-depth LC on the bottom boundary log-layer and its dependence on wind and wave forcing parameters La_t and λ .

5.2 Turbulence Structures

Figure 5.1 shows instantaneous upwelling and downwelling limbs of full-depth LC in terms of instantaneous vertical velocity averaged over the downwind direction for flows with different values of La_t and λ . Recall that downwelling limbs are generated at the surface convergence of LC, described earlier in the caption of Figure 2.1. As noted in the previous chapter, the coherency of the downwelling limbs of LC in Figure 5-1 in terms of downwind-averaged velocity fluctuation demonstrates that LC is a secondary, coherent turbulent structure advected by the mean flow and corresponds to the largest scales of the Langmuir turbulence generated

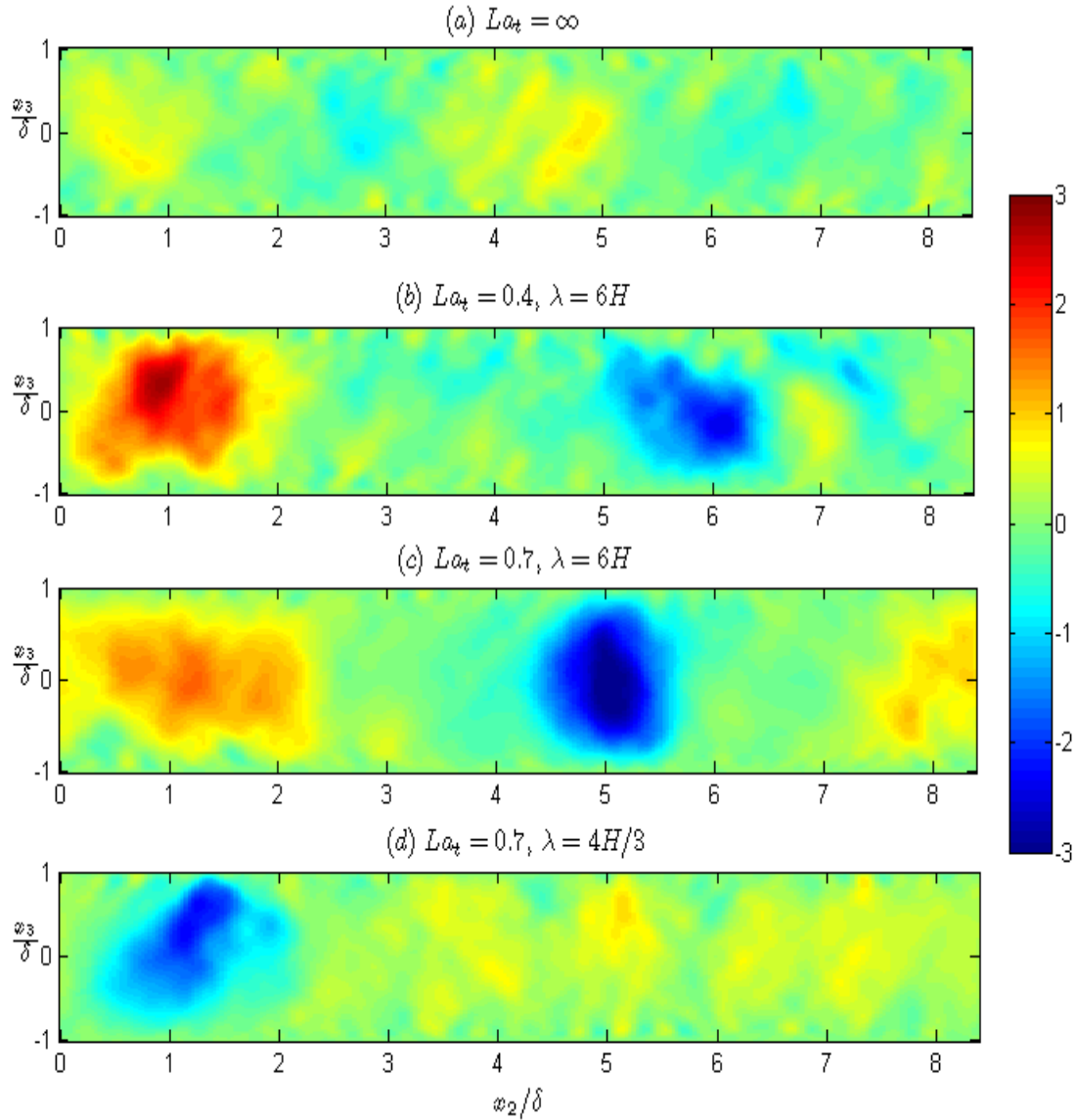


Figure 5.1 Instantaneous vertical velocity fluctuation (\bar{u}'_3/u_τ) averaged over the downwind x_1 direction showing upwelling and downwelling limbs of Couette cells in (a) and LC in (b) (c). The horizontal axis denotes the crosswind direction.

by the Craik-Leibovich vortex force in the governing momentum equations. Comparing panels (c) and (d) in Figure 5.1, it can be seen that lowering λ from $6H$ to $4H/3$ with La_t fixed at 0.7 leads to less coherent (weaker) upwelling and downwelling limbs. Meanwhile lowering La_t from 0.7 to 0.4 with λ fixed at $6H$ leads to a strengthening of the upwelling limb of the cell.

As will be shown in the upcoming sections, these characteristics play an important role in the bottom log-layer behavior induced by full-depth LC.

As also described in the previous chapter, the flow without LC ($La_t = \infty$) is characterized by Couette cells, which have been observed in DNS and LES of classical Couette flow driven by two parallel no-slip plates moving in opposite direction (e.g. (Papavassiliou and Hanratty, 1997)). Downwelling and upwelling limbs of Couette cells are evident in the first panel of Figure 5.1.

5.3 Mean Velocities

Figure 5.2a, b show mean velocity in plus units for flows with and without LC. The full horizontal axis in these figures extends from $x_3^+ \approx 0$ (denoting the bottom wall) up to $x_3^+ \approx 790$ (denoting the surface). In order to facilitate discussion of results, we have zoomed into the bottom log-layer region showing only the part extending from $x_3^+ \approx 40$ up to $x_3^+ \approx 395$ (the middle of the water column). In the region below the bottom log-layer not shown ($0 < x_3^+ < 40$) the velocity profiles for all cases are identical, while satisfying the expected $u_1^+ = x_3^+$ theoretical profile within the viscous sublayer $x_3^+ < 7$.

The homogenizing action of LC induces a near constant mean downwind velocity profile over the bulk region of the flow (see Figure 5.2c, d). Furthermore this homogenizing action extends deeper into the water column as the wavelength of the surface waves generating LC becomes larger (i.e. as λ becomes larger) (Figure 5.2c). This is expected based on the strength of full-depth LC, as described in the previous section (see for example Figure 4.6) and the form of the Stokes drift velocity shear in Figure 3.2b which has a depth-decay rate inversely proportional to λ .

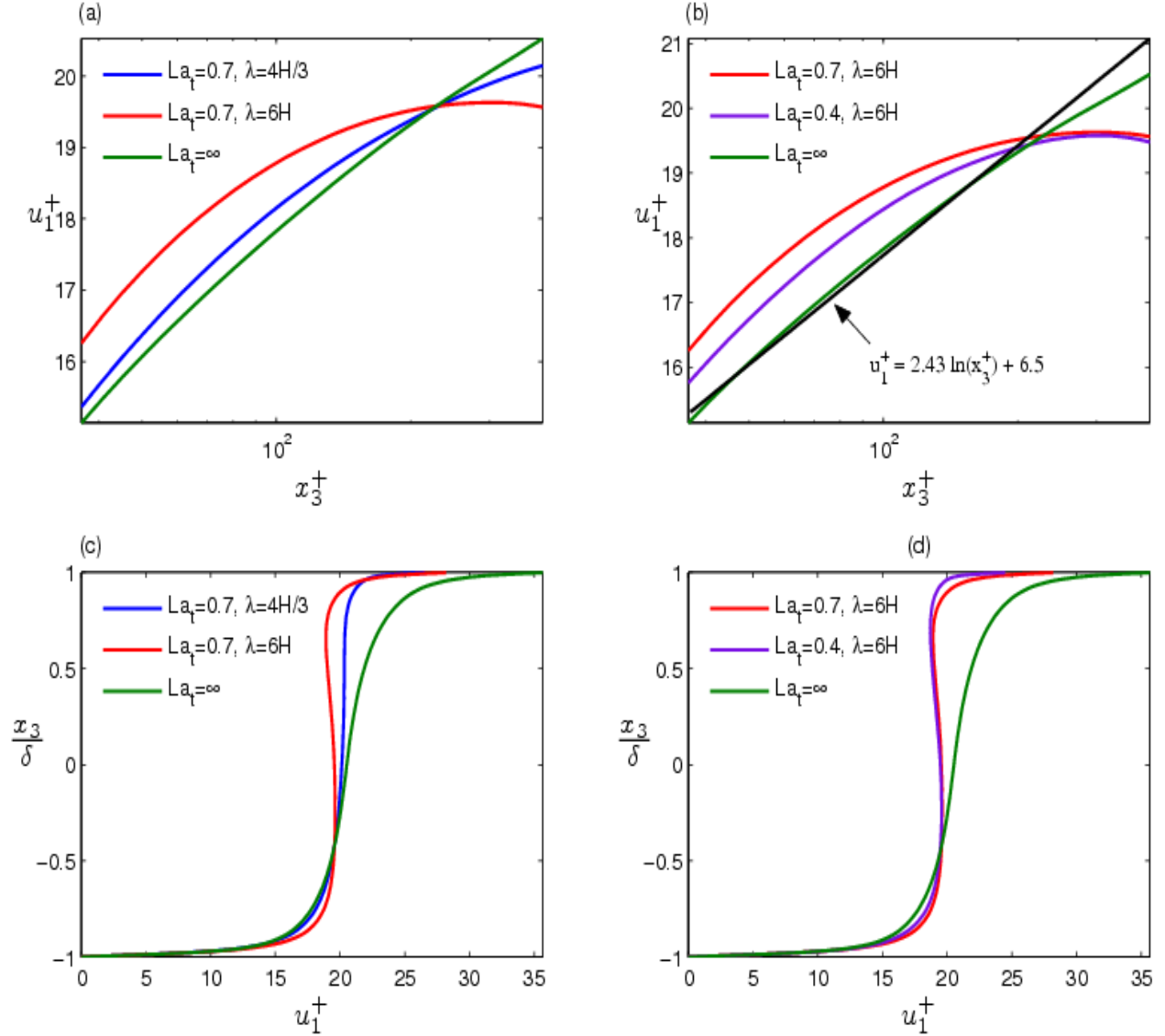


Figure 5.2 Mean velocity profiles: panels (a) and (c) show the variation with λ at fixed La_t with $\lambda = 6H$, $La_t = 0.7$ the reference and panels (b) and (d) show the variation with La_t at fixed λ . Note that $u_1^+ = \langle \bar{u}_1 \rangle / u_{\tau_b}$ where u_{τ_b} is the mean bottom (bed) stress friction velocity. For all flows considered here, the mean bottom stress is equal to the constant wind stress, thus the mean bed stress friction velocity is equal to wind stress friction velocity ($u_{\tau_b} = u_\tau$).

As seen in Figure 5.2a and b, the flow without LC ($La_t = \infty$) is characterized by a well-developed mean velocity log-law in the bottom half of the water column. In the flow without LC, the log-law extends from $x_3^+ \approx 50$ up to $x_3^+ \approx 200$. In the flow with LC generated by deepwater waves with $\lambda = 4H/3$ (Figure 5.2a, c) the mean velocity profile possesses a slight deviation from

the log-law. In the case of flows with LC generated by longer (intermediate) waves, the effect of LC extends deeper into the water column, causing a larger deviation or erosion of the classical log-law down to $x_3^+ \approx 90$ and inducing a velocity profile closer to the law of the wake (Figure 5.2a). This erosion is primarily caused by the downwelling limbs of the cells which bring high, well-mixed momentum closer to the bottom resulting in a shift from a well-developed log-law to a near constant profile for $x_3^+ > 100$, as seen in Figure 5.3b, c.

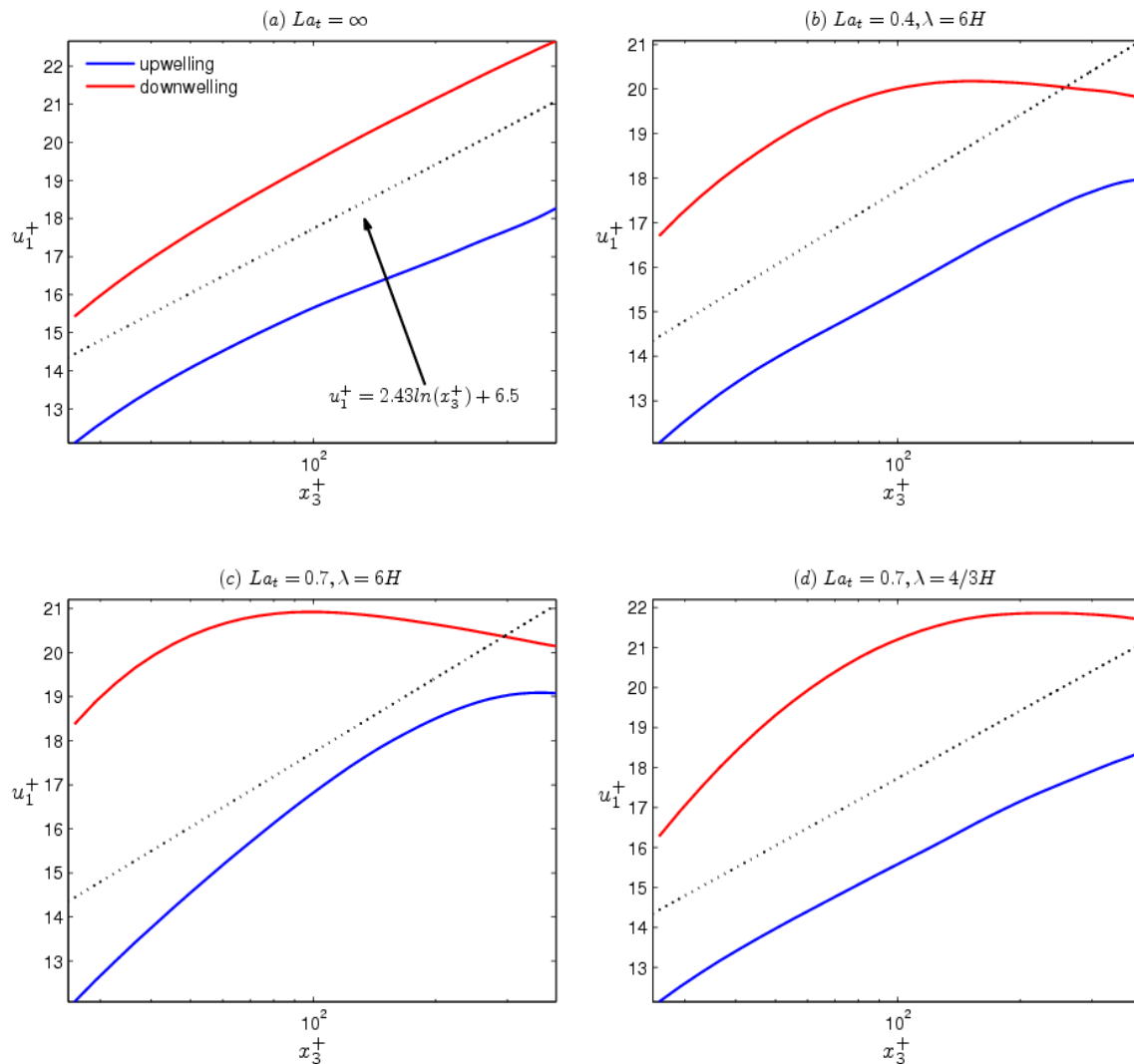


Figure 5.3 Mean velocity profiles within downwelling and upwelling limbs of Couette cells (a) and LC (b)-(d)

In flow with $La_t = 0.7$ and $\lambda = 4H/3$, the downwelling limb of LC tends to cause a deviation from the log-law (Figure 5.3d), however the resulting deviation is not as strong as in the $La_t = 0.7$ and $\lambda = 4H/3$ case (Figs. 5.2a, 5.3b, c). This is consistent with the downwelling limb of the LC being weaker in the $\lambda = 4H/3$ case compared with the $\lambda = 6H$ case as described in the previous chapter through Figure 4.6 and also in Figures 5.1c, d.

In Figure 5.2b, it can be seen that in the cases with $\lambda = 6H$, the case with $La_t = 0.7$ is characterized by a more pronounced deviation from the log-law compared to the case with $La_t = 0.4$. The reason for this can be traced to the stronger upwelling limb of the $La_t = 0.4$ case, observed by comparing Figures 5.1b and 5.1c. This stronger upwelling limb brings slower moving fluid to the log-region (Fig. 5.3b, c) serving to dampen the log-layer disrupting effect of the downwelling limb when averaging velocity over the crosswind direction (spanning both upwelling and downwelling limbs).

5.4 Budgets of Turbulent Kinetic Energy (TKE)

Balances of TKE budget terms below mid-depth within the region $50 < x_3^+ < 200$ are shown in Figure 5.4. We focus on cases with $(La_t = 0.7, \lambda = 6H)$ and $(La_t = 0.7, \lambda = 4H/3)$ given that differences between these two cases are more pronounced than differences between cases with $(La_t = 0.7, \lambda = 6H)$ and $(La_t = 0.4, \lambda = 6H)$. We also show results from the flow without LC.

The flow without LC exhibits a well-developed bottom log-layer in which mean shear production of TKE is nearly balanced by viscous and SGS dissipation. In flow with LC generated by surface gravity waves with wavelength $\lambda = 6H$, LC disrupts the log-layer balance between production and dissipation within $50 < x_3^+ < 200$ (Figure 5.5 and 5.5). In this case

turbulent transport and pressure transport have greater influence on the dynamics than in the flow without LC. For example, turbulent transport becomes of the same magnitude as subgrid-scale (SGS) dissipation. In the case of flow with $\lambda = 4H/3$, the disruption of the balances of TKE is not as evident (turbulent transport is not as important) consistent with the diminished strength of LC in the lower half of the water column. Nevertheless a slight disruption still occurs as seen in the ratio between production and dissipation in Figure 5.5.

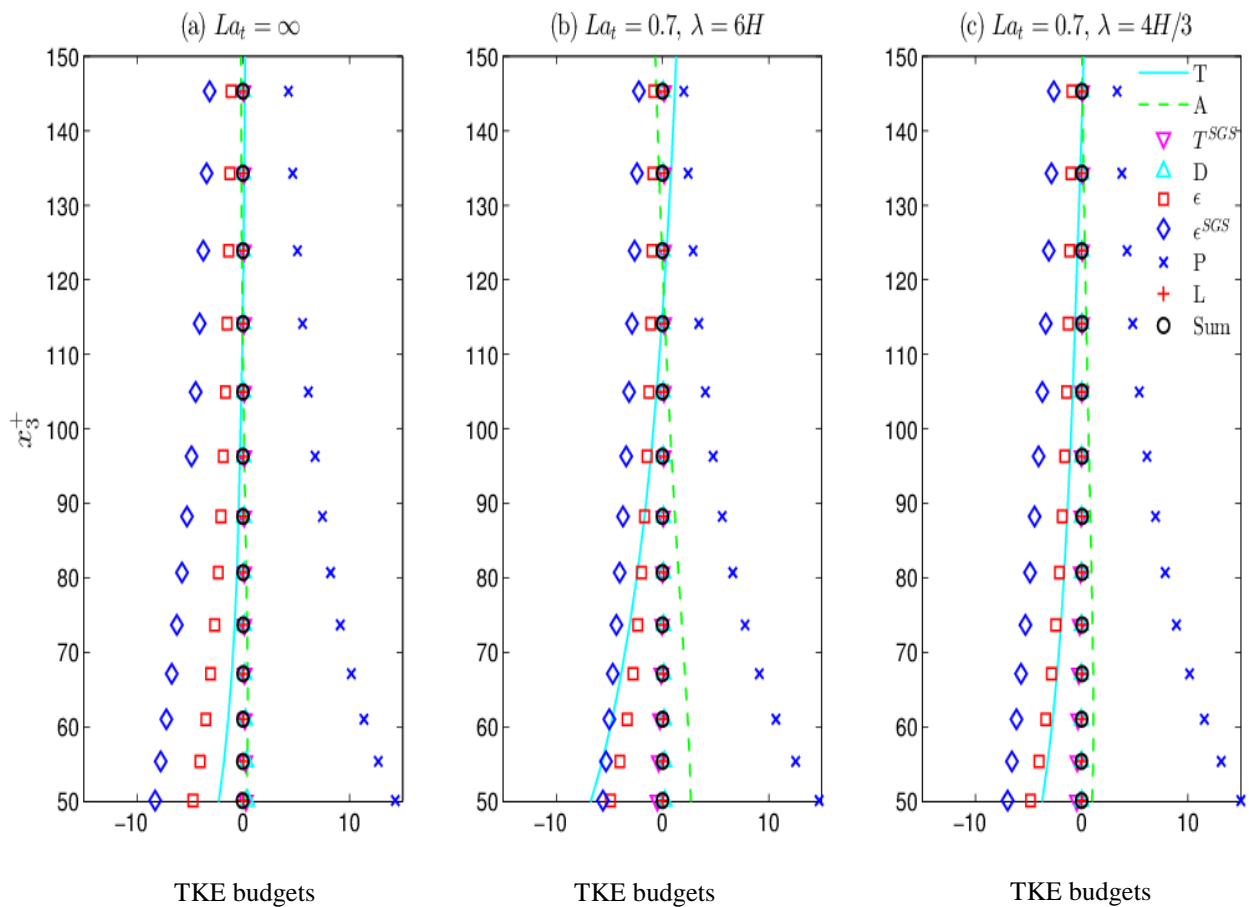


Figure 5.4 Near-bottom balance of TKE budget terms (scaled by u_τ^2) in flows with and flow without LC. T is turbulent transport, A is pressure transport, T^{SGS} is SGS transport, D is viscous diffusion, ϵ is viscous dissipation, ϵ^{SGS} is SGS dissipation, P is mean velocity shear production, and L is production by Stokes drift velocity shear. Definitions of these terms were given in Chapter 3.

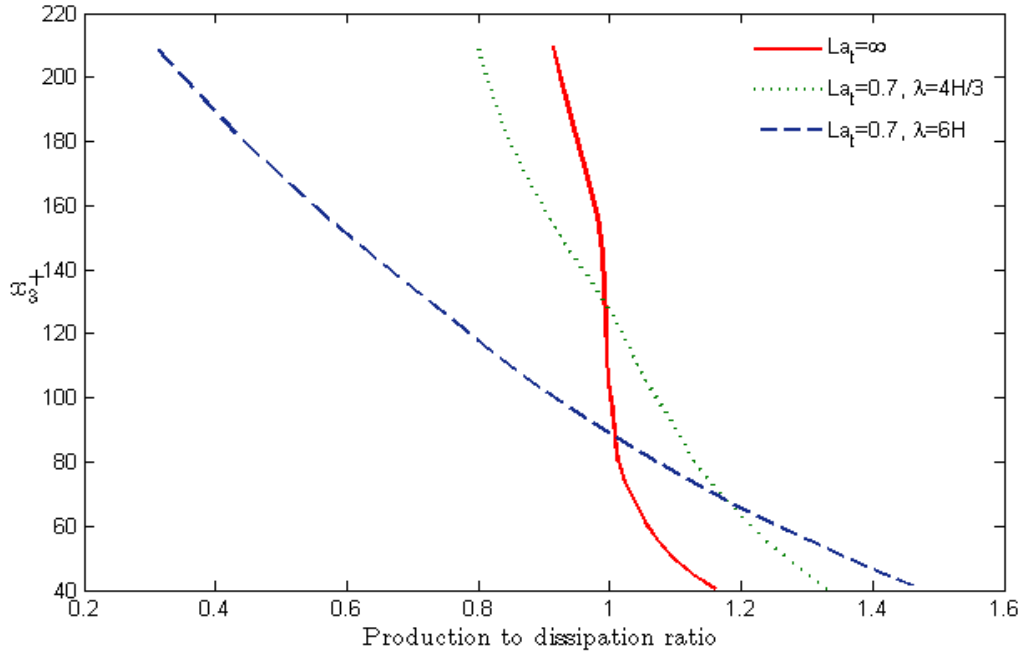


Figure 5.5 Ratio of production to dissipation of TKE

5.5 Budgets of TKE Components

Next we analyze transfer of energy between the individual components of TKE. In the flow without LC, as is also the case in traditional boundary layers, mean velocity shear acts as the main source of downwind TKE $\langle \bar{u}'_1 \bar{u}'_1 \rangle$ while pressure-strain correlation serves to re-distribute this energy to crosswind $\langle \bar{u}'_2 \bar{u}'_2 \rangle$ and vertical $\langle \bar{u}'_3 \bar{u}'_3 \rangle$ components (see Figure 5.6 first row of panels). In contrast, in flows with LC, pressure transport and turbulent transport act as the main sources of vertical TKE $\langle \bar{u}'_3 \bar{u}'_3 \rangle$ while pressure-strain correlation transfers this energy to the crosswind TKE component $\langle \bar{u}'_2 \bar{u}'_2 \rangle$ (Figure 5.6, first and second rows of panels). Noteworthy is the fact that pressure-strain correlation acts as a source of vertical TKE in the flow without LC, but its role is reversed in flows with LC acting as a sink. The same behavior was observed earlier in Chapter 4 for the surface log layer.

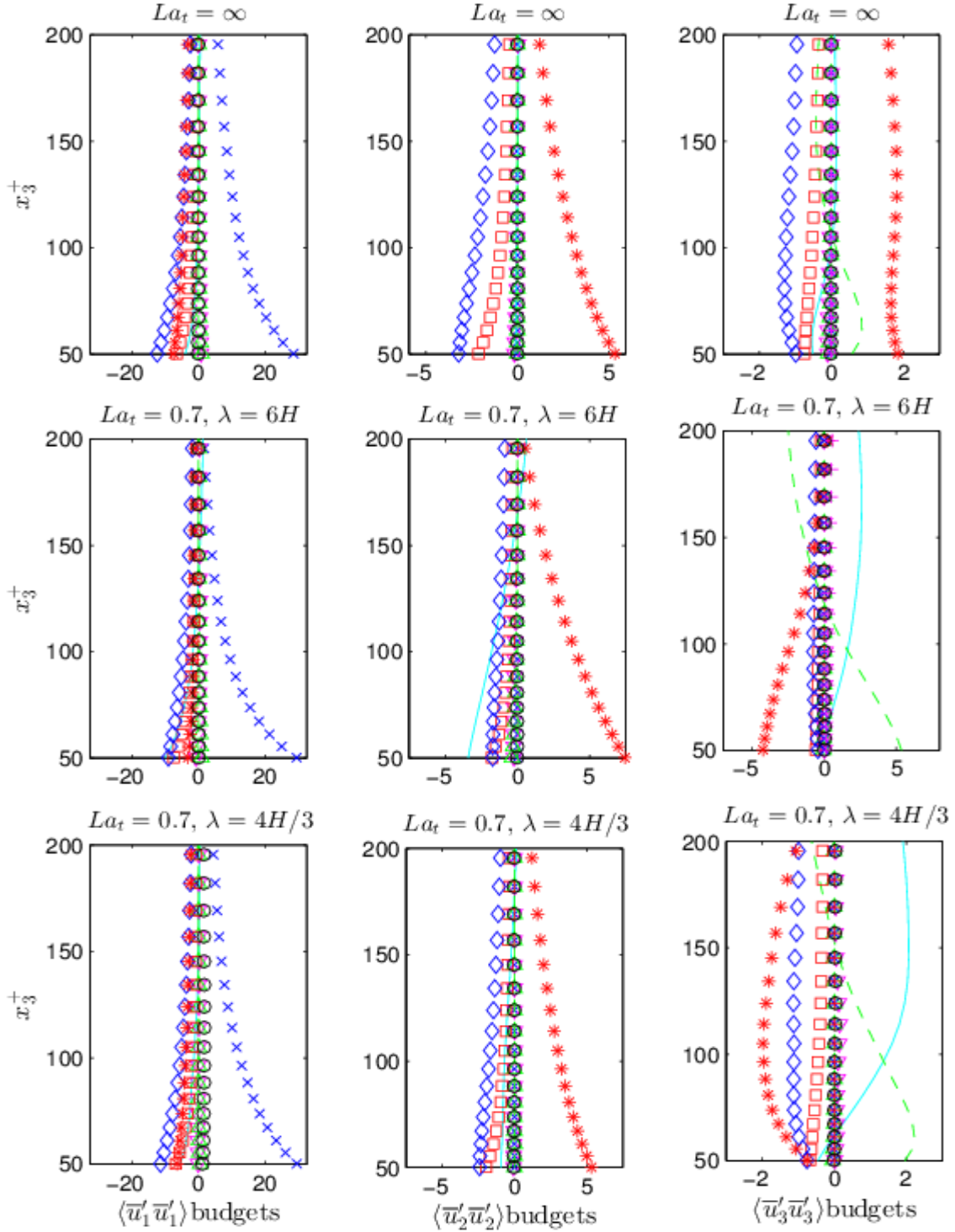


Figure 5.6 Near-bottom balance of TKE component budget terms (scaled by u_t^2) in flow with and without LC. — is turbulent transport, — — is pressure transport, ∇ is SGS transport, Δ is viscous diffusion, \square is viscous dissipation, \diamond is SGS dissipation, $*$ is pressure strain re-distribution, \times is mean velocity shear production, and $+$ is production by Stokes drift velocity shear. Definitions of these terms are given in (3-7)

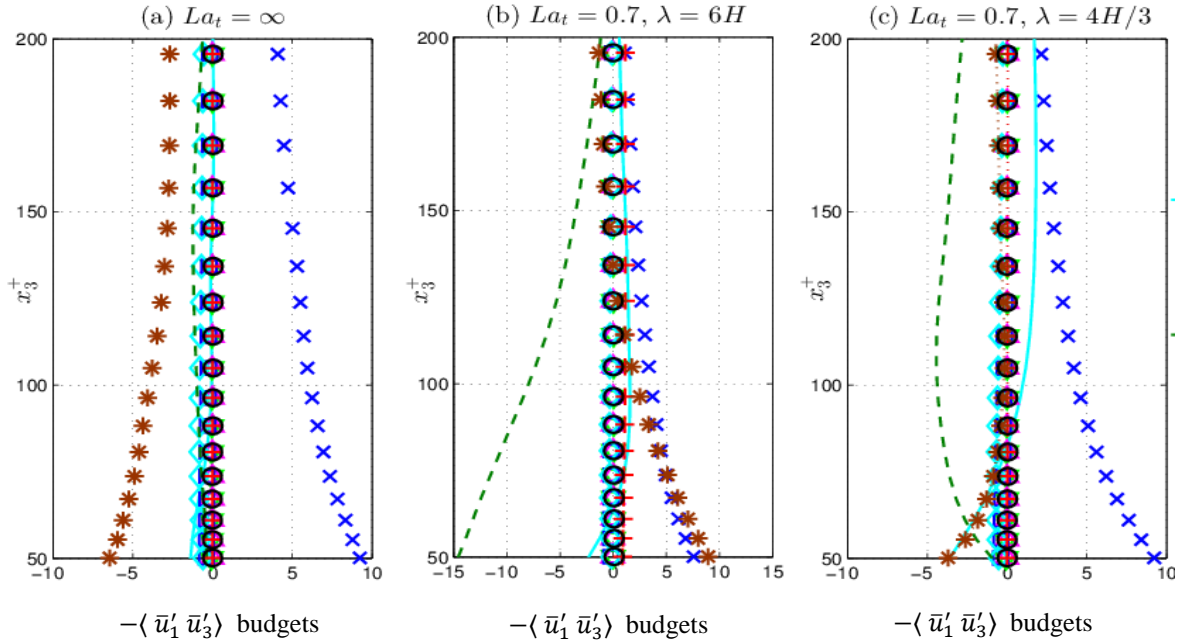


Figure 5.7 Near-bottom balance of Reynolds shear stress, $-\langle \bar{u}'_1 \bar{u}'_3 \rangle$, budget terms (scaled by u_τ^2) in flows with and flow without LC. $—$ is turbulent transport, $—$ is pressure transport, ∇ is SGS transport, Δ is viscous diffusion, \square is viscous dissipation, \diamond is SGS dissipation, $*$ is pressure strain re-distribution, \times is mean velocity shear production, and $+$ is production by Stokes drift velocity shear. Definitions of these terms are given in Chapter 3.

Figure 5.7 shows budgets of Reynolds shear stress $-\langle \bar{u}'_1 \bar{u}'_3 \rangle$ within the bottom log layer. Similar to the TKE budgets near the bottom (Fig. 5.4), production by mean velocity shear is a main source and production by Stokes drift shear is negligible given that Stokes drift shear diminishes towards the bottom of the water column (recall Figure 3.2b). In flows with LC, the case with $(La_t = 0.7, \lambda=6H)$ is characterized by significant turbulent transport as a source, unlike in the case with $(La_t = 0.7, \lambda=4H/3)$. The reason for this is that the full-depth LC is stronger in the $(La_t = 0.7, \lambda=6H)$ case compared to the $(La_t = 0.7, \lambda=4H/3)$ case as discussed earlier. A key difference between flows with and without LC is the role of pressure-strain re-distribution. In flow without LC, pressure strain re-distribution is the main sink in the log-layer region. In the flows with LC, pressure transport is the main sink. In the flow with $(La_t = 0.7,$

$\lambda=6H$) pressure strain re-distribution acts as a source, while in the flow with ($La_t = 0.7$, $\lambda=4H/3$) pressure strain re-distribution remains as a sink, similar to the flow without LC, but not as significant.

5.6 Conclusion

We have analyzed near-bottom mean velocity profiles and budgets of TKE resolved in large-eddy simulations of full-depth LC in a wind-driven shear current in neutrally-stratified shallow water. It was found that for sufficiently long waves, full-depth LC disrupts classical boundary layer dynamics. For example, full-depth LC can disrupt the log-law, inducing a “law of the wake-like” behavior. The disruption is primarily caused by the downwelling limb of LC which brings high speed fluid down to the log-layer region. The extent of this disruption depends on the strength of LC as determined through the wavelength (λ) of the surface waves generating the LC. Smaller λ generate weaker, less disruptive LC. . For sufficiently long wavelengths, the extent of the disruption also depends on the structure of LC as determined through the turbulent Langmuir number, La_t . For example lowering La_t from 0.7 to 0.4 while keeping λ at $6H$ strengthens the upwelling limb of the cell. A stronger upwelling limb is characterized by an increase in the rate at which it brings slower moving fluid up to the log-layer, thereby diminishing the log-layer disrupting effect of the downwelling limb.

Full-depth LC can also disrupt the classical log-layer balance between production and dissipation of TKE causing turbulent and pressure transport to play non-negligible roles in the dynamics. Furthermore, LC can impact the transfer of energy between TKE components inducing new behavior especially in terms of pressure-strain redistribution. In flows with full-depth LC, pressure-strain redistribution transfers energy from vertical to crosswind TKE

components, in contrast to classical boundary layers in which pressure-strain redistribution transfer energy from downwind to crosswind and vertical components.

Finally, turbulent transport was seen as an important source in the Reynolds shear stress budgets in cases when full-depth LC is sufficiently strong. This is similar to the behavior observed in the near-surface budgets of Reynolds shear stress in Chapter 4.

6 A K-profile Parameterization of Langmuir Turbulence in Shallow Water

6.1 Introduction

As described in the Introduction, the total number of grid points required for a direct numerical simulation should be $N \sim Re^{9/4}$. Most of the flows in applied sciences and engineering applications have a Reynolds number in range of $10^4 < Re < 10^8$. Therefore, the requirement of massive computational resources for DNS (direct numerical simulation) limits its applicability. Although large-eddy simulation offers a less computationally intensive alternative, it is still prohibitive in many applications such as in geophysical flows as LES requires resolution of a disparate range of scales extending from the largest scales of the turbulence down to the significantly smaller scales within the inertial subrange. In oceanic flows, one of the largest domains LES has been applied to consists of a 5.76 km by 10.5 km horizontal upper ocean region, 120 meters in depth with grid resolution of 3 meters (Skylingstad and Samelson, 2012). The focus of that study was to understand the breakdown of frontal sub-mesoscale eddies of ~ 1 km in horizontal scale into smaller scale turbulence. The necessity to study the general ocean circulation requires resolution of much larger scales. For example, the classical problem of wind-driven coastal upwelling and downwelling requires resolution of horizontal scales of $O(100 \text{ km})$, for which LES (say with grid cell size of $O(1 \text{ m})$) similar to that of Skylingstad and Samelson, 2012) is out of reach given current computational resources. In order to investigate such flow phenomena, researchers have turned to Reynolds-averaged Navier-Stokes (RANS) simulation methodology in which only the mean component of the flow is resolved while the effect of the

unresolved turbulent scales is parameterized via a turbulence model. The turbulence model appears in the governing RANS equations as a closure for the Reynolds stress often in terms of an eddy viscosity (see equations 1-17 and 1-18).

In oceanic applications involving the RANS simulation methodology, the eddy viscosity should represent turbulent mixing induced by unresolved horizontal and vertical eddies. For example, the horizontal eddies could be the sub-mesoscale frontal eddies discussed earlier of horizontal size $O(1 \text{ km})$ and the vertical eddies could be full-depth Langmuir cells of vertical size $O(10\text{-}20 \text{ m})$. Given this vast difference in length scales between horizontal and vertical eddies, which is typical in the ocean, horizontal and vertical diffusion in the RANS momentum equation is treated with different eddy viscosities (e.g. see Austin & Lentz, 2002). For example, in the x_1 momentum equation, the general diffusion term is expressed as

$$\frac{\partial}{\partial x_i} \left(v_t \frac{\partial \langle u_1 \rangle}{\partial x_i} \right) = \frac{\partial}{\partial x_1} \left(v_{hor} \frac{\partial \langle u_1 \rangle}{\partial x_1} \right) + \frac{\partial}{\partial x_2} \left(v_{hor} \frac{\partial \langle u_1 \rangle}{\partial x_2} \right) + \frac{\partial}{\partial x_3} \left(v_{ver} \frac{\partial \langle u_1 \rangle}{\partial x_3} \right) \quad (6-1)$$

where v_{hor} is horizontal eddy (turbulent) viscosity and v_{ver} is vertical eddy viscosity. The focus of this chapter is the development of a parameterization for vertical eddy viscosity that takes into account vertical mixing induced by the full-depth Langmuir cells studied in the previous chapters.

6.2 Vertical Turbulent Mixing Models for the Coastal Ocean

An important component of oceanic circulation modeling is the development of efficient and accurate parameterizations of the vertical mixing process. A large number of mixing schemes has been developed, amongst the most popular being the Mellor-Yamada model (Mellor and Yamada, 1982), the $\kappa - \epsilon$ model (Burchard et al., 1998) and the K-profile parameterization or

KPP (Large et al., 1994). Although these vertical mixing parameterizations have led to overall good performance of ocean circulation models under certain conditions, these models are not able to accurately represent vertical mixing during the occurrence of full-depth Langmuir circulation and associated Langmuir turbulence. The main focus of this study is the development of a new KPP accounting for full-depth LC. Results of the new KPP model implemented in a single water column RANS simulation of the wind-driven flows with full-depth LC studied in previous chapters are compared to LES results and to results of RANS with the standard KPP and the $\kappa - \epsilon$ models. Note that a description of the $\kappa - \epsilon$ model will not be given (see Burchard et al, 1998; Wilcox, 1994 for details), as the focus here is on the KPP.

6.3 K-Profile Parameterization

The standard KPP (Large et al., 1994) is a local parameterization of the Reynolds shear stress made under the assumption of the presence of surface and bottom (bed) log layers. The modified KPP developed here accounts for (i) surface and bottom log-layer disruption mainly caused by Stokes drift shear and full-depth LC, respectively (ii) non-local transport induced by full-depth LC and (iii) Reynolds shear stress production by Stokes drift shear. These effects have been revealed in previous chapters through LES of wind-driven flows with full-depth LC.

6.3.1 The Standard KPP Parameterization

The RANS turbulence model developed is based on the K-profile parameterization (or KPP) reviewed in (Large et al., 1994). The popularity of the KPP lies in its implementation simplicity given that it is an algebraic model unlike Mellor-Yamada and $\kappa - \epsilon$ model which necessitate solution of differential equations.

In the traditional KPP, the dominant component (i.e. the downwind (x_1)-wall-normal (x_3) component) of the Reynolds shear stress for our flows of interest (i.e. the flows with LC studied via LES in previous chapters) is modeled as

$$-\langle u'_1 u'_3 \rangle = \nu_t \frac{d\langle u_1 \rangle}{dx_3} \quad (6-2)$$

Note that here ν_t will denote vertical eddy diffusivity. Within the surface boundary layer this RANS eddy viscosity is taken as

$$\nu_t = \delta w(\sigma)G(\sigma) \quad (6-3)$$

where δ is the depth of the surface boundary layer, $w(\sigma)$ is a velocity scale and $G(\sigma)$ is a shape function. In general, velocity scale w and shape function G are functions of σ , a dimensionless coordinate varying between 0 at the surface of the water column and 1 at the base of the surface boundary layer. In the present implementation (for the homogeneous (neutrally stratified) flows of interest) the surface boundary layer is taken to be the upper half of the water column (see domain sketch in Fig. 3.1 in Chapter 3). Dimensionless coordinate σ is defined as $\sigma = z/\delta$, where z measures distance to the surface. Shape function G is taken to be a cubic polynomial:

$$G(\sigma) = a_0 + a_1\sigma + a_2\sigma^2 + a_3\sigma^3 \quad (6-4)$$

Velocity scale w and coefficients a_0 and a_1 are chosen so that the resulting eddy viscosity matches scale-similarity theory (i.e. log-layer dynamics) (Pope, 2000) near the surface. Velocity w is taken as $w = \kappa u_{\tau w}$ where $\kappa = 0.4$ is von Karman's constant and $u_{\tau w}$ is wind stress friction velocity. Thus, w is independent of σ . Furthermore, $a_0 = 0$ and $a_1 = 1$. These two values together with $w = \kappa u_{\tau w}$ ensure that ν_t goes as $\kappa u_{\tau w} z$ within the surface log-layer in accordance with similarity theory. In general, coefficients a_2 and a_3 are taken as

$$a_2 = -2 + 3G(1) - \partial_\sigma G(1) \quad (6-5)$$

$$a_3 = 1 - 2G(1) + \partial_\sigma G(1)$$

with

$$G(1) = \frac{v_{t0}}{\delta w(1)} \quad (6-6)$$

$$\partial_\sigma G(1) = \frac{\partial_z v_{t0}}{w(1)} - \frac{v_{t0} \partial_\sigma w(1)}{\delta w^2(1)}$$

So as to allow for the eddy viscosity to match the interior eddy viscosity v_{t0} at the base of the surface layer (here corresponding to the middle of the water column) (Large et al., 1994). Eddy viscosity v_{t0} is obtained via an interior parameterization typically dependent on a Richardson number describing water column stability. For the homogenous flows considered here, v_{t0} is independent of Richardson number. In wind-driven flow without Langmuir cells v_{t0} is taken as the eddy viscosity at the middle of the water column predicted by the $k - \epsilon$ model. For flows with Langmuir forcing and thus full-depth LC, determination of v_{t0} will be described further below. As will be seen for these cases, v_{t0} is an eddy viscosity associated with non-local transport and transport down the vertical gradient of Stokes drift velocity.

Since v_{t0} is a constant and in the standard KPP w is taken as independent of σ ($w = \kappa u_{\tau w}$), the coefficients in (6-5) become

$$a_2 = -2 + 3 \frac{v_{t0}}{\delta w} \quad (6-7)$$

$$a_3 = 1 - 2 \frac{v_{t0}}{\delta w}$$

for the standard KPP.

In the bottom half of the water column, within the bed log-layer, the eddy viscosity is expected to behave similar to the surface log-layer but as $\kappa u_{\tau b} z$ where $u_{\tau b}$ is bottom (bed) friction velocity and z is distance to the bottom wall. Shape function coefficients are also chosen so as to match the interior eddy viscosity ν_{t0} . Note that for flows studied in previous chapters, in the mean, bottom friction velocity, $u_{\tau b}$, is equal to wind-stress friction velocity $u_{\tau w}$, however, in general these two friction velocities do not have to be the same.

6.4 A Modified KPP

Recall that the generating mechanism of Langmuir turbulence and associated LC (i.e. Langmuir forcing) is the cross product between Stokes drift velocity induced by surface gravity waves and flow vorticity. The latter cross product, better known as the Craik-Leibovich vortex force, appears in the LES momentum equation. The LES results in the previous chapter (Chapter 4) have indicated that Langmuir forcing causes deviations from the classical surface similarity theory (i.e. surface log-layer dynamics) characteristic of surface stress-driven flows. Surface log-law disruption is primarily caused by Stokes drift velocity shear serving to intensify near-surface small-scale vortices (Figure 4.9) ultimately leading to enhanced mixing in the near-surface region (Fig. 4.16a). These results suggest the need for a near-surface eddy viscosity enhancement dependent on Stokes drift shear.

Based on analysis of Chapter 4 Langmuir forcing also affects water column dynamics of wind and wave-driven shallow water flows through the non-local effect of the coherent, full-depth upwelling and downwelling limbs of LC. For example, the downwells bring high speed fluid close to the bottom wall thereby inducing a deviation from the classical bottom log-law velocity profile. Furthermore, in some instances (under certain combinations of wind and wave

forcing) the full-depth cells can be sufficiently strong to lead to regions of negative vertical gradient of mean downwind velocity within the core or bulk of flow. Under this circumstance, the Reynolds shear stress closure requires an additional non-local term in addition to the traditional local term based on mean velocity vertical shear.

Finally, analysis of Reynolds shear stress budgets in Chapters 4 and 5 have revealed the importance of Stokes drift shear throughout the water column, suggesting that the Reynolds shear stress closure should have a term proportional to Stokes drift shear, similar to the usual local term proportional to mean velocity shear.

6.4.1 Modification of KPP Based on Near-Surface Dynamics

In order to account for Stokes drift shear-enhanced near-surface mixing in the KPP model, we proceed following (Teixeira, 2012). Analyzing the budget terms of Reynolds shear stress $-\langle u'_1 u'_3 \rangle$ presented in Chapter 3, it can be seen that production by mean wind-driven current velocity shear is $\langle u_3'^2 \rangle d\langle u_1 \rangle / dx_3$ while production by Stokes drift shear is $\langle u_1'^2 \rangle d\langle U_S \rangle / dx_3$ where U_S is the depth-dependent Stokes drift velocity, taken here to have non-zero component only in the downwind direction. Note that U_S is an input determined from the dominant wavelength, amplitude and frequency of the surface gravity waves generating Langmuir turbulence, as described earlier in Chapter 3. In an effort to find the influence of Langmuir turbulence on turbulent kinetic energy dissipation rate in the upper ocean, (Teixeira, 2012) decomposes the Reynolds shear stress as

$$-\langle u'_1 u'_3 \rangle = -\langle u'_1 u'_3 \rangle_{wind} - \langle u'_1 u'_3 \rangle_{Stokes} \quad (6-8)$$

where the first term on the right hand side is a component due to the wind-driven shear and the second term is a component due to the Stokes drift shear. Furthermore, assuming a constant shear stress layer at the surface (Pope, 2000), the total Reynolds shear stress can be taken as

$$-\langle u'_1 u'_3 \rangle = u_{\tau w}^2 \quad (6-9)$$

within the usual surface log-layer. The decomposition in (6-8) and the constant shear stress layer approximation in (6-9) suggest that $-\langle u'_1 u'_3 \rangle_{wind} < u_{\tau w}^2$. This along with the assumption that within the usual log-layer the primary sources of Reynolds shear stress are wind-driven shear production and Stokes drift shear production leads to the following expression (Teixeira, 2012):

$$-\langle u'_1 u'_3 \rangle_{wind} = \frac{u_{\tau w}^2}{1 + \frac{\langle u_1'^2 \rangle}{\langle u_3'^2 \rangle} \frac{d\langle U_s \rangle}{dx_3} / \frac{d\langle u_1 \rangle}{dx_3}} \quad (6-10)$$

The ratio

$$\gamma = \frac{\langle u_1'^2 \rangle}{\langle u_3'^2 \rangle d\langle u_1 \rangle / dx_3} \quad (6-11)$$

appearing in (6-10) may be parameterized using LES. Based on our own LES, we have found γ to be $O(\delta/u_{\tau w})$ within the usual surface log-layer and thus take it as simply $\gamma = \delta/u_{\tau w}$ (see Figure 6.1). Additionally, the total Reynolds shear stress budget collected from the LES (see Figure 4.14, repeated here as Figure 6.2 for convenience) shows that within this near-surface region, the dominant source terms are indeed production by wind-driven (mean velocity) shear and production by Stokes drift shear, lending support to equation (6-10).

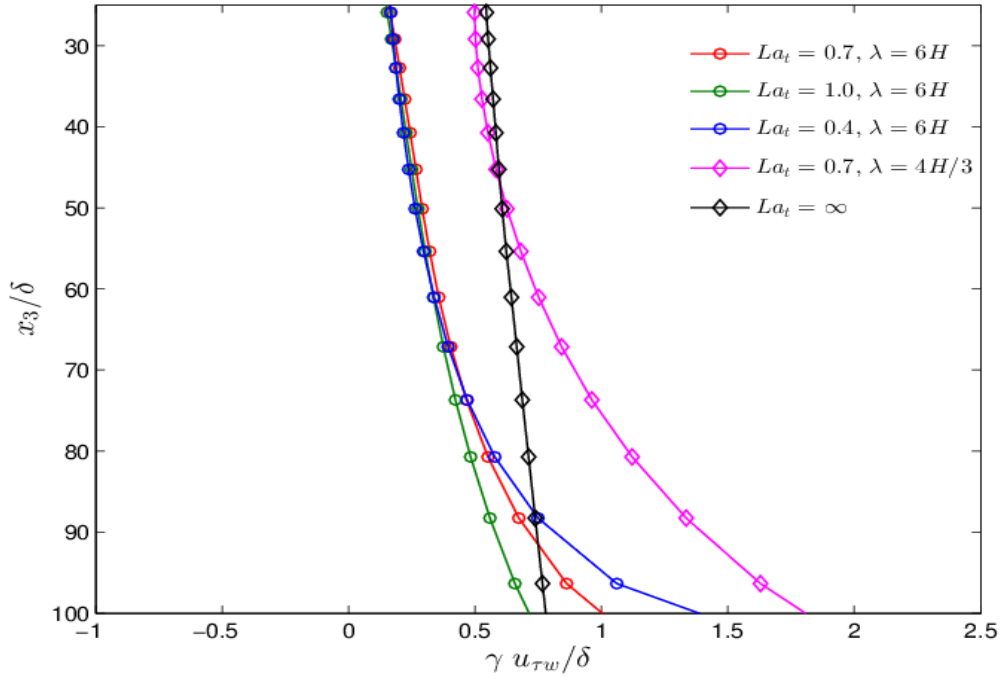


Figure 6.1 Parameter γ in Eqn. (6-11) evaluated using LES fields within the surface log-layer

The wind-driven shear component of the total Reynolds shear stress is modeled as

$$-\langle u'_1 u'_3 \rangle_{wind} = \nu_t \frac{d\langle u_1 \rangle}{dx_3} \quad (6-12)$$

with the eddy viscosity within the surface log-layer taken as $\nu_t = \kappa u_{\tau w} z$ (with z being distance to the surface). Equating (6-10) and (6-12) and making use of (6-11) leads to

$$\nu_t \left(1 + \gamma \frac{dU_s}{dx_3} \right) \frac{d\langle u_1 \rangle}{dx_3} = u_{\tau w}^2 \quad (6-13)$$

implying an amplified near-surface eddy viscosity with amplification factor $(1 + \gamma dU_s/dx_3)$.

Thus, the KPP model modified for near-surface dynamics induced by Langmuir turbulence results in

$$-\langle u'_1 u'_3 \rangle = \nu'_t \frac{d\langle u_1 \rangle}{dx_3} \quad (6-14)$$

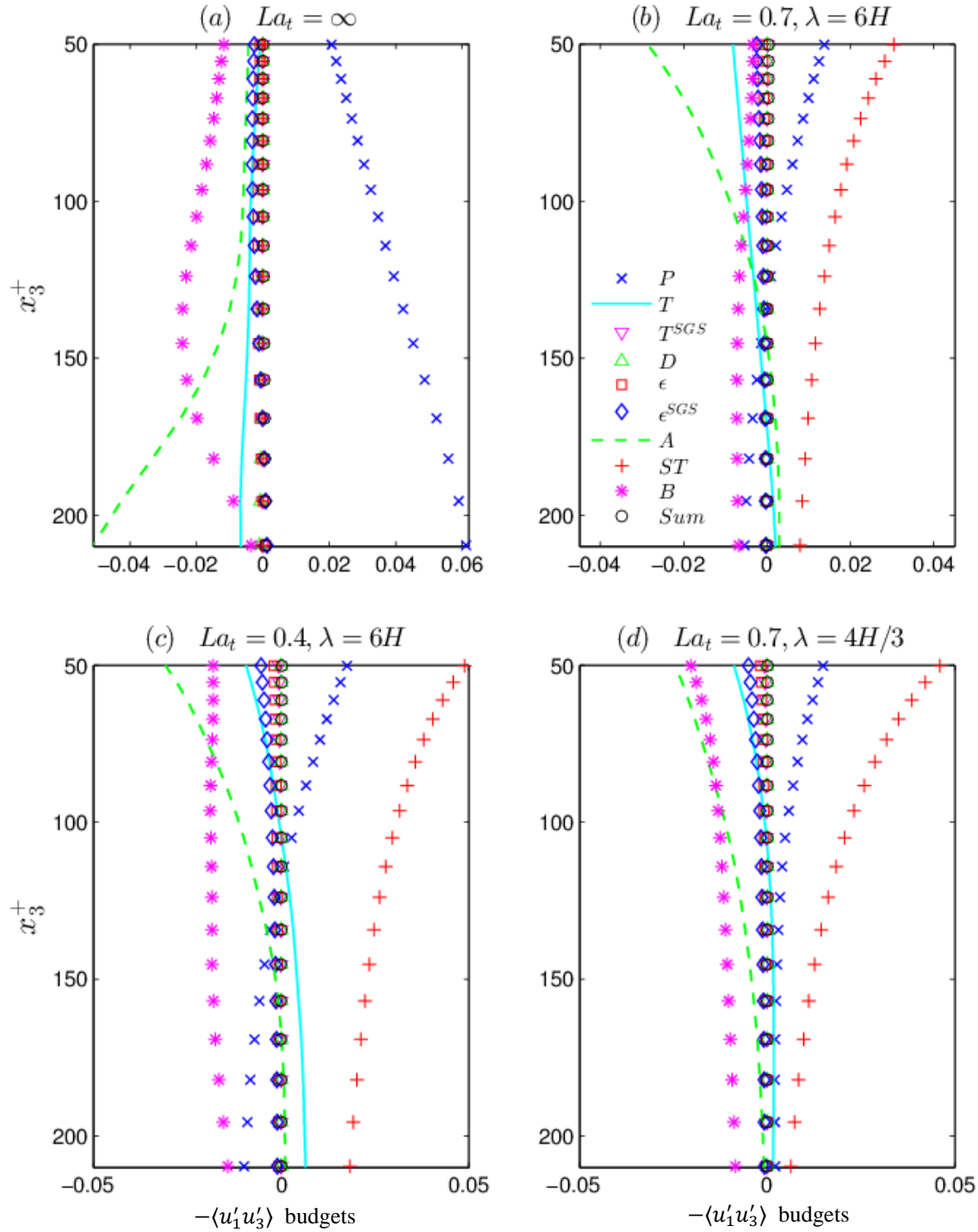


Figure 6.2 Near-surface budget terms of $-\langle \bar{u}'_1 \bar{u}'_3 \rangle$ (scaled by u_τ^2) in flows with and without LC. x_3^+ measures distance to the surface in plus units. P is production by mean velocity shear, T is turbulent transport, T^{SGS} is SGS transport, D is viscous diffusion, ϵ is viscous dissipation, ϵ^{SGS} is SGS dissipation, A is pressure transport, ST is production by Stokes drift shear and B is pressure-strain correlation.

with amplified eddy viscosity

$$v'_t = v_t \left(1 + \gamma \frac{d\langle U_s \rangle}{dx_3} \right) \quad (6-15)$$

where v_t is given in (6-3). This amplified eddy viscosity is consistent with LES results of Chapter 4 showing that Stokes drift shear serves to enhance near-surface mixing.

Recall that in the standard KPP, velocity scale w in (6-3) is taken independent of σ as $w = \kappa u_{\tau w}$ where $\kappa = 0.4$ is von Karman's constant and $u_{\tau w}$ is wind-stress friction velocity. The amplified eddy viscosity in (6-15) implies that the velocity scale should be

$$w = \left(1 + \gamma \frac{d\langle U_s \rangle}{dx_3} \right) \kappa u_{\tau w} \quad (6-16)$$

for the modified KPP of the total Reynolds stress in (6-11). Note that this new velocity scale affects the shape function coefficients calculated in (6-5). More specifically, the new velocity scale is no longer constant and is now a function of σ through the depth dependence of the Stokes drift vertical shear, dU_s/dx_3 . Thus, the shape function coefficients for the modified KPP are different than those for the standard KPP appearing in (6-7).

6.4.2 Modification of KPP Model Accounting for Non-Local Transport

As noted earlier, mixing induced by full-depth LC causes a negative slope in the vertical gradient of mean downwind velocity and thus a breakdown of the local model in (6-14). In order to account for this non-local effect induced by LC, the KPP model is augmented as

$$-\langle u'_1 u'_3 \rangle = v'_t \left(\frac{d\langle u_1 \rangle}{dx_3} + \Gamma \right) \quad (6-17)$$

where Γ is a counter-gradient defined as

$$\Gamma = \frac{u_{\tau w}^2}{v(\sigma)\delta} \quad (6-18)$$

where $v(\sigma)$ is a velocity scale. Counter-gradients such as this one have been proposed for non-local transport in the convective atmospheric boundary layer (see for example (Frech and Mahrt, 1995) and references within) and have been extended to the upper ocean mixed layer (see for example (Smyth et al., 2002)).

In the current implementation, general velocity scale $v(\sigma)$ is taken independent of σ as simply $\kappa u_{\tau w}$. It is not taken as that given by equation (6-16) because the latter is not representative of core (bulk) region non-local effects, but rather of the near-surface Stokes drift shear-enhanced mixing via small-scale vortices described in Chapter 4.

As per the discussion in previous section, the standard KPP eddy viscosity is designed to match the eddy viscosity (ν_{t0}) at the base of the surface layer taken to be middle of the water column and thus the amplified eddy viscosity of the modified KPP there becomes

$$\nu'_{t0} = \nu_{t0} \left(1 + \gamma \frac{dU_s}{dx_3} \right)_{x_3=0} \quad (6-19)$$

where $x_3 = 0$ denotes the middle of the water column. We find ν_{t0} by setting the counter-gradient term in (6-17) at the middle of the water column proportional to the wind stress:

$$\nu'_{t0}\Gamma = C u_{\tau w}^2 \quad (6-20)$$

where ν'_{t0} is given in terms of ν_{t0} in (6-19). The constant of proportionality, C , is a coefficient representative of the strength of the full-depth LC and Stokes drift shear being parameterized. If

wind and wave forcing conditions are such that the LC and Stokes drift shear are sufficiently strong to cause a negative slope in the vertical gradient of mean downwind velocity, then $C > 1$; otherwise, $C \leq 1$.

Inserting (6-15) with $\gamma = \delta/u_{\tau w}$ into (6-17) and expanding reveals that the modified KPP contains the term $(v_t \Gamma \delta / u_{\tau w}) dU_s / dx_3$. This term represents flux down the vertical gradient of Stokes drift. The Reynolds shear stress transport equation derived from the momentum equation with Craik-Leibovich (Langmuir) forcing (serving to generate Langmuir turbulence) possesses production by vertical gradients of mean downwind velocity and Stokes drift velocity, $d\langle u_1 \rangle / dx_3$ and dU_s / dx_3 , respectively, as shown in Chapter 3. This along with the LES-based analysis of Reynolds shear stress transport equation terms (budget terms) in Chapter 4, suggest that a parameterization of the Reynolds shear stress should contain a vertical flux down the gradient dU_s / dx_3 , in addition to the usual flux down the gradient $d\langle u_1 \rangle / dx_3$. Reynolds shear stress parameterizations including transport down the gradient dU_s / dx_3 have been postulated (although not tested *a priori*) in (Harcourt and D'Asaro, 2008) and (McWilliams et al., 2012) for Langmuir turbulence in the upper ocean mixed layer. Note that Langmuir turbulence in the upper ocean mixed layer possess a number of differences from Langmuir turbulence in shallow water, primarily associated with the coherency of the full-depth LC in shallow water. In the shallow water case, full-depth LC tends to be strongly coherent contributing greatly to negative slope of $d\langle u_1 \rangle / dx_3$ and thus significant non-local effects extending down to (and disrupting) the bottom log-layer. In the upper ocean, the LC are less coherent and, obviously, do not interact with the bottom log-layer.

6.5 A Priori Evaluation of the Modified KPP Model

Single water column RANS simulations of wind-driven flows at $Re_\tau = 395$ (based on wind stress friction velocity and water column mid-depth) with full-depth LC were performed with the standard KPP, the $k - \varepsilon$ model and the newly proposed modified KPP for various combinations of wind and wave forcing. LES results of these same flows were presented in Chapters 3, 4 and 5. Recall that wind-driven flows with LC are characterized by the dominant wavelength of surface gravity waves (λ) generating LC and the turbulent Langmuir number (La_t) which is inversely proportional to the strength of wave forcing relative to wind forcing. Four cases have been simulated: ($La_t = 0.7, \lambda = 6H$), ($La_t = 0.4, \lambda = 6H$), ($La_t = 1.0, \lambda = 6H$) and ($La_t = 0.7, \lambda = 4H/3$).

RANS simulations consisted of solving the Reynolds averaged continuity equation and momentum equation with Craik-Leibovich vortex force. The domain consisted of a single water column, i.e. a one dimensional domain extending from $x_3 = 0$ at the bottom of the water column and $x_3 = 2\delta$ (same depth as the LES domain). In this domain, the mean velocity $\langle u_1 \rangle$ is dependent on x_3 . The domain was discretized with 33 equally distant points, thus the first grid point away from the bottom (surface) was at a distance $z_1^+ = 25$ from the bottom (surface). As a result, these simulations do not resolve viscous nor buffer sublayers and resolution only extends into the log layer. The surface boundary condition consists of a prescribed wind stress, the same as in the LES described in Chapter 3. The bottom boundary condition will be described in detail further below.

Figure 6.3 compares mean downwind velocity predicted by LES and by RANS with modified KPP, standard KPP and $k - \varepsilon$ model. With respect to LES, the RANS with modified

KPP leads to a better prediction than with standard KPP and $k - \varepsilon$ model in representing (i) the mixing of momentum throughout the bulk flow region and at the bottom of the water column induced by full-depth LC and (ii) the near-surface mixing induced by near-surface small scale vortices enhanced by Stokes drift shear. In some cases, the simulations with modified KPP tend to over-predict the near-surface mixing of momentum such as in the flow with $(La_t = 0.7, \lambda = 4H/3)$. This is attributed to the coarse mesh which only provides two grid points to resolve the rapid transition of the mean velocity at the surface.

Recall that the modified KPP coefficient C in (6-20) is representative of the strength of the full-depth LC and Stokes drift shear (i.e. the strength of Langmuir turbulence) at mid-depth being parameterized. From the results in Figure 6.3, it can be concluded that the C coefficient is primarily dependent on the strength of full-depth LC in the upper-half of the water column as measured through $\langle \bar{u}'_3 \bar{u}'_3 \rangle_{LC}$ defined in Eqn. (4-1) in Chapter 4 and plotted in Figure 4.8b for the various cases with LC. The quantity $\langle \bar{u}'_3 \bar{u}'_3 \rangle_{LC}$ represents the contribution of full-depth LC to vertical velocity variance $\langle \bar{u}'_3 \bar{u}'_3 \rangle$.

Figure 6.3 show results with $C = 1$ and with tuned values of C so as to yield mean velocity profiles in closer agreement with the LES. The tuned values of C are consistent with the strength of LC in the upper-half of the water column evaluated through $\langle \bar{u}'_3 \bar{u}'_3 \rangle_{LC}$ as previously discussed (see Fig. 4.8a): for $(La_t = 0.4, \lambda = 6H)$, $C = 1.4$; for $(La_t = 0.7, \lambda = 6H)$, $C = 1.2$; for $(La_t = 1, \lambda = 6H)$, $C = 1.1$; and for $(La_t = 0.7, \lambda = 4H/3)$, $C = 0.7$. Thus, as expected, a parameterization of the effect of a weaker full-depth LC in the upper-half of the water column via the modified KPP requires a smaller value of C . Future research should focus on obtaining a parameterization of C

in terms of La_t and λ by performing a suite of LES simulations sweeping through a range of these parameters.

In addition to being dependent on the Reynolds shear stress model, the previous results are also strongly dependent on the bottom boundary condition of the simulations. The bottom boundary condition and its modification to account for log-law disruption caused by full-depth LC will be described in the detail in the upcoming sub-section.

Figure 6.4 shows momentum balances in the RANS simulations of wind-driven flows with LC for the cases ($La_t = 0.4, \lambda = 6H$) with $C = 1.4$, ($La_t = 0.7, \lambda = 6H$) with $C = 1.2$, ($La_t = 1, \lambda = 6H$) with $C = 1.1$, and ($La_t = 0.7, \lambda = 4H/3$) with $C = 0.7$. The RANS equation governing these flows yield the following balance:

$$\nu \frac{d\langle u_1 \rangle}{dx_3} - \langle u'_1 u'_3 \rangle = u_{\tau w}^2 \quad (6-21)$$

where the first term on the left hand side is the local molecular viscous stress. The Reynolds stress is modeled via the modified KPP modeled in (6-20) yielding

$$-\langle u'_1 u'_3 \rangle = \nu'_t \frac{d\langle u_1 \rangle}{dx_3} + \nu_t \Gamma \frac{d\langle U_s \rangle}{dx_3} + \nu_t \Gamma \quad (6-22)$$

The first term on the right hand side is the local eddy viscosity stress or flux, the second term is vertical flux down the gradient of Stokes drift and the third term is the non-local flux. Figure 6.4 shows that the four stresses (local molecular viscosity stress, local eddy viscosity stress, non-local flux and flux down the gradient of Stokes drift) sum to the square of the wind stress friction velocity, $u_{\tau w}^2$, as expected.

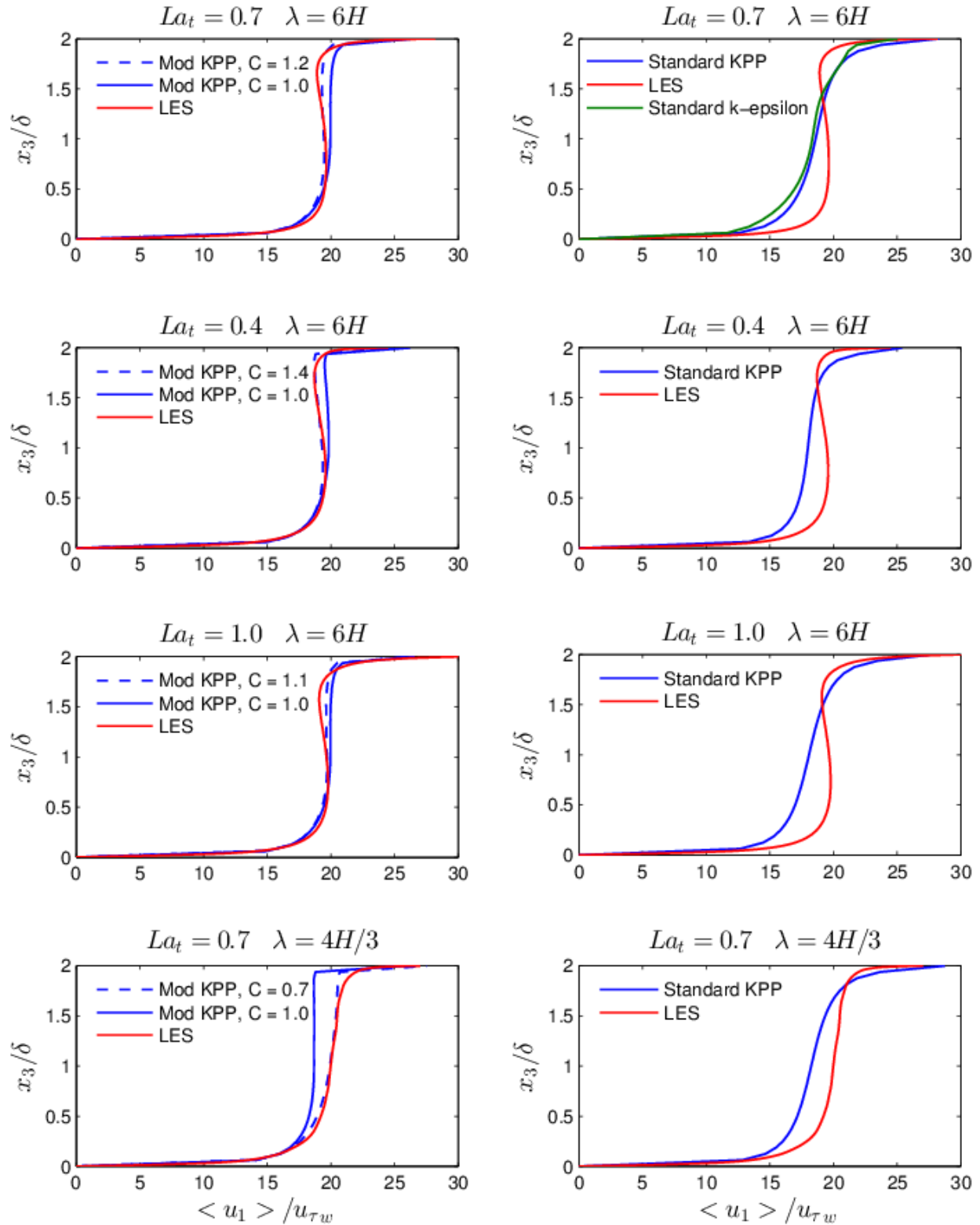


Figure 6.3 Comparison between RANS and LES of flows with LC at $Re_{\tau} = 395$. RANS is performed with the $k - \varepsilon$ model, the standard KPP and the modified KPP accounting for Langmuir turbulence and associated full-depth LC. Note that $H = 2\delta$ is the depth water column.

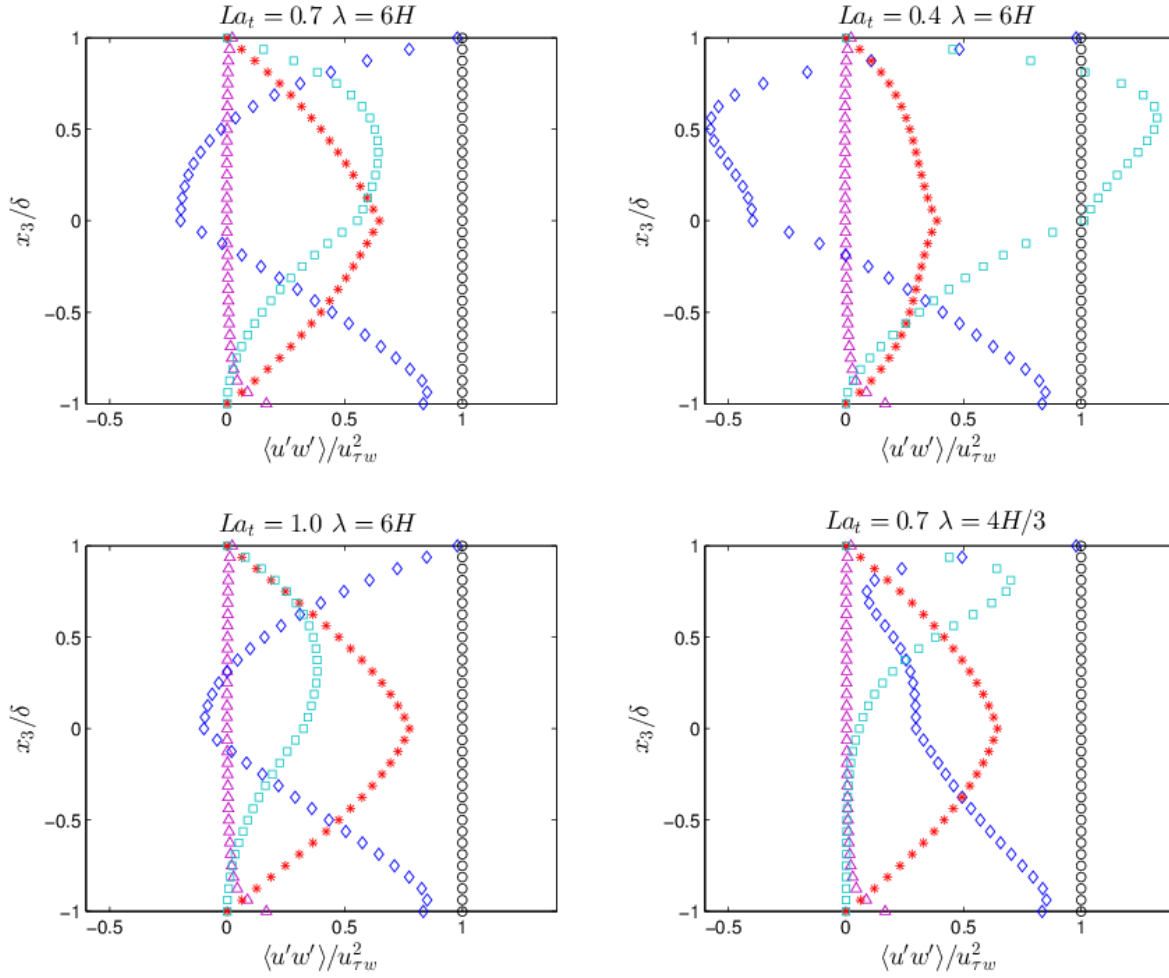


Figure 6.4 Momentum balance for modified nonlocal KPP in flows with LC at $Re_\tau = 395$. *: local eddy viscosity stress, Δ : local molecular viscous stress, \diamond : non-local stress \square : flux down the gradient of Stokes drift velocity, \circ : sum

Looking at Figure 6.4, in flows where the contribution of the flux down the gradient of Stokes drift is lower (e.g. in the flow with $(La_t = 1.0, \lambda = 6H)$) the contribution of the non-local stress is higher and vice-versa. For example, in the flow with $(La_t = 1.0, \lambda = 6H)$, Stokes drift shear is smallest compared to the other flows, leading to relatively small contribution from the flux down the gradient of Stokes drift in the modified KPP model. Furthermore, the presence of the full-depth LC in this case serves to homogenize the entire water column leading to small contributions from the local stresses especially in the middle of the water column (which is expected given that these stresses are proportional to vertical gradient of mean downwind

velocity). As a result, in the ($La_t = 1.0, \lambda = 6H$) case, the non-local stress is left to provide the bulk of wind shear stress vertical transfer throughout the water column, serving to explain why the non-local stress in this flow is higher than in the other cases.

Finally note that in Figure 6.4, in some of the flows it is seen that the local eddy viscosity stress becomes negative throughout significant portions of the water column (e.g. in the ($La_t = 1.0, \lambda = 6H$) case). This is due to the negative vertical gradient of mean downwind velocity induced by full-depth LC, consistent with the LES results presented in Chapters 4 and 5.

6.6 Bottom Boundary Condition

In the single water column RANS simulations previously described, the bottom boundary condition consists of a prescribed bottom stress rather than a no-slip condition. The reason for this is that the no-slip condition would require resolution of the buffer and viscous wall regions below the log-layer. In order to avoid resolution of these computationally expensive regions, the RANS simulation performed relies on imposition of the bottom stress rather than the no-slip condition in what is often referred to as near-wall modeling. The bottom stress is defined in terms of the bed stress friction velocity (which in these flows is equal to the wind stress friction velocity, $u_{\tau w}$). In near-wall modeling [(Li et al., 2010), (Piomelli and Balaras, 2002)] the bed stress friction velocity is obtained by assuming that the computed mean velocity, $\langle \bar{u}_1 \rangle$, satisfies the log-law at the first grid point away from the bottom wall:

$$\frac{\langle \bar{u}_1 \rangle}{u_{\tau w}} = \frac{1}{\kappa} \ln \left(\frac{u_{\tau w} z}{\nu} \right) + B \quad (6-23)$$

where $B=5.2$ for classical boundary layers. In traditional near-wall modeling, the previous equation is solved dynamically (i.e. during the simulation) for $u_{\tau w}$ with z set equal to the

distance between the wall and the first grid point away from the wall and $\langle \bar{u}_1 \rangle$ set as the computed mean velocity at the first grid point away from the wall.

LES presented in Chapter 5 has shown that full-depth LC disrupts the bottom log-law velocity profile in equation (6-23). The behavior induced by the LC can be approximated by varying the value of B depending on the strength of full-depth LC in the lower half of the water column. For example, in flow with $(La_t = 0.7, \lambda = 6H)$ the LES of Chapter 5 has shown that the disrupted log-law caused by full-depth LC may be approximated by re-setting B to 7.5 in the log-law in (6-23). In flow with $(La_t = 0.7, \lambda = 4H/3)$ in which the full-depth LC is weaker in the lower half of the water column than in the $(La_t = 0.7, \lambda = 6H)$ case, LES of Chapter 5 has shown that the disrupted log-law may be approximated by re-setting B to 6.5. Thus, a stronger LC in the lower-half of the water column requires a higher value of B . Similar conclusions can be arrived at by comparing the cases with $(La_t = 0.7, \lambda = 6H)$ and $(La_t = 0.4, \lambda = 6H)$.

Figure 6.5 shows mean velocities obtained in RANS simulations with the modified KPP with different values of the B coefficient in the log-law used for near-wall modeling. For example, in the flow with $(La_t = 0.7, \lambda = 6H)$, the log-law in (6-23) with $B=7.5$ leads to a velocity profile in better approximation of the LES velocity profile than the traditional $B=5.2$, as expected. The difference between using $B=5.2$ and $B=7.5$ in the RANS single water column simulation with modified KPP model is shown in Figure 6.5. The importance of the B coefficient in the near-wall model is further demonstrated in Figure 6.5 for the flow with $(La_t = 0.7, \lambda = 4H/3)$. Following the LES results of Chapter 5 and setting $B=6.5$ in the near-wall model in the RANS simulation with modified KPP leads to a better result than $B=5.2$.

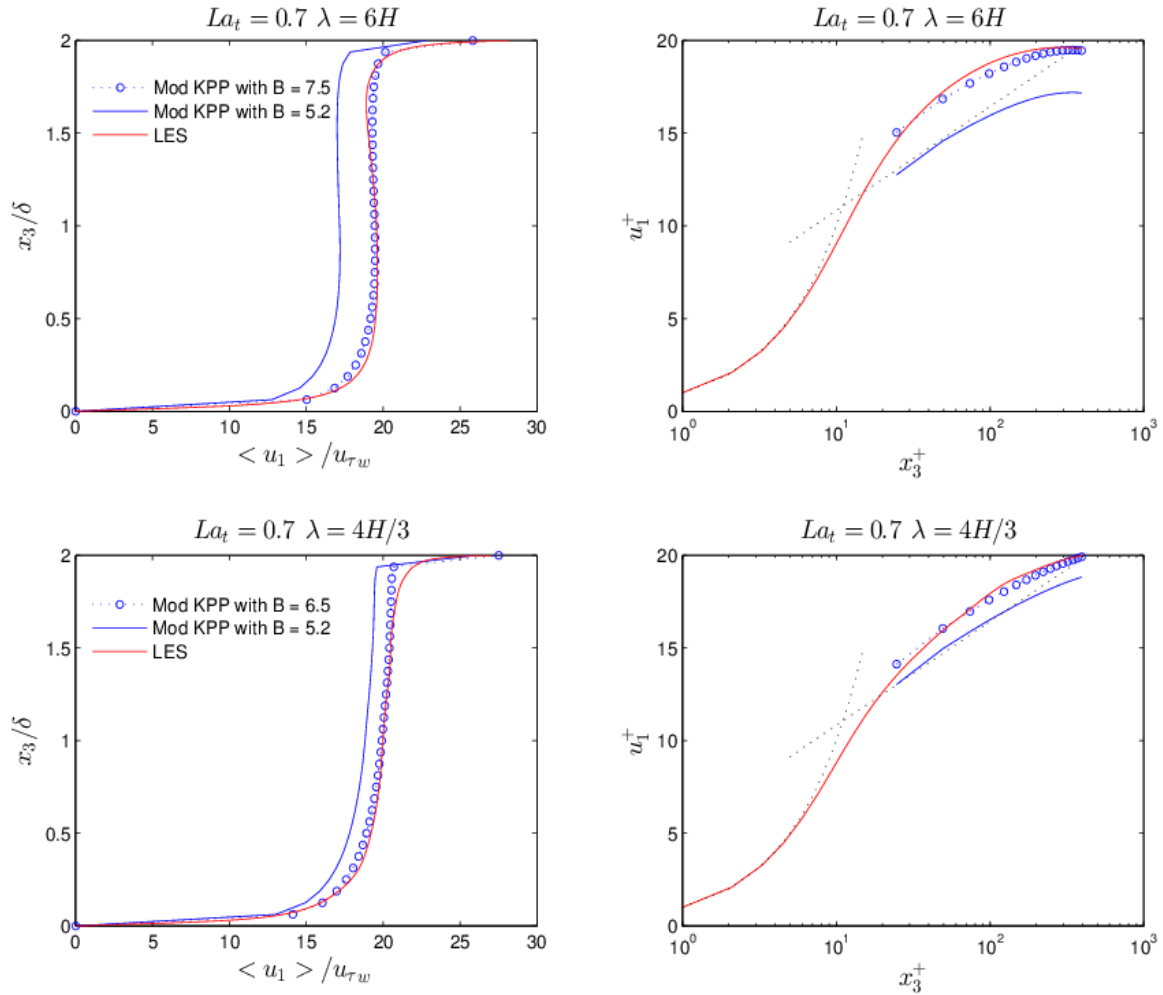


Figure 6.5 Mean downwind velocity predicted in RANS with modified KPP and various different values of B coefficient in the log-law used for near-wall modeling.

6.7 Conclusion

Langmuir turbulence is generated by interaction between Stokes drift velocity induced by surface gravity waves and the wind-driven shear. In homogeneous shallow water, Langmuir turbulence is often characterized by full-depth LC engulfing the entire water column. LES of Langmuir turbulence with full-depth LC in a wind-driven shear current has revealed that mixing due to full-depth LC erodes the bottom log-law velocity profile inducing a profile resembling a wake law. The full-depth LC also induces negative mean velocity shear under certain

combinations of wind and wave forcing parameters. Meanwhile, near the surface, Stokes drift shear serves to intensify small scale eddies leading to enhanced mixing and disruption of the surface velocity log-law.

A K-profile parameterization (KPP) of the Reynolds shear stress comprised of local and nonlocal components has been introduced capturing these basic mechanisms by which full-depth LC and associated turbulence impact the mean flow. Single water column RANS simulations with the new parameterization were presented showing good agreement with LES in terms of mean velocity profiles. The KPP introduced is characterized by two coefficients (C and B) dependent on the strength of the full-depth LC in the upper half of the water column and its strength in the bottom half of the water column. Future research should focus on parameterizing these coefficients as functions wind and wave forcing parameters λ and La_t by performing a suite of LES over likely values of λ and La_t .

7 Influence of Strong Tidal Current on LC in Shallow Continental Shelf

7.1 Introduction

Full-depth LC in the shallow coastal ocean is affected by the action of tides. For example, Figure 7.1 shows field measurements of full-depth LC by Gargett and Wells (2007) during a time of relatively weak tidal velocities at 20 cm s^{-1} . In this case, downwind velocity fluctuations are intensified near the bottom of the water column. A similar behavior was also observed in the LES of full-depth LC without the effect of tides presented in Chapters 4 and 5 (e.g. see Figure 4.3). Figure 7.2 shows field measurements of full-depth LC by Gargett and Savidge (2008) during a time of relatively strong tidal velocities at 60 cm s^{-1} . Unlike the case in Figure 7.1, here the downwind velocity fluctuations are not intensified near the bottom. Furthermore, in this case with stronger tidal velocities, the downwelling/upwelling limbs of the cells (exhibited through the vertical velocity fluctuations) are not as coherent nor as wide in the cross-wind direction as the downwelling/upwelling limbs in the case with weaker tidal velocities in Fig. 7.1.

Kukulka et al. (2011) performed LES of full-depth LC under a constant crosswind body force and noted that the body force induces an attraction mechanism between cells ultimately causing the cells to merge. The merged cells are characterized by wider crosswind size than the original cells without the effect of the crosswind pressure gradient. Simulations conducted by Martinat et al. (2011) using the same LES code used here, also found the same attraction mechanism.

Simulations performed for this dissertation also found similar results. Furthermore, it has also

been found that the merging of cells occurs when the crosswind body force is sufficiently weak relative to the downwind surface force caused by the wind stress. For example, when the crosswind Reynolds number (based on crosswind bottom friction velocity and water column half-depth) is one-half of the downwind Reynolds number (based on downwind bottom friction velocity and water column half-depth), the attraction between cells was observed for a case with $\lambda = 6H$ and $La_t = 0.7$.

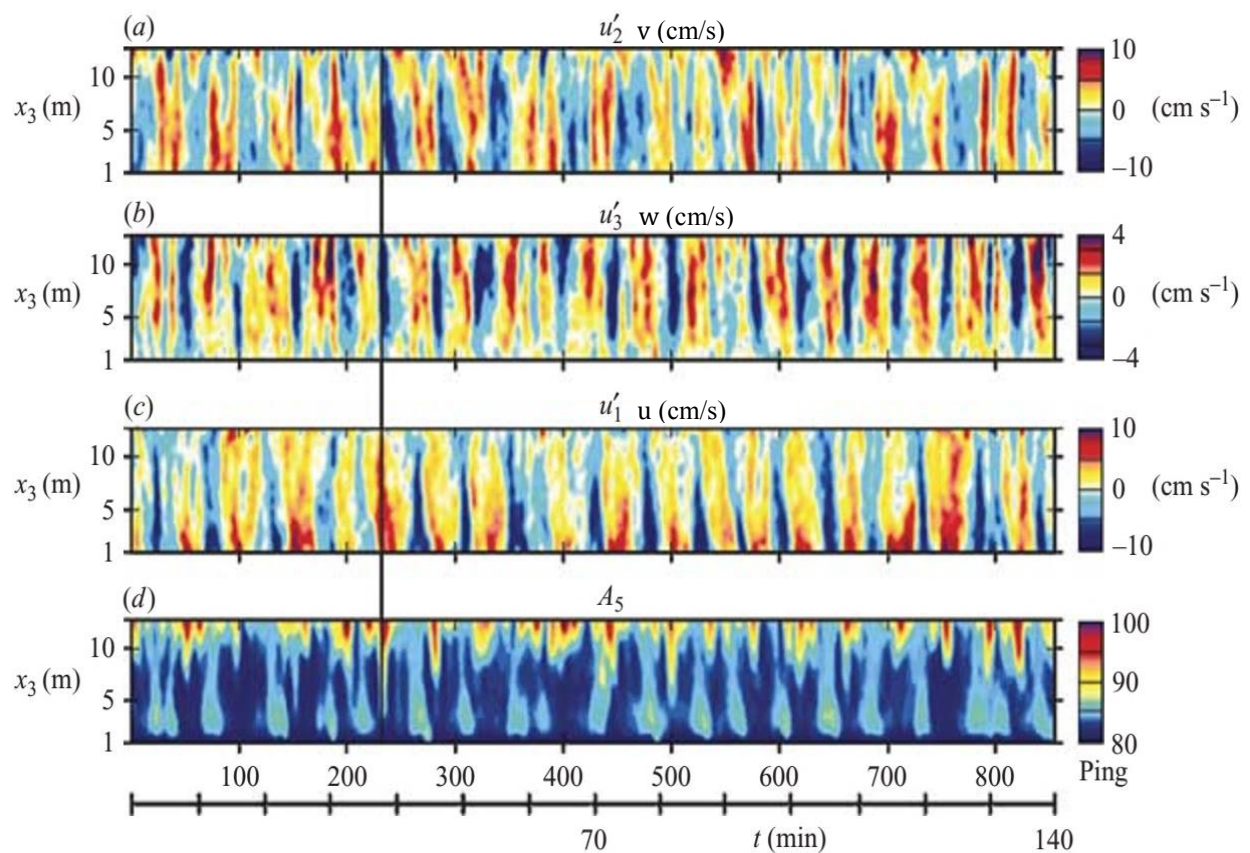


Figure 7.1 Fields of fluctuating velocity components in downwind (u), crosswind (v) and vertical (w) directions and backscatter amplitude (A_5) measured using an acoustic Doppler current profiler (Gargett and Wells 2007). Measurements were made under relatively weak tidal velocities of $\sim 20 \text{ cm s}^{-1}$. Measurements were made on the continental shelf off southern New Jersey at depth of 15 meters. Note: 10 pings ~ 1.5 minutes. [Ann E. Gargett and J. R. Wells (2007). Langmuir turbulence in shallow water. Part 1. Observations. *Journal of Fluid Mechanics*, 576, pp 27-61. Reprint with permission from Cambridge University Press]

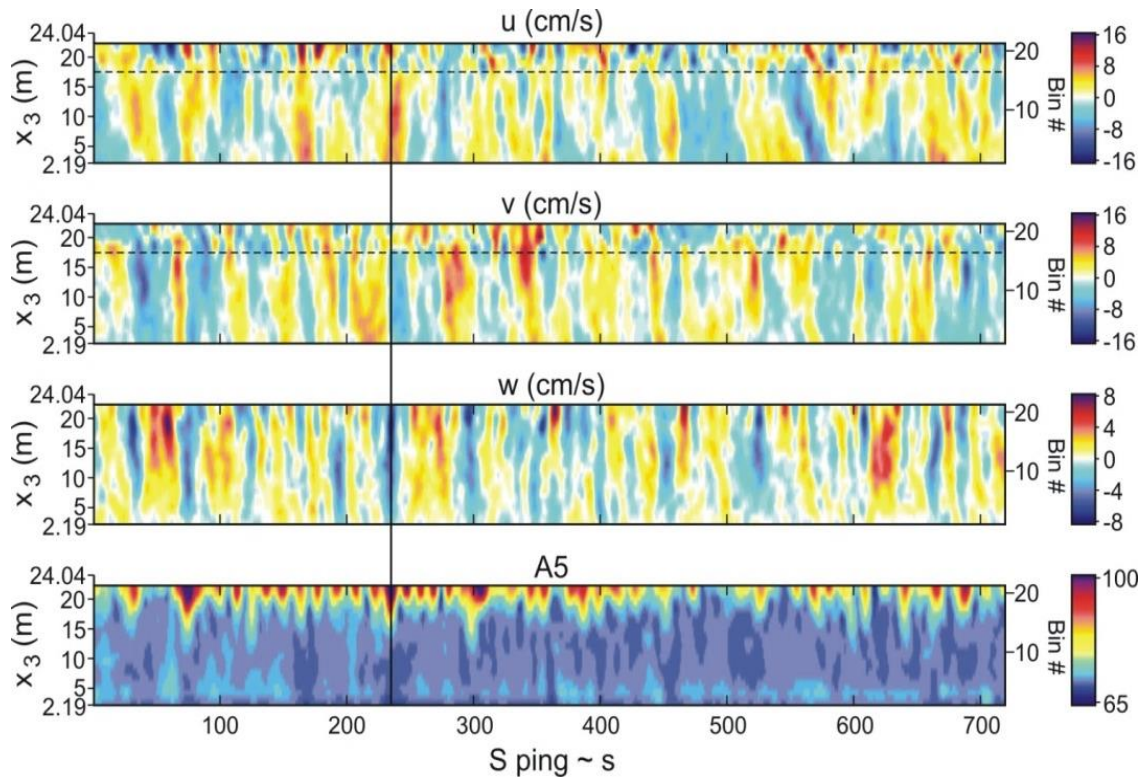


Figure 7.2 Fields of fluctuating velocity components in the downwind (u), crosswind (v) and vertical (w) directions and backscatter amplitude measured using an acoustic Doppler current profiler (Gargett and Savidge 2008). Measurements were made under relatively strong tidal velocities of $\sim 60 \text{ cm s}^{-1}$. Measurements were made on the continental shelf off Georgia at depth of 30 meters. [Savidge, W.B., A. Gargett, R.A. Jahnke, J.R. Nelson, D.K. Savidge, R.T. Short, and G. Voulgaris. 2008. Forcing and dynamics of seafloor-water column exchange on a broad continental shelf. *Oceanography* 21(4):179–184]

However, when the crosswind Reynolds number was increased such that it became equal to the downwind Reynolds number, the cells were observed to undergo a dramatic change in structure. In this case the relatively stronger constant crosswind body force led to crosswind shear able to break up the LC cells into smaller scale cells characterized by smaller crosswind size. Although the smaller scale cells reach the bottom of the water column, their disruption of the bottom boundary layer is not as prominent as that reported earlier in Chapter 5 for full-depth LC without crosswind body force. The previously described results were all obtained with constant pressure gradient (body force) in the crosswind direction. Langmuir turbulence occurs

on timescales significantly shorter than the time period of a full tidal cycle. Thus the constant crosswind body force applied in these cases represents the force during a time period of the tidal cycle which is longer than the timescale of the turbulence, but sufficiently smaller than the tidal period to assume the tidal force is temporarily constant. In this Chapter results are presented from LES with an oscillating crosswind body force representative of a crosswind tidal cycle. The peak value of the crosswind body force is selected such that it matches the intensity of the downwind force caused by the wind stress. The goal is to reveal the effect of the body force at different phases of the cycle on the LC structure, the overall Langmuir turbulence structure and associated disruption of the surface and bottom log laws observed in Chapters 4 and 5. For example, as will be shown further below, the cycle is characterized by times when the crosswind body force leads to the break-up of full-depth LC into smaller scale LC as found in cases with constant body force described earlier. The weakening of the body force as the tide transitions from peak tide to low tide leads to the re-emergence of the full-depth LC structure described in Chapters 4 and 5 for cases without tides.

7.2 LES Equations and Flow Configuration

The governing LES equations are the same as those discussed in Chapter 3, but now augmented with a time-dependent dimensionless body force, Af_2 , in the crosswind direction:

$$\frac{\partial \bar{u}_i}{\partial x_i} = 0 \quad (7-1)$$

$$\frac{\partial \bar{u}_i}{\partial t} + \bar{u}_j \frac{\partial \bar{u}_i}{\partial x_j} = -\frac{\partial \bar{\Pi}}{\partial x_i} + \frac{1}{Re_\tau} \frac{\partial^2 \bar{u}_i}{\partial x_j^2} - \frac{\partial \tau_{ij}^{LES(d)}}{\partial x_j} + \frac{1}{La_t^2} \epsilon_{ijk} U_j^s \bar{\omega}_k + Af_2 \delta_{i2} \quad (7-2)$$

where δ_{ij} is Kronecker's delta. The body force Af_2 consists of an oscillating component f_2 varying between -1 and +1. The period of oscillation was taken as 12.5 hours; this period is made dimensionless with a wind stress friction velocity of 0.009 m s^{-1} and water column half-depth of 7.5 m, characteristic of the field measurements of full-depth LC of Gargett and Wells (2007). The Reynolds number based on mean bottom downwind friction velocity (equal to wind stress friction velocity) is set to 360. Furthermore, the peak value of the crosswind body force, A , is selected such that it matches the intensity of the downwind force cause by the wind stress. Wind and wave forcing parameters are chosen as $\lambda = 6H$ and $\text{Lat} = 0.7$, which were values characterizing the field measurements of Gargett and Wells (2007).

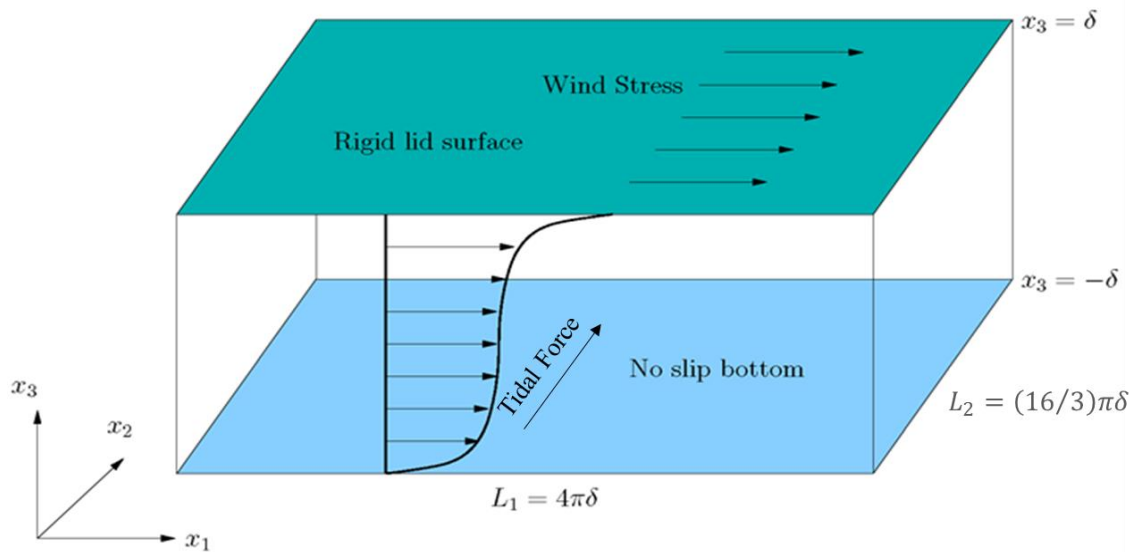


Figure 7.3 Sketch of LES domain in simulations with oscillating crosswind body force.

The flow domain for the LES in this study is shown in Figure 7.3. Note that crosswind size has been expanded by a factor of 2 relative to the domain used in the LES of Chapters 4 and 5 (see Figure 3.1). The reason for this is to enable resolution of at least two full-depth Langmuir cells and thus allow for the possibility of the merging of these cells as a result of the crosswind body force; recall that the LES simulations of Kukulka et al. (2011) and Martinat et al. (2011)

with constant crosswind body force revealed an attraction mechanism between full-depth cells that promotes the merging of the cells.

First a simulation was carried out with the expanded domain resolving two full-depth Langmuir cells without tidal forcing. Then the tidal forcing was turned on from zero gradually increasing towards peak tide following the oscillation shown in Figure 7.4. The simulation ran for more than 3 tidal cycles beyond which point no significant differences in the turbulence structure were observed between peak tide and low tide. The initial condition is shown in Figure 7.5 in terms of crosswind-vertical variation of downwind-averaged streamwise, crosswind and vertical velocity fluctuations. This figure reveals two full-depth Langmuir cells, with the same structural characteristics described earlier in Chapter 4.

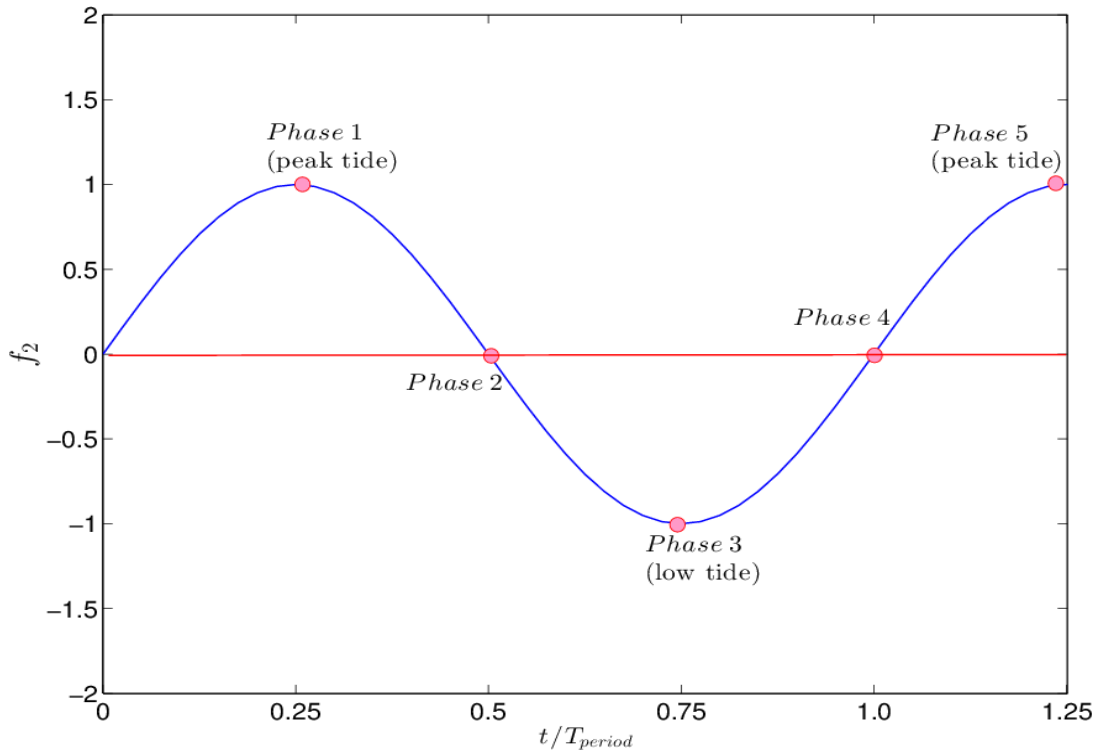


Figure 7.4 Tidal phases represented via oscillating force f_2 in Eqn. 7.2 in LES of full-depth LC with crosswind tidal forcing.

7.3 Results

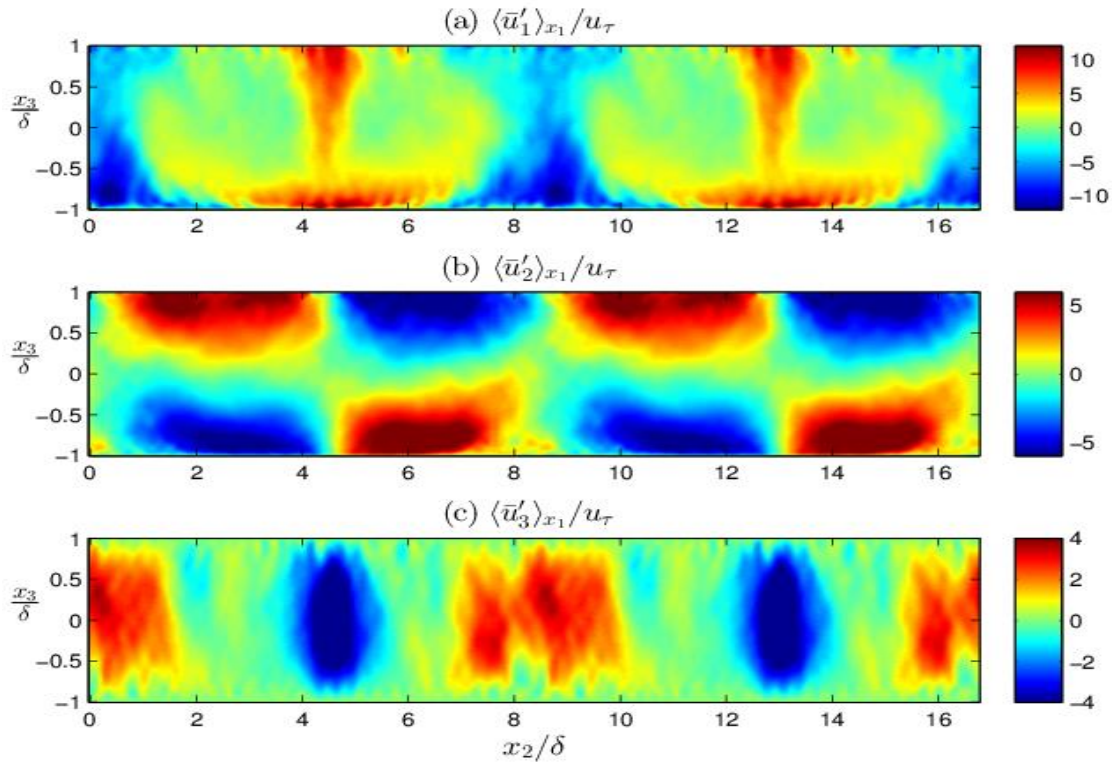


Figure 7.5 Initial instantaneous velocity fluctuations averaged over the downwind (x_1) direction in flow with LC with $La_t = 0.7$ and $\lambda = 6H$

Snapshots of crosswind-vertical variation of downwind-averaged velocity fluctuations are shown in Figures 7.6 through 7.9. These snapshots of the LC structure were taken during the various tidal phases after the simulation had run for more than 3 tidal cycles. Figure 7.6 corresponds to phase 1 (or peak tide) and Figure 7.7 corresponds to phase 2, the part of the cycle between peak and low tides. During peak tide, the LC structure resembles that of the simulation without tides (Figure 7.5). However, by phase 2, the effect of the tidal forcing and associated crosswind shear is clearly evident in terms of the vertical velocity fluctuations (or upwells and downwells) as the cells have broken up into less coherent full-depth cells characterized by smaller crosswind width. Furthermore, downwind velocity fluctuations are no longer intensified

near the bottom of the water column, the latter being one of the key features associated with coherent full-depth cells seen in Figure 7.5 and earlier in Chapter 4. Note that there is a time lag between the crosswind tidal force and its impact on LC structure. The full effect of peak tide (phase 1) causing the full-depth LC to break up into smaller scales is not observed at the time of phase 1, but rather at a later time closer to phase 2 (see Figure 7.4). The weakening of the body force as the tide transitions from peak tide to low tide (phase 2) leads to the re-emergence of the full-depth LC structure as seen in the cases without tidal forcing. However, because of the time lag between the crosswind tidal force and its impact on LC structure, this re-emergence is seen during phase 3 of the body force. The previously described pattern is repeated during phases 4 and 5 shown in Figures 7.9 and 7.10.

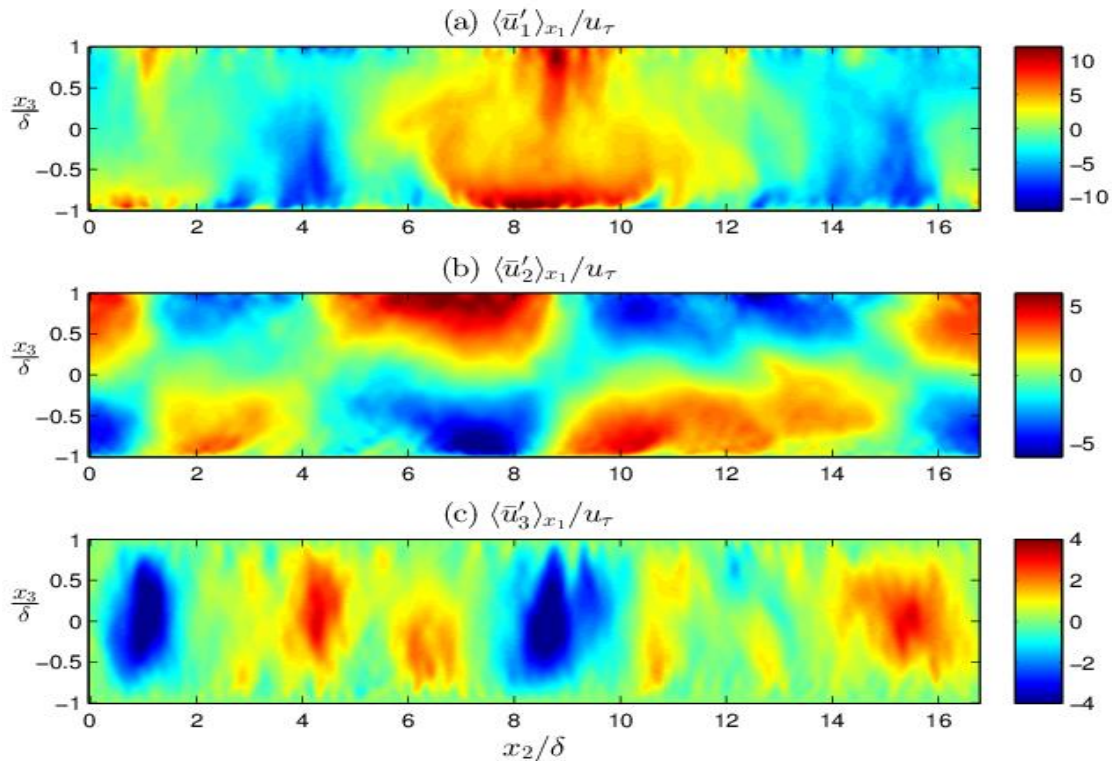


Figure 7.6 Phase 1 instantaneous velocity fluctuations averaged over the downwind (x_1) direction in flow with LC with $La_t = 0.7$ and $\lambda = 6H$.

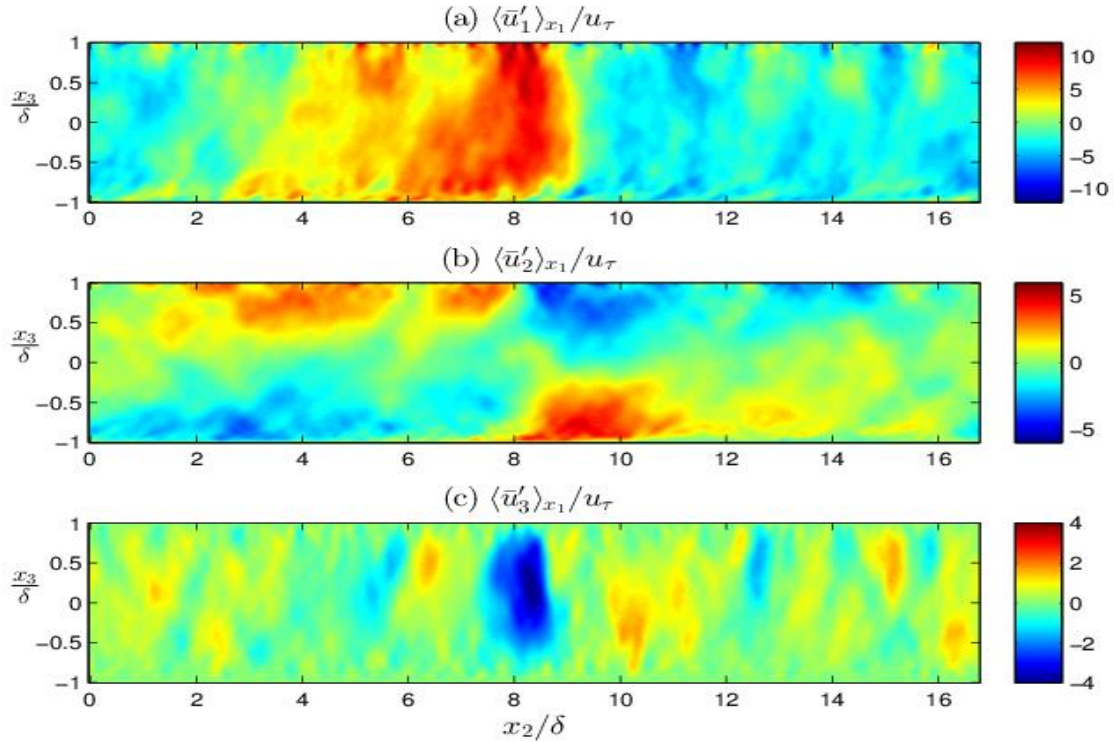


Figure 7.7 Phase 2 instantaneous velocity fluctuations averaged over the downwind (x_1) direction in flow with LC with $La_t = 0.7$ and $\lambda = 6H$.

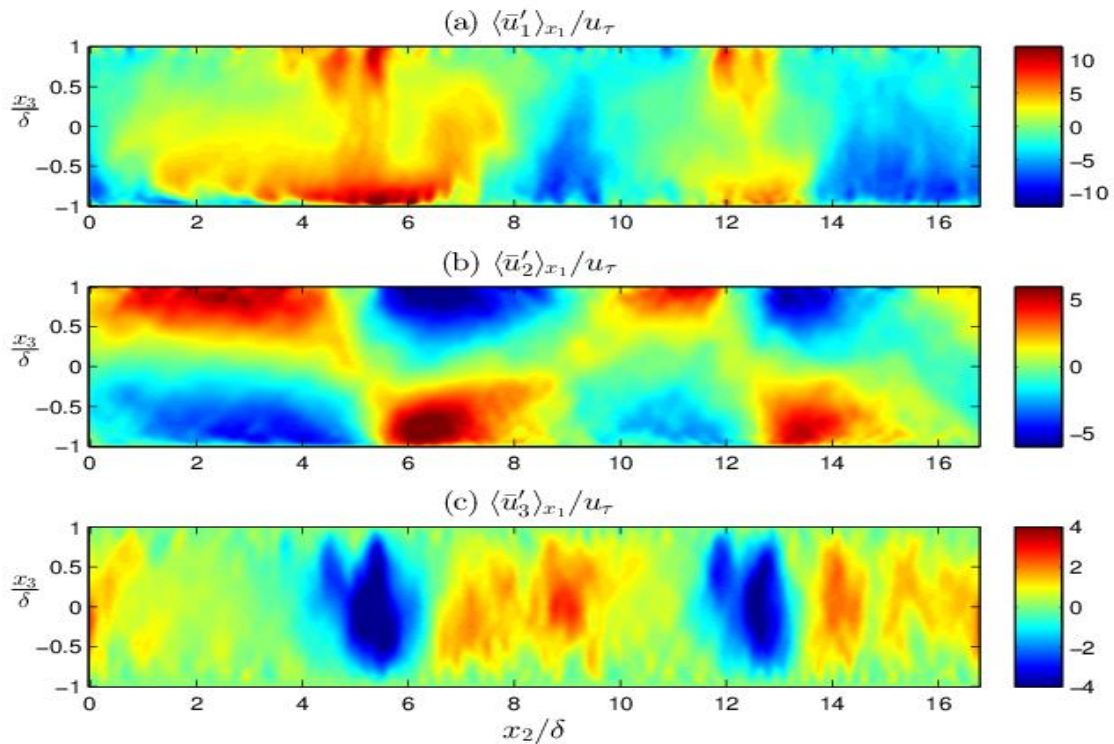


Figure 7.8 Phase 3 instantaneous velocity fluctuations averaged over the downwind (x_1) direction in flow with LC with $La_t = 0.7$ and $\lambda = 6H$.

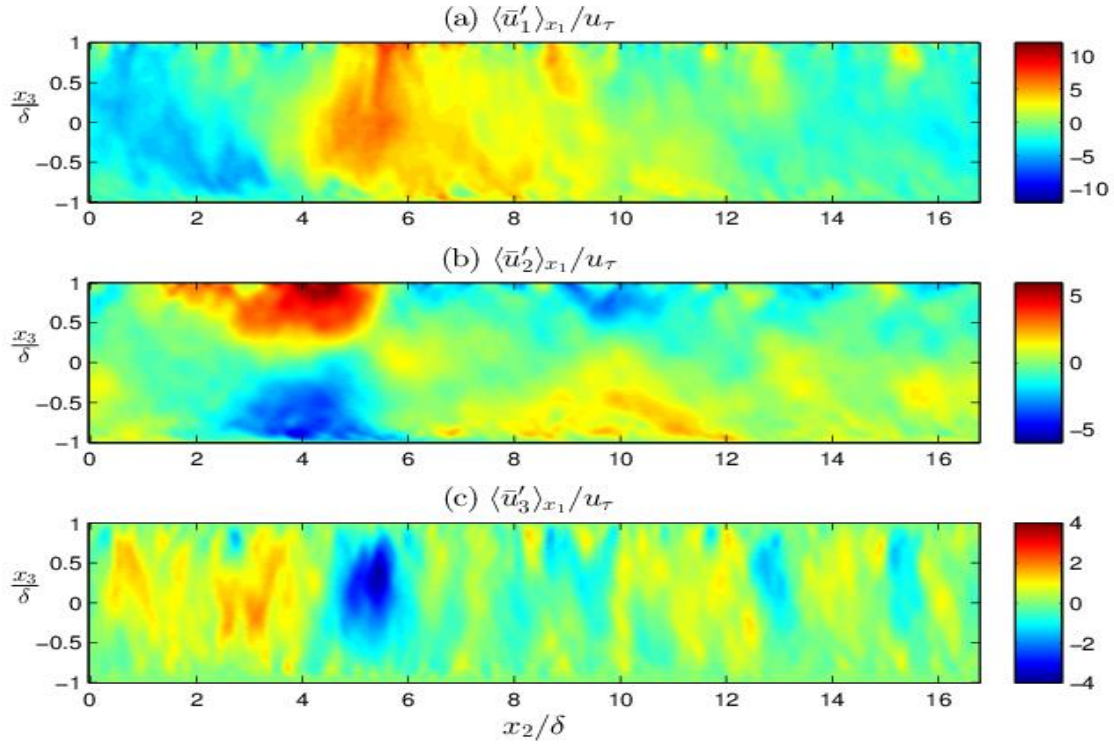


Figure 7.9 Phase 4 instantaneous velocity fluctuations averaged over the downwind (x_1) direction in flow with LC with $La_t = 0.7$ and $\lambda = 6H$.

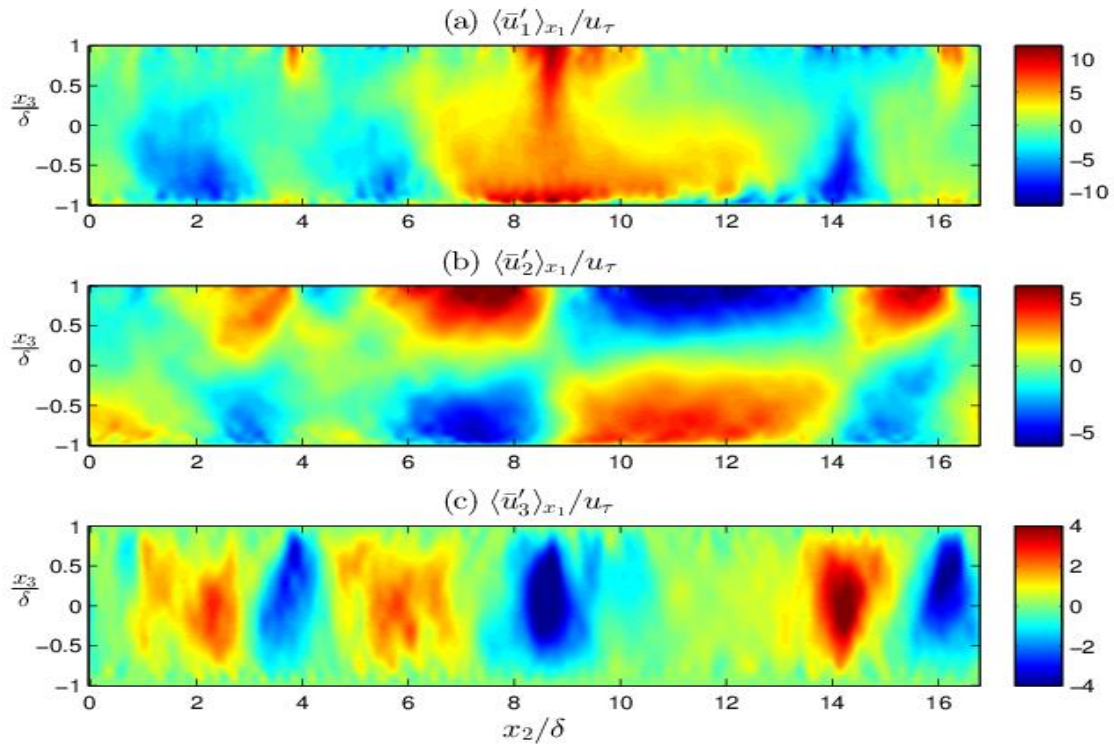


Figure 7.10 Phase 5 instantaneous velocity fluctuations averaged over the downwind (x_1) direction in flow with LC with $La_t = 0.7$ and $\lambda = 6H$.

The structure of Langmuir turbulence in terms of root mean square (rms) of velocity is modulated by the crosswind tidal activity, as seen in Figure 7.11. For example, during phases 1, 3 and 5 during the presence of relatively coherent full-depth cells, vertical velocity rms becomes larger than crosswind velocity rms in the middle of the water column. In the upper part of the

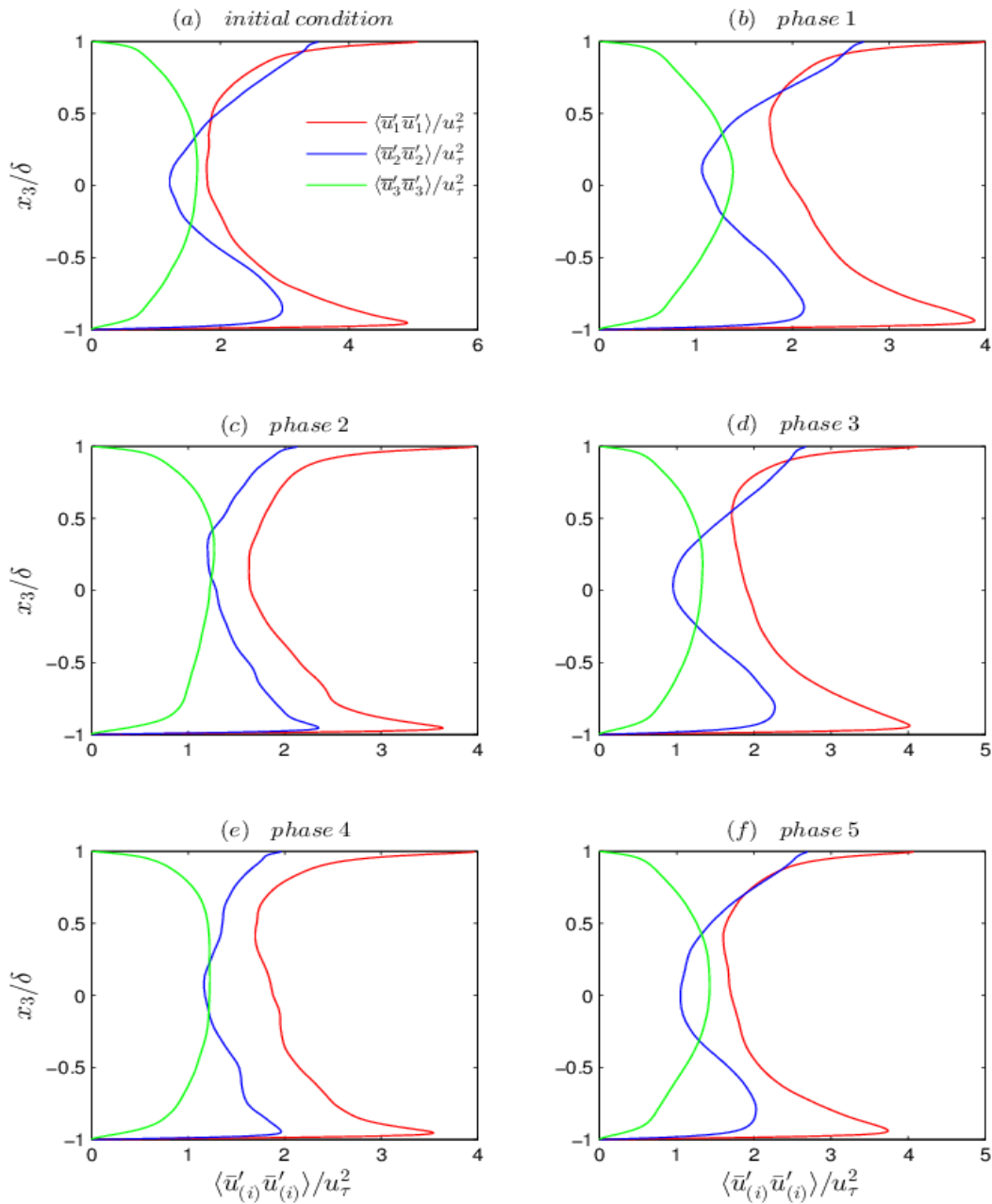


Figure 7.11 Root mean square (rms) of resolved velocity throughout the tidal cycle.

water column, the crosswind velocity rms reaches values greater than downwind rms. This behavior is similar to the velocity rms behavior in the flow with full-depth LC without tides (Figure 7.11a). During phases 2 and 4 when the full-depth cells are less coherent and have smaller crosswind size, the vertical rms becomes comparable to crosswind rms in the middle of the water column, but does not become noticeably greater as it does in phases 1, 3 and 5. Furthermore, crosswind rms does not surpass downwind rms in the upper portion of the water column. In these instances (during phase 2 and phase 4), the turbulence structure is a hybrid between Langmuir-dominated turbulence (Figure 7.11a) and shear-dominated turbulence. In the latter case the streamwise velocity rms is dominant over crosswind and vertical rms throughout the entire water column (as was shown for the flow without full-depth LC nor tides in Fig. 4.7a in Chapter 4).

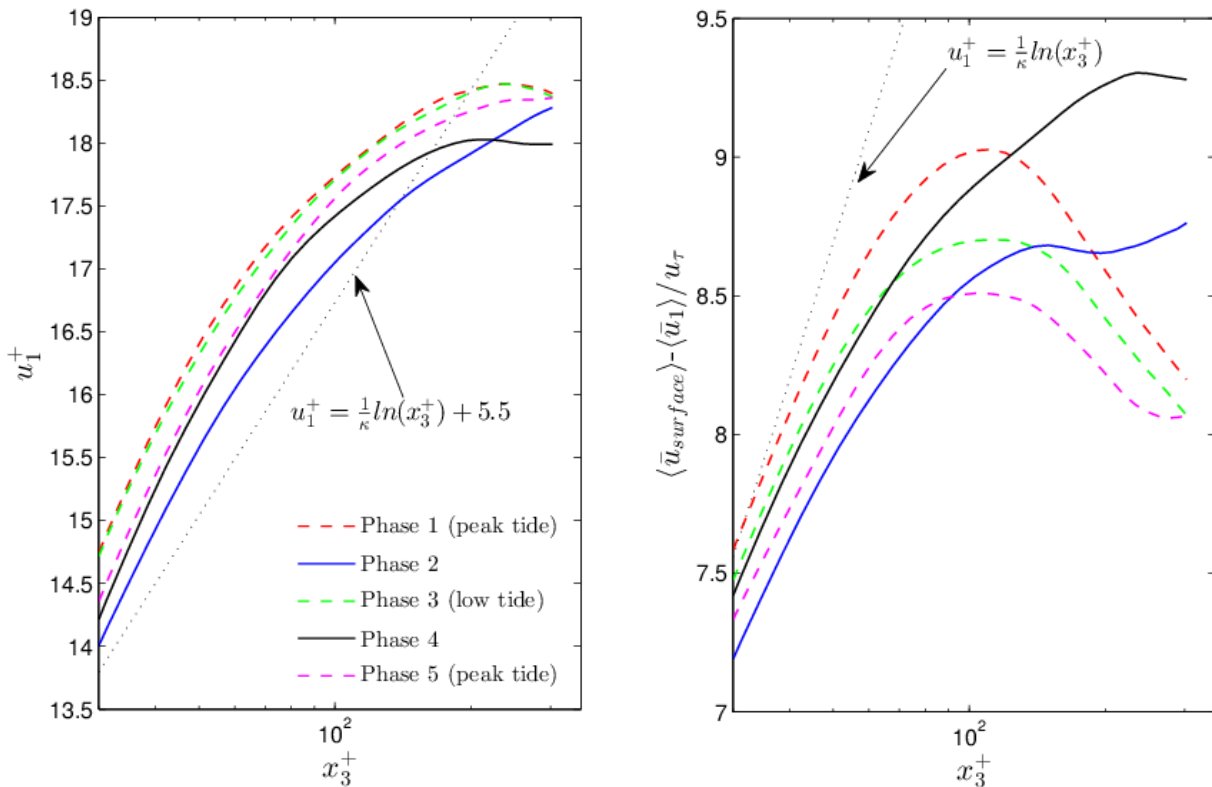


Figure 7.12 Mean downwind velocity near bottom and near surface throughout the tidal cycle.

Finally, Figure 7.12 shows surface and bottom log-layer disruption in terms of mean downwind velocity caused by Langmuir turbulence throughout the tidal cycle. Although surface log-layer disruption occurs at all times, it is weakest during phases 2 and 4 corresponding to times when the full-depth cells have broken up into smaller scale cells due to the crosswind shear induced by the tidal forcing

7.4 Conclusion

In this chapter, results were presented from LES of full-depth LC under the action of an oscillating crosswind tidal force generating a crosswind tidal current. The crosswind tidal current and associated shear serves to sweep the full-depth Langmuir cells in the crosswind direction causing the cells to break up into less coherent, full-depth cells of smaller crosswind width. LES results obtained with the oscillating current were consistent with field measurements of full-depth cells during the occurrence of relatively strong tidal velocities. In these cases, full-depth cells were no longer characterized by near-bottom intensification of downwind velocity fluctuation as is the case when tidal velocities are weaker. As the tidal force weakens in going from peak to low tide, the cells gain coherency, become larger in crosswind size, and near-bottom downwind velocity fluctuations regain strength. Overall, the cells return to similar structure to the full-depth cells when no tides are present. Analysis of rms of velocity obtained in the LES indicated that the crosswind tidal current leads to a hybrid or intermediate turbulent structure in between shear-dominated turbulence (characteristic of wind-driven flows without the action of tides) and Langmuir-dominated turbulence (characteristic of wind-driven flows with full-depth LC without tides). As the tide weakens, the structure reverts back to Langmuir-dominated turbulence. Although tidal forcing was seen to dampen Langmuir turbulence (LT) and

its effects (for example in terms of disruption of classical surface and bottom log-layers) the tidal forcing is not able to extinguish LT and its effects. As the tidal force weakens in going from peak to low tide, Langmuir turbulence re-organizes once again causing disruption of the surface and bottom log-layers.

8 Summary and Conclusions

Langmuir turbulence results from wind-current interaction in the upper ocean, specifically the interaction between the Stokes drift induced by surface gravity waves with the wind-driven shear current. The largest scales of the turbulence are characterized by Langmuir circulation or counter-rotating vortices engulfing the depth of the surface mixed layer in the upper ocean or the full depth of the water column in homogenous (fully mixed) shallow coastal shelf regions. Langmuir circulation manifests itself as windrows on the surface of the ocean coinciding with the surface convergence zone of the Langmuir cells. Windrows can extend for distances on the order of $O(1 \text{ km})$ in the downwind direction and typical distances separating the windrows range between $O(10)$ to $O(100)$ meters.

In the upper ocean, turbulence is generated via a number of mechanisms such as surface-wave breaking, wave-current interaction (giving rise to Langmuir-dominated turbulence), wind shear (giving rise to shear-dominated turbulence) and destabilizing surface heat fluxes (giving rise to convective turbulence). A recent study by Belcher et al. (2012) found that wind and wave forcing conditions in the Southern Ocean are favorable to Langmuir-dominated turbulence over 80% of the time throughout the year. Meanwhile in the North Atlantic, during winter, conditions are favorable to Langmuir-dominated turbulence for about 70% of the time. Overall their conclusion was that Langmuir turbulence is important everywhere in the world's ocean and thus must be parameterized in climate models.

This dissertation focused on understanding the impact of Langmuir turbulence in homogenous shallow water and associated full-depth Langmuir circulation on bottom and surface boundary layers in coastal shelf regions. This understanding formed the basis for the derivation and testing of a shallow water Langmuir turbulence parameterization suitable for coastal ocean circulation models.

The effect of Langmuir turbulence with full-depth LC was explored in terms of wind and wave forcing parameters such as surface gravity wave wavelength, surface gravity wave amplitude and wind stress. Specifically, the parameters were surface wavelength, λ , and turbulent Langmuir number, La_t , the latter inversely proportional to wave forcing relative wind forcing.

Langmuir turbulence led to the disruption of surface log-layer dynamics in terms of the mean downwind velocity and the production and dissipation rates of TKE. This disruption included deviations from (i) the classical log-law velocity profile and (ii) the classical balance between production and dissipation rates of TKE, both exhibited by wind-driven flows without LC in the near-surface region of the water column. The primary factor controlling surface log-layer dynamics was seen to be Stokes drift vertical shear which serves to enhance near-surface small scale vortices and associated vertical mixing. Recall that Stokes drift velocity interacts with the wind-driven current to generate Langmuir turbulence. Furthermore, Stokes drift decays with depth with decay rate inversely proportional to the dominant wavelength, λ , of surface gravity waves. Thus, for deep water waves characterized by relatively shorter wavelengths (short waves), Stokes drift decays rapidly with depth inducing high Stokes drift shear near the surface and reduced (near zero) shear at depths below. The higher Stokes drift shear near the surface leads to intense small scale eddies near the surface and thus stronger surface log-layer disruption

despite the weaker full-depth Langmuir cells generated due to the reduced Stokes drift vertical shear throughout the bulk of the water column.

Full-depth LC was also seen to cause negative mean velocity shear throughout the bulk region of the flow. Such behavior is important for Reynolds shear stress parameterization, as parameterizations purely based on local mean velocity shear are not able to represent the negative mean shear of the velocity.

It was found that for sufficiently long waves, full-depth LC disrupts classical bottom boundary layer dynamics. For example, full-depth LC can disrupt the bottom log-law, inducing a “law of the wake-like” behavior. The disruption is primarily caused by the downwelling limb of LC which brings high speed fluid down to the log-layer region. The extent of this disruption depends on the strength of LC in the bottom half of the water column as determined through the wavelength (λ) of the surface waves generating the LC. Smaller λ generate weaker, less disruptive LC. For sufficiently long wavelengths, the extent of the disruption also depends on the structure of LC as determined through the turbulent Langmuir number, La_t . For example lowering La_t can lead to strengthening of the upwelling limb of the cell. A stronger upwelling limb is characterized by an increase in the rate at which it brings slower moving fluid up to the log-layer, thereby diminishing the log-layer disrupting effect of the downwelling limb.

A K-profile parameterization (KPP) of Langmuir turbulence in shallow water comprised of local and nonlocal components was introduced capturing the basic mechanisms by which Langmuir turbulence and associated full-depth LC impact the mean flow. Single water column RANS simulations (based on the Reynolds-averaged Navier-Stokes equations) with the new parameterization were presented showing good agreement with LES in terms of mean velocity

profiles. The new KPP was shown to lead to much better representation of the mean velocity profile during the occurrence of Langmuir turbulence than the standard (traditional) KPP (Large, 1994) and the well-known $k-\epsilon$ model. The KPP introduced is characterized by two coefficients dependent on the strength of the full-depth LC. It was shown that both of these coefficients may be calibrated via LES. Future research should focus on parameterizing these coefficients as functions of wind and wave forcing parameters λ and La_t by performing LES simulations covering a range of likely values of λ and La_t .

In Chapter 7 results were presented from LES of Langmuir turbulence in shallow water under the action of an oscillating crosswind tidal force generating a crosswind tidal current. These simulations were motivated by two separate field measurements of Langmuir turbulence, one under relatively weak tidal velocities (Gargett and Wells, 2007) and another under stronger tidal velocities (Gargett and Savidge, 2008). The LES revealed that the crosswind tidal current and associated shear serves to sweep full-depth Langmuir cells in the crosswind direction causing the cells to break up into less coherent, full-depth cells of smaller crosswind width. LES results obtained with the oscillating current were consistent with field measurements of full-depth cells during the occurrence of relatively strong tidal velocities. In these cases full-depth cells were no longer characterized by near-bottom intensification of downwind velocity fluctuation as is the case when tidal velocities are weaker. As the tidal force weakens in going from peak to low tide, the cells regain coherency, become larger in crosswind size, and near-bottom downwind velocity fluctuations regain strength. This was consistent with the field measurements.

Overall, tidal forcing was seen to dampen Langmuir turbulence and its effects (for example in terms of disruption of classical surface and bottom log-layers) leading to a hybrid regime of turbulence between Langmuir-dominated and shear-dominated turbulence. However, as the tidal

force weakens in going from peak to low tide, Langmuir turbulence re-organizes proceeding to intensify its disruption of the surface and bottom log-layers.

The previously described understanding of Langmuir turbulence in shallow water and parameterization can serve as basis for further research:

- i. The modified KPP model accounting for shallow water Langmuir turbulence derived and tested in Chapter 6 may be readily implemented in a general coastal ocean circulation model (GCOCM). The coastal upwelling scenario described in Chapter 2 would be an excellent test-case for the new KPP and its behavior relative to traditional parameterizations that do not take into account the effect of Langmuir turbulence. In this scenario, strong mixing of the water column in regions closest to the coast may limit the cross-shore extent of upwelling currents, forcing these currents to terminate off-shore (i.e. at distances farther away from the coast). This results in a shut-down of near-coast, cross-shelf transport of nutrients, as well-mixed water becomes trapped at the coast. It is hypothesized that the shut-down mechanism may be enhanced by the intense vertical mixing caused by the action of full-depth Langmuir cells within the trapped water close to the coast. This behavior would be possible to represent via the newly developed KPP.
- ii. The newly derived KPP possess two coefficients dependent on the strength of the full-depth Langmuir cells in the upper- and lower-half of the water column. In Chapter 6, it was shown that both of these coefficients may be calibrated via LES. Future research should focus on parameterizing these coefficients as functions of

wind and wave forcing parameters λ and La_t by performing a suite of LES over a range of typical values for these parameters.

- iii. The analysis of LES results in Chapters 4 and 5 used to develop the newly proposed KPP in Chapter 6 may be also put to use for enabling other RANS parameterizations such as the k- ϵ and Mellor-Yamada models to be able to account for Langmuir turbulence.
- iv. The LES of full-depth LC in Chapter 6 was performed with a crosswind oscillating tidal current. In the future, tests should be done with an oscillating tidal current in the downwind direction as well. In principle, the tidal forcing should be extended to general directions following, for example, the work of Sakamoto and Akitomo (2008) who included the effect of tides via a tidal velocity advection term in the Navier-Stokes equations. Note that the work of Sakamoto and Akitomo (2008) has been done without a wind stress (i.e. with zero surface shear stress). The turbulence structure of a tidal current together with a surface stress over a no-slip bottom has gone largely uninvestigated, and thus this should be done first prior to the addition of Craik-Leibovich forcing generating Langmuir turbulence. The only research on the effect of a tidal current together with surface stress (without Craik-Leibovich (Langmuir) forcing) with a no-slip bottom has been explored by Kramer (2010); however, in their case the tidal current and the wind stress were aligned. Analysis of surface and bottom log-layer dynamics in flows with a surface wind stress and general tidal current should consider the net current (between downwind and crosswind components), and not only the downwind current which was the case in Chapter 7, Figure 7.12. For example, the

net current is expected to also be characterized by a bottom log law and its behavior under the influence of the varying phases of full-depth LC due to an oscillating crosswind current should be investigated.

References

- Akan, C., Tejada-Martínez, A.E., Grosch, C.E., Martinat, G., 2013. Scalar transport in large-eddy simulation of Langmuir turbulence in shallowwater. *Cont. Shelf Res.* 55, 1–16.
- Austin, J.A., Lentz, S.J., 2002. The Inner Shelf Response to Wind-Driven Upwelling and Downwelling *. *J. Phys. Oceanogr.* 32, 2171–2193.
- Barstow, S., 1983. The ecology of Langmuir circulation: a review. *Mar. Environ. Res.* 9, 211–236.
- Belcher, S.E., Grant, A.L.M., Hanley, K.E., Fox-Kemper, B., Van Roekel, L., Sullivan, P.P., Large, W.G., Brown, A., Hines, A., Calvert, D., Rutgersson, A., Pettersson, H., Bidlot, J.-R., Janssen, P. a. E.M., Polton, J. a., 2012. A global perspective on Langmuir turbulence in the ocean surface boundary layer. *Geophys. Res. Lett.* 39, L18605.
- Burchard, H., Petersen, O., Rippeth, T.P., 1998. Comparing the performance of the Mellor-Yamada the two-equation turbulence models and the Kolmogorov. *J. Geophys. Res.* 103, 10543–10554.
- Coles, D., 1956. The law of the wake in the turbulent boundary layer. *J. Fluid Mech.* 1, 191.
- Craik, A.D.D., Leibovich, S., 1976. A rational model for Langmuir circulations. *J. Fluid Mech.* 73, 401–426.
- Davidson, P.A., 2004. *Turbulence: An Introduction for Scientists and Engineers*. Oxford University Press.
- Donelan, M.A., 1998. Physical Processes in Lakes and Oceans, in: Imberger, J. (Ed.), *Coastal and Estuarine Studies*. American Geophysical Union, Washington, D. C., pp. 1–668.
- Durski, S.M., 2004. Vertical mixing schemes in the coastal ocean: Comparison of the level 2.5 Mellor-Yamada scheme with an enhanced version of the K profile parameterization. *J. Geophys. Res.* 109, C01015.
- Frech, M., Mahrt, L., 1995. A two-scale mixing formulation for the atmospheric boundary layer. *Boundary-Layer Meteorol.* 73, 91–104.
- Gargett, A., Wells, J., Tejada-Martínez, A.E., Grosch, C.E., 2004. Langmuir supercells: a mechanism for sediment resuspension and transport in shallow seas. *Science* 306, 1925–8.

- Gargett, A.E., Savidge, D. k., 2008. The role of Langmuir supercells in seasonally tuned cross-shelf transport of bioactive material. Abstr. AGU Ocean Sci. Meet. Orlando, FL.
- Gargett, A.E., Wells, J.R., 2007. Langmuir turbulence in shallow water. Part 1. Observations. *J. Fluid Mech.* 576, 27.
- Grant, A.L.M., Belcher, S.E., 2009. Characteristics of Langmuir Turbulence in the Ocean Mixed Layer. *J. Phys. Oceanogr.* 39, 1871.
- Harcourt, R.R., D'Asaro, E. a., 2008. Large-Eddy Simulation of Langmuir Turbulence in Pure Wind Seas. *J. Phys. Oceanogr.* 38, 1542.
- Holm, D., 1996. The ideal Craik-Leibovich equations. *Phys. D Nonlinear Phenom.* 98, 415–441.
- Kawamura, T., 2000. Numerical investigation of turbulence near a sheared air–water interface. Part 2: Interaction of turbulent shear flow with surface waves. *J. Mar. Sci. Technol.* 5, 161–175.
- Kukulka, T., Plueddemann, a. J., Trowbridge, J.H., Sullivan, P.P., 2011. The influence of crosswind tidal currents on Langmuir circulation in a shallow ocean. *J. Geophys. Res.* 116, 1–15.
- Langmuir, I., 1938. Surface Motion of Water Induced by Wind. *Adv. Sci.* 87, 119–123.
- Large, W.G., McWilliams, J.C., Doney, S.C., 1994. Oceanic vertical mixing: A review and a model with a nonlocal boundary layer parameterization. *Rev. Geophys.* 32, 363.
- Li, M., Radhakrishnan, S., Piomelli, U., Rockwell Geyer, W., 2010. Large-eddy simulation of the tidal-cycle variations of an estuarine boundary layer. *J. Geophys. Res.* 115, 1–18.
- Lilly, D.K., 1992. A proposed modification of the Germano subgrid-scale closure method. *Phys. Fluids A Fluid Dyn.* 4, 633.
- Martinat, G., Xu, Y., Grosch, C.E., Tejada-Martínez, A.E., 2011. LES of turbulent surface shear stress and pressure-gradient-driven flow on shallow continental shelves. *Ocean Dyn.* 61, 1369–1390.
- McWilliams, J.C., Huckle, E., Liang, J.-H., Sullivan, P.P., 2012. The Wavy Ekman Layer: Langmuir Circulations, Breaking Waves, and Reynolds Stress. *J. Phys. Oceanogr.* 42, 1793–1816.
- McWilliams, J.C., Sullivan, P.P., Moeng, C.-H., 1997. Langmuir turbulence in the ocean. *J. Fluid Mech.* 334, 1–30.
- Mellor, G.L., Yamada, T., 1982. Development of a turbulence closure model for geophysical fluid problems. *Rev. Geophys.* 20, 851.

- Papavassiliou, D.V.D.V., Hanratty, T.J.T.J., 1997. Transport of a passive scalar in a turbulent channel flow. *Int. J. Heat Mass Transf.* 40, 1303–1311.
- Phillips O.M., 1967. *The Dynamics of the Upper Ocean*. Cambridge at the university press.
- Piomelli, U., Balaras, E., 2002. Wall-layer models for large-eddy simulations. *Annu. Rev. Fluid Mech.*
- Pope, S.B., 2000. *Turbulent Flows*. Cambridge University Press.
- Robinson, S., 1991. Coherent Motions In The Turbulent Boundary Layer. *Annu. Rev. Fluid Mech.* 23, 601–639.
- Savidge, W., Gargett, A., Jahnke, R., Nelson, J., Savidge, D., Short, R., Voulgaris, G., 2008. Forcing and Dynamics of Seafloor-Water Column Exchange on a Broad Continental Shelf, *Oceanography*.
- Schlichting, H., 1960. *Boundary layer theory*, McGraw-Hill. McGraw-Hill.
- Skyllingstad, E.D., Samelson, R.M., 2012. Baroclinic Frontal Instabilities and Turbulent Mixing in the Surface Boundary Layer. Part I: Unforced Simulations. *J. Phys. Oceanogr.* 42, 1701–1716.
- Smyth, W.D., Skyllingstad, E.D., Crawford, G.B., Wijesekera, H., 2002. Nonlocal fluxes and Stokes drift effects in the K-profile parameterization. *Ocean Dyn.* 52, 104–115.
- Teixeira, M. a. C., 2012. The influence of Langmuir turbulence on the scaling for the dissipation rate in the oceanic boundary layer. *J. Geophys. Res.* 117, 1–15.
- Tejada-Martínez, A.E., Akan, C., Sinha, N., Grosch, C.E., Martinat, G., 2013. Surface dynamics in LES of full-depth Langmuir circulation in shallow water. *Phys. Scr.* T155, 014008.
- Tejada-martínez, A.E., Grosch, C.E., Sinha, N., Akan, C., Martinat, G., 2012. Disruption of bottom log-layer in LES of full-depth Langmuir circulation. *J. Fluid Mech.* 699, 79–93.
- Tejada-Martínez, A.E., 2002. *Dynamic Subgrid-Scale Modeling for Large-Eddy Simulation of Turbulent Flows with a Stabilized Finite Element Method*. Rensselaer Polytechnic Institute.
- Tejada-Martínez, A.E., Grosch, C.E., 2007. Langmuir turbulence in shallow water. Part 2. Large-eddy simulation. *J. Fluid Mech.* 576, 63.
- Thorpe, S. a., 2004. Langmuir Circulation. *Annu. Rev. Fluid Mech.* 36, 55–79.
- Umlauf, L., Burchard, H., Hutter, K., 2003. Extending the $k-\omega$ turbulence model towards oceanic applications. *Ocean Model.* 5, 195–218.

Veron, F., Melville, W.K., 2001. Experiments on the stability and transition of wind-driven water surfaces. *J. Fluid Mech.* 446, 25–65.

Appendices

Appendix A : Rights and Permissions

A.1 Permission to Use Figure 1.2



Nityanand Sinha <nsinha@mail.usf.edu>

Permission to use figure

Andreas Thurnherr <ant@ldeo.columbia.edu>
To: Nityanand Sinha <nsinha@mail.usf.edu>

Fri, Nov 15, 2013 at 10:06 AM

Dear Nityanand Sinha,

This is so funny: I took that image on a really cheap digital camera in 640x480 resolution and it has already appeared in two glossy oceanography books. There *must* be a better image around, somewhere. But, yes, by all means, you have my permission to use the figure in your thesis.

Cheers

- Andreas

On Nov 14, 2013, at 7:53 PM, Nityanand Sinha wrote:

Dear Dr. Thurnherr

I am currently a PhD candidate at university of South Florida working,towards to obtain my degree by December, 2013. I respectfully ask to use the figure

(http://www.ldeo.columbia.edu/~ant/Langmuir_1.jpg) on your website in my dissertation

titled "Towards RANS Parameterization of Vertical Mixing by Langmuir Turbulence in

Shallow Coastal Shelves".

I will be really glad if you could let me know as early as possible, and i will appreciate your help.

Kind Regards

--

Nityanand Sinha

A.2 Permission to Use Figure 1.5



Nityanand Sinha <nsinha@mail.usf.edu>

Reprint permission

Tejada-Martinez, Andres etejada@usf.edu
To: "Sinha, Nityanand" <nsinha@mail.usf.edu>

Tue, Nov 19, 2013 at 10:58 PM

Nitya,

Yes, you may use these figures.

Andres

From: Nityanand Sinha [<mailto:nsinha@mail.usf.edu>]
Sent: Thursday, November 14, 2013 7:25 PM
To: Tejada-Martinez, Andres
Subject: Reprint permission

i need to obtain reprint permission for every previously published figure/table that i used in my dissertation. Thus, I respectfully ask to use the figure 1.2 on page 11 of your PhD dissertation title "Dynamic Subgrid-scale Modeling for Large-Eddy Simulation of Turbulent Flows with a stabilized Finite Element Method" in my dissertation titled "Towards RANS Parameterization of Vertical Mixing by Langmuir Turbulence in Shallow Coastal Shelves".

Please do let me know, and i will appreciate your help.

--

Nityanand Sinha

A.3 Permission to Use Figure 7.1

CAMBRIDGE UNIVERSITY PRESS LICENSE TERMS AND CONDITIONS

Nov 18, 2013

This is a License Agreement between Nityanand Sinha ("You") and Cambridge University Press ("Cambridge University Press") provided by Copyright Clearance Center ("CCC"). The license consists of your order details, the terms and conditions provided by Cambridge University Press, and the payment terms and conditions.

All payments must be made in full to CCC. For payment instructions, please see information listed at the bottom of this form.

License Number	3272090396205
License date	Nov 18, 2013
Licensed content publisher	Cambridge University Press
Licensed content publication	The Journal of Fluid Mechanics
Licensed content title	Langmuir turbulence in shallow water. Part 1. Observations
Licensed content author	ANN E. GARGETT and JUDITH R. WELLS
Licensed content date	Apr 10, 2007
Volume number	576
Issue number	-1
Start page	27
End page	61
Type of Use	Dissertation/Thesis
Requestor type	Author
Portion	Full article
Author of this Cambridge University Press article	No
Author / editor of the new work	Yes
Order reference number	
Territory for reuse	North America Only

Title of your thesis / dissertation	Towards RANS Parameterization of Vertical Mixing by Langmuir Turbulence in Shallow Coastal Shelves
Expected completion date	Dec 2013
Estimated size(pages)	140
Billing Type	Invoice
TAX (0.00%)	0.00 USD
Total	0.00 USD
Terms and Conditions	

TERMS & CONDITIONS

Cambridge University Press grants the Licensee permission on a non-exclusive nontransferable basis to reproduce, make available or otherwise use the Licensed content 'Content' in the named territory 'Territory' for the purpose listed 'the Use' on Page 1 of this Agreement subject to the following terms and conditions.

1. The permission granted is not valid until the Licensee has paid in full.
2. The License is limited to the permission granted and the Content detailed herein and does not extend to any other permission or content.
3. Cambridge gives no warranty or indemnity in respect of any third-party copyright material included in the Content, for which the Licensee should seek separate permission clearance.
4. The integrity of the Content must be ensured.
5. The License does extend to any edition published specifically for the use of handicapped or reading-impaired individuals.
6. The Licensee shall provide a prominent acknowledgement in the following format:
author/s, title of article, name of journal, volume number, issue number, page references, , reproduced with permission.

If author's own material and free of charge then condition 1 to be removed. Other terms and conditions: None v1.0

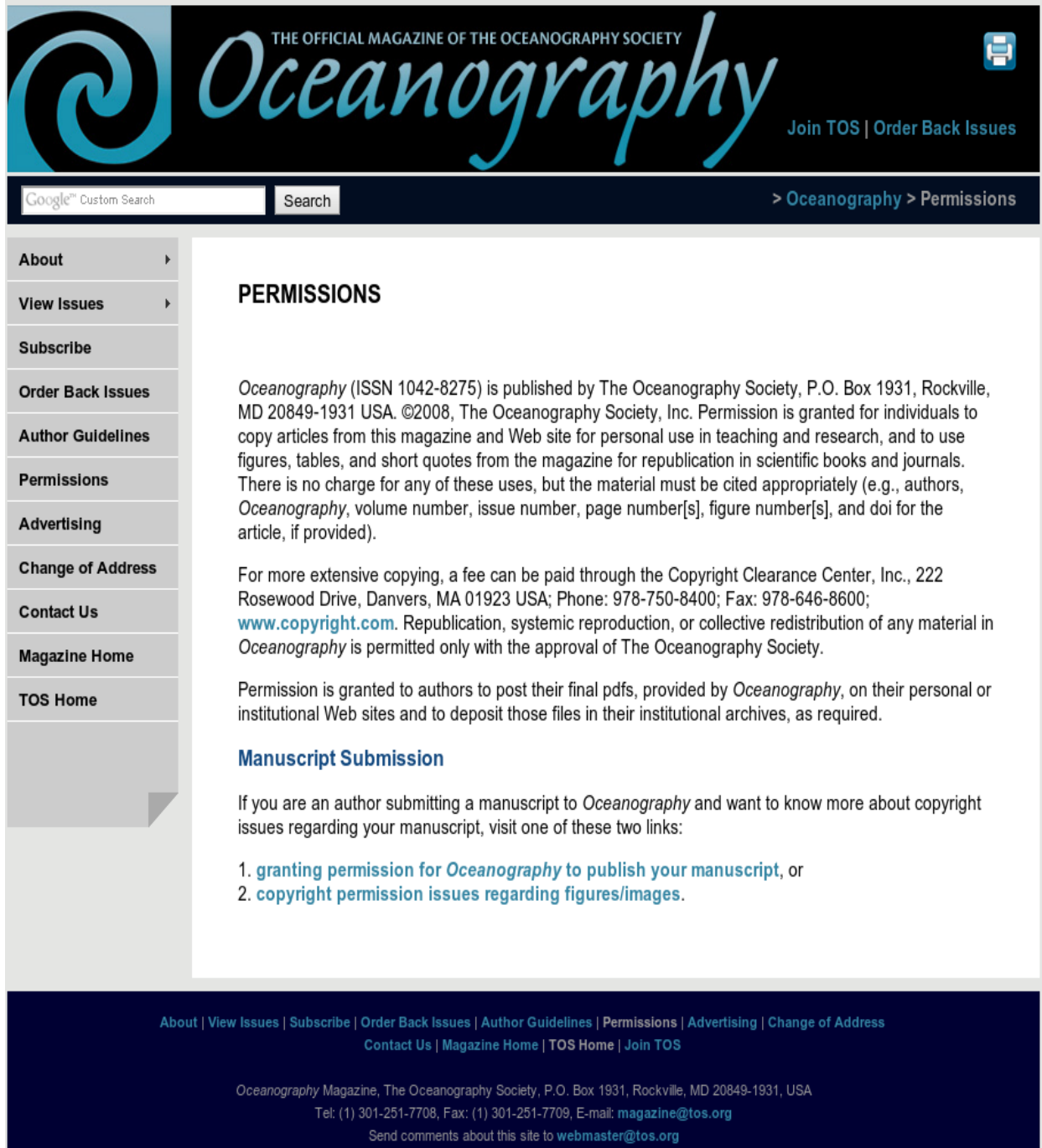
If you would like to pay for this license now, please remit this license along with your payment made payable to "COPYRIGHT CLEARANCE CENTER" otherwise you will be invoiced within 48 hours of the license date. Payment should be in the form of a check or money order referencing your account number and this invoice number RLNK501162025. Once you receive your invoice for this order, you may pay your invoice by credit card. Please follow instructions provided at that time.

**Make Payment To:
Copyright Clearance Center
Dept 001
P.O. Box 843006
Boston, MA 02284-3006**

For suggestions or comments regarding this order, contact RightsLink Customer Support: customercare@copyright.com or +1-877-622-5543 (toll free in the US) or +1978-646-2777.

Gratis licenses (referencing \$0 in the Total field) are free. Please retain this printable license for your reference. No payment is required.

A.4 Permission to Use Figure 2.2 and 7.2



The screenshot shows the website for Oceanography Magazine, the official magazine of the Oceanography Society. The header features the magazine's logo, the title "Oceanography", and the text "THE OFFICIAL MAGAZINE OF THE OCEANOGRAPHY SOCIETY". There are links for "Join TOS" and "Order Back Issues". Below the header is a search bar with "Google Custom Search" and a "Search" button. A navigation menu on the left includes links for "About", "View Issues", "Subscribe", "Order Back Issues", "Author Guidelines", "Permissions", "Advertising", "Change of Address", "Contact Us", "Magazine Home", and "TOS Home". The main content area is titled "PERMISSIONS" and contains the following text:

PERMISSIONS

Oceanography (ISSN 1042-8275) is published by The Oceanography Society, P.O. Box 1931, Rockville, MD 20849-1931 USA. ©2008, The Oceanography Society, Inc. Permission is granted for individuals to copy articles from this magazine and Web site for personal use in teaching and research, and to use figures, tables, and short quotes from the magazine for republication in scientific books and journals. There is no charge for any of these uses, but the material must be cited appropriately (e.g., authors, *Oceanography*, volume number, issue number, page number[s], figure number[s], and doi for the article, if provided).

For more extensive copying, a fee can be paid through the Copyright Clearance Center, Inc., 222 Rosewood Drive, Danvers, MA 01923 USA; Phone: 978-750-8400; Fax: 978-646-8600; www.copyright.com. Republication, systemic reproduction, or collective redistribution of any material in *Oceanography* is permitted only with the approval of The Oceanography Society.

Permission is granted to authors to post their final pdfs, provided by *Oceanography*, on their personal or institutional Web sites and to deposit those files in their institutional archives, as required.

Manuscript Submission

If you are an author submitting a manuscript to *Oceanography* and want to know more about copyright issues regarding your manuscript, visit one of these two links:

1. [granting permission for *Oceanography* to publish your manuscript, or](#)
2. [copyright permission issues regarding figures/images.](#)

The footer contains a navigation bar with links: "About | View Issues | Subscribe | Order Back Issues | Author Guidelines | Permissions | Advertising | Change of Address | Contact Us | Magazine Home | TOS Home | Join TOS". Below this, it provides contact information: "Oceanography Magazine, The Oceanography Society, P.O. Box 1931, Rockville, MD 20849-1931, USA. Tel: (1) 301-251-7708, Fax: (1) 301-251-7709, E-mail: magazine@tos.org. Send comments about this site to webmaster@tos.org".